Proton pencil beam kernels as extracted from Geant4 Monte Carlo simulations

by

Maluba Vernon J. Chisapi

Thesis presented in partial fulfilment of the requirements for the degree of ***Master of Science in the Faculty of Science*** *at Stellenbosch University*

Department of Physics,
Stellenbosch University,
Private Bag X1, Matieland 7602, South Africa.

Supervisors:

Prof. Richard T. Newman
Mr. Evan A. de Kock

December 2016

Declaration

By submitting this thesis electronically, I declare that the entirety of the work contained therein is my own, original work, that I am the sole author thereof (save to the extent explicitly otherwise stated), that reproduction and publication thereof by Stellenbosch University will not infringe any third party rights and that I have not previously in its entirety or in part submitted it for obtaining any qualification.

Date: December 2016 .....

Abstract

Proton pencil beam kernels as extracted from Geant4 Monte Carlo simulations

M. V. J. Chisapi

Department of Physics,
Stellenbosch University,
Private Bag X1, Matieland 7602, South Africa.

Thesis: M.Sc.

December 2016

The contribution of primary protons, secondary protons, heavy recoil ions, and other secondary particles to the total energy deposited in water by a proton pencil beam (in the therapeutic energy regime) has been investigated using the Geant4 Monte Carlo simulation toolkit. Simulation results have been compared with those calculated using dose distribution functions of the analytical beamlet model of Ulmer et al., which is currently used in the commercial proton treatment-planning package Eclipse^{TM}. Optimized settings for a robust, accurate, and computationally inexpensive Geant4 simulations have also been proposed.

Uittreksel

Proton dun-bundel dieptedosis berekeninge deur middel van Geant4 Monte Carlo simulasies

*("**Proton pencil beam kernels as extracted from Geant4 Monte Carlo simulations**")*

M. V. J. Chisapi

Departement Fisika,
Universiteit van Stellenbosch,
Privaatsak X1, Matieland 7602, Suid Afrika.

Tesis: M.Sc.

Desember 2016

Monte Carlo simulasies is gedoen met Geant4 om die primêre protone, sekondêre protone, swaar terugslag-ione en ander sekondêre deeltjies se bydraes te bepaal tot die energie wat deur 'n dun protonbundel in water gedeponeer word. Hierdie ondersoek is uitgevoer vir protone in die terapeutiese energiegebied. Die resultate wat vekrei is van die Monte Carlo simulasies is vergelyk met dosisverspreidings wat breken is venaf die analitiese dun-bundel model van Ulmer et al. Dié model word tans gebruik in die Eclipse^{TM} stelsel, wat 'n kommersiële beplanningsisteem vir protonterapie is. Verstellings word ook verskaf wat verseker dat die Geant4 simulasies geoptimaliseer is in terme van robuustheid, akkuraatheid en berekeningspoed.

Acknowledgements

My sincere gratitude to my supervisors: Prof. Richard T. Newman and Evan A. de Kock for giving me the opportunity to study under their supervision, their enlightening academic support and guidance. Special thanks to Evan de Kock for charting the direction of this work and his most appreciated input throughout the course of the study. I would also like to thank God for good health and sustenance during my studies. I am indebted to my family for their continued support, and all colleagues and friends for discussions and conversations exchanged.
I am particularly grateful to Alexander Howard of CERN and Jeysingam Jeyasugiththan of the Department of Clinical Oncology of Jaffna Teaching Hospital for their assistance on Geant4 related matters.

This thesis would not be possible, had it not been for the financial and academic support of the following institutions: the African Institute of Mathematical Sciences (AIMS), the Faculty of Science and the Department of Physics of Stellenbosch University, the University of Zambia, and the National Research Foundation (NRF) through iThemba LABS.

Dedications

This thesis is thankfully dedicated to my late loving mother Genevieve Esther Chisapi who inspired me and did everything she could to ensure I get an education, I will forever love you.

Contents

List of Figures

List of Tables

Chapter 1

Introduction

Since the first hospital-based proton therapy center was established in the 1990s, proton radiation therapy has continued to gain popularity in cancer treatment. Hundreds of different types of cancers (emanating from different body tissues) are being diagnosed today. Some of them are not only difficult to cure with prevalent methods (e.g., surgery, chemotherapy, x-ray or radiotherapy), but their treatment with methods such as radiotherapy could lead to exposure of surrounding healthy tissue or critical organs to damage by radiation. Conventional photon radiation has been used extensively to treat certain tumours, either alone or in combination with other modalities. Any form of cancer treatment plan involving radiation is adopted based on its ability to deliver sufficiently high dose to the target volume, with the aim of eradicating the cancerous tumour, while limiting dose falling on healthy tissue as much as possible to avoid late effects and toxicity. With the advent of improved computing, imaging, and scanning technology, photon therapy has undergone tremendous improvement over the past 15 to 20 years. For example, three-dimensional conformal radiation therapy (3D-CRT), intensity modulated radiation therapy (IMRT), image-guided radiation therapy (IGRT), volumetric modulated arc therapy (VMAT), and intensity modulated arc therapy (IMAT), used today in many cancer treatment centers, are some of the external-beam radiation techniques that are taking advantage of the significant computer technology evolution currently happening around the world.

However, the energy-loss characteristic of protons traversing matter shows a lot of potential insofar as optimizing trade-offs between irradiating the target with a high energy conformal beam and limiting the dose to critical structures is concerned [1]. Several authors writing on this topic have shown that proton therapy has all the flexibility of the photon radiation, plus the possibility to control the penetration depth of the proton beam in the target volume [2].

In clinical cancer treatment, proton beams within the therapeutic energy regime of about 50-250 MeV, depending on the depth and or size of the tumour volume in the patient, are used. The common approach is to accelerate protons from their source by using particle accelerators (usually synchrotrons or cyclotrons) to different treatment rooms. Devices such as bending and focussing/defocussing magnets are placed along the beam line to guide the beam to the treatment rooms. As proton therapy continues to grow, researchers around the world have continued the quest for better and more reliable ways of getting the most out of this modality insofar as increasing the probability of curing the cancer is concerned.

1.1 A brief historical background of proton therapy

Since the first medical application of ionizing radiation, in the form of x-rays, was reported in 1895 [3] many technical advancements relating to the manner in which radiation is administered to patients, bearing in mind its effects on biological tissue, have been made. The adaptability of various technologies to the ionizing radiation therapy and the notable evolution in the computing world has led to radiation therapy becoming one of the main treatment options for cancer. The challenge in external-beam radiation method of cancer treatment has always been with how to reduce dose to healthy tissue while increasing or maintaining prescribed dose to target volumes. Techniques such as computerized treatment planning, patient setup, advanced imaging, introduction of intensity-modulated radiotherapy (IMRT), etc., have tremendously transformed the way ionizing radiation is delivered to target volumes in the history of radiation therapy. In addition, dose deposition characteristics of different type of particles can also go a long way in improving beam delivery accuracy [1]. In fact, the medical use of proton beams (and other heavy ions) was first proposed in 1946 by R. H. Wilson [4] primarily because of the physical characteristics of the way they interact with matter. Wilson observed that the well known physics of proton interactions and their energy loss in matter had the potential to enhance delivery of higher radiation doses to the target volumes relative to 'conventional' photon radiation therapy. Protons lose their energy mainly through electromagnetic (EM) interactions with orbital electrons of atoms of the target medium. As the protons slow down, energy transfer to tissue per unit length increases. This leads to almost uniform energy loss over a certain penetration depth (dependent on incident proton energy) but increases sharply to the maximum before a subsequent sharp distal fall off as protons come to a stop (near the end of the range), resulting

in a depth-dose peak commonly referred to as the Bragg peak, Fig. 1.1, (after W. H. Bragg) [5].

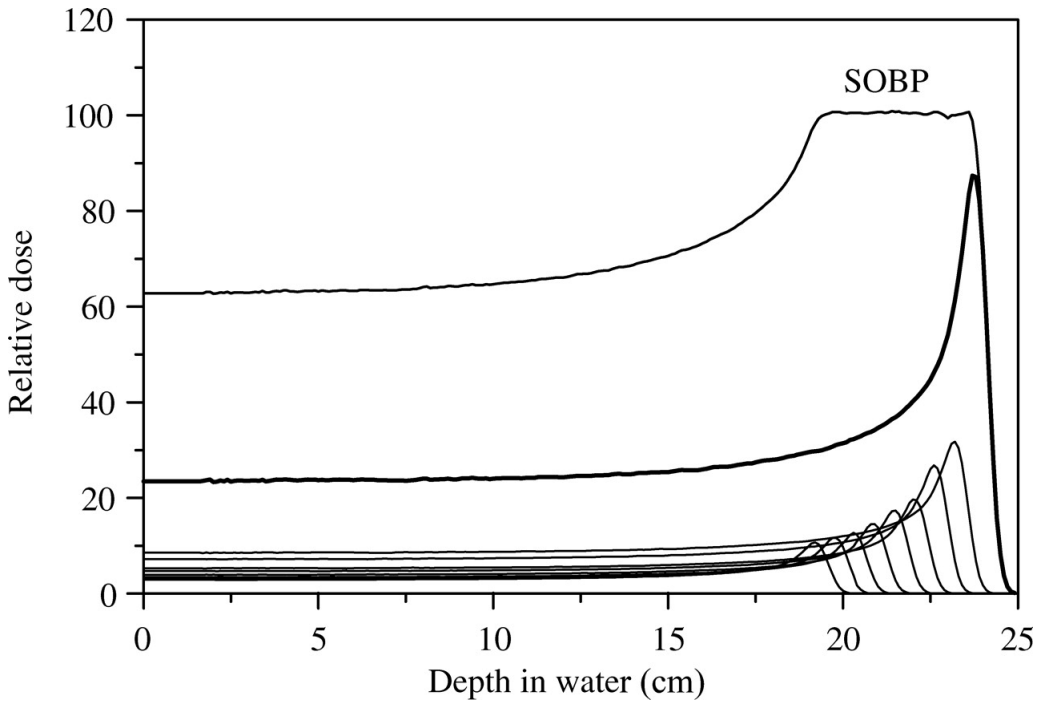

Figure 1.1: *A sharp Bragg peak due to near-monoenergetic proton beams, a SOBP resulting from weighted summation of Bragg peaks of different ranges, and Bragg peaks with varying ranges. Image sourced from [6].*

A near-monoenergetic proton beam exhibits a very narrow Bragg peak, Fig. 1.1. In order to get a Bragg peak that extends longitudinally in width and spreads over the target volume (also known as spread-out Bragg peak (SOBP)), beams of different ranges and weights are added together. Variations in proton beam range can be realized by employing various techniques, such as altering the machine energy or placing an adjustable-degrader, e.g., a double wedge, across the beam line. Wilson also suggested utilizing the Bragg peak and the finite range of proton beams for treating tumours seated deep within healthy tissue or close to critical organs [4].

A couple of years after Wilson first proposed the use of protons (and heavy ions) for cancer treatment, some individuals and institutions began to explore the idea further, first by trying to get an insight on the biological effects of proton radiation. For instance, Lawrence et al. at Lawrence Berkeley Laboratory (LBL) published their work on the biological study of protons on mice in 1952 [7]. Similarly, in 1955 radiation oncologists at Gustav Werner Institute in Uppsala, Sweden, ran experiments on a series of animals (rabbits and goats) [8] [9] to study the biological effect of proton radiation, while at Harvard Cyclotron Laboratory (HCL), extensive relative

biological effectiveness (RBE) [10] [11] studies of protons were done in the 1960s. Initially, the major emphasis for proton therapy clinical research was on dose escalation for tumors which had poor local control with conventional radiotherapy [2].

By the early 1990s, proton therapy was still at the experimental stage, based mainly in research institutions [1]. More work still needed to be done to attain a full-scale use of this treatment modality. For example, many proton machines had limited beam energy, hence could not treat deep seated tumours. They also had fixed horizontal beam lines and limited choice of beam angles, thus patients had to be immobilized and positions reproduced in every treatment session. Early proton therapy facilities employed a passive beam scattering technique, in which beam modifying devices such as rotating range-modulator wheel, optional range-shifter plates, adjustable energy-degrader, scattering filters, range-compensators, were used to, mechanically, obtain a spread-out-Bragg-peak (SOBP) that conform to the target volume. With the evolution in the computer technology and the availability of devices such as the multi-leaf collimator, the passive scattering has transformed into a more automated beam delivery method. For example, beam shaping is now done with computer controlled dynamic multi-leaf collimators [2].

The technological advancements happening around the world coupled with the involvement of commercial companies have given rise to sophisticated equipment associated with proton treatment delivery. Among them are isocentric gantries, which are capable of irradiating a target volume from any arbitrary direction around the patient, accurate imaging equipment such as the PET/CT, which combines a positron emission tomography (PET) scan and a computed tomography (CT) scan, and computerized treatment planning programs. This has made possible the adoption of dynamic proton beam delivery techniques such as spot or pencil beam scanning (also known as the intensity-modulated proton therapy (IMPT)). Compared to passive beam scattering, which uses beam modifying devices to produce a required dose distribution in the target volume, IMPT uses magnets to direct an unmodulated pencil beam from the accelerator (synchrotron) onto the target cross section area (in spot or continuous form) while varying the energy and the intensity to control its penetration depth. IMPT therefore offers proton dose distributions that are highly conformal to the target volume, thereby increasing sparing of the normal tissue. Furthermore, a number of companies around the world today manufacture proton therapy related equipment, making the treatment modality more accessible to the public. The first hospital-based proton therapy facility, equipped with modern technology, e.g., gantries, was opened in October, 1990 at the Loma Linda

University Medical Center (LLUMC) [1]. A few years down the line, more proton therapy centers started mushrooming across the world and the numbers have since been growing steadily [12]. Among the earliest centers to be opened is the iThemba Laboratory for Accelerator-Based Sciences proton therapy facility, which was commissioned in September 1993 in Cape Town, South Africa. It provides a proton beam with maximum energy of 200 MeV which is used for both medical applications and for research purposes [13]. Currently, there are over sixty operational proton therapy centers around the world and over thirty more are scheduled for commissioning within the next two to three years [14].

1.2 Proton dose calculation algorithms

The wide acceptance proton therapy is currently receiving across the globe has heightened the need for accurate and relatively fast dose calculation algorithms. For routine clinical treatment planning, analytical dose calculation algorithms are preferred as they are both feasible and computationally fast compared to Monte Carlo [15] methods. Several forms of proton dose calculation algorithms exist today, the majority of which are based on the pencil beam model [16] [17] [18].

The pencil beam model is a mathematical model attempting to zoom in and assimilate the dose-deposition process of a very narrow (and near-monoenergetic) proton beam in the patient and subsequently approximating the effect of such interaction processes for a broad beam. The pencil beam model, based on the Fermi-Eyges theory of particle transport [19], was first applied to electron dose calculation algorithms by Hogstrom [16]. With suitable modifications however, his formalisms are widely used today in proton pencil beam dose calculation algorithms. Hogstrom defines a pencil beam as a narrow particle beam with infinitesimally small lateral dimension (cross section) impinging at a point on a semi-infinite medium [16]. The dose delivered by the broad beam is approximately equal to the sum of dose deposited by individual near mono-energetic pencil beams. In other words, this approach suggests that a 3D broad beam is made up of an infinitely large number of narrow pencil beams impinging on the surface of the medium [20]. Due to inhomogeneity of the medium, these pencil beams lose their energy differently even though they are subject to similar interaction processes. Several authors have shown that individual pencil beam dose distributions can indeed be summed up to give, approximately, the total dose deposited in the medium by the broad beam [21] [16] [17] [22].

A good proton-dose calculation algorithm must take into account all possible energy loss processes while being both accurate and relatively fast. To date, a number of

algorithms used to predict proton-dose distribution in the patient have been developed using different approaches [17] [18] [23] [22] [21] [24] [25]. While the majority of these dose-calculation algorithms have to some extent compromised accuracy for the sake of achieving clinically viable computational speeds, a few of them, e.g., Ulmer's beamlet model, have attempted to take into account all the physics while remaining computationally inexpensive. The rate of energy loss per unit track length (stopping power) in different material have been successfully calculated using the Bethe-Bloch equation (BBE) and the results [26] [27] are widely used to develop relatively fast dose-calculation algorithms. On the other hand, incorporating an algorithm that gives a comprehensive description of multiple Coulomb scattering (MSC) can be quite involved. Various MSC theories e.g., Molière's [28] (known to be the most comprehensive), Highland's [29], Goudsmith and Saunderson's [30], Lewis' [31], etc., exist today. The choice of the MSC theory for a proton dose-calculation algorithm to be used in a treatment planning system (TPS) can depend on the feasibility to incorporate it and/or the trade-offs between the accuracy and the computational speed. Usually, relatively less involved theories, such as Highland's, are employed or minor permissible modifications are made to the original MSC theory in order to achieve a clinically viable analytical dose-calculation algorithm. Literature shows that, with a few exceptions, a large number of proton pencil-beam algorithms in use today either improve on or are a generalization of the Fermi-Eyges theory [16] [32] [33] [34], which is a relatively simple particle-transport theory [19].

1.3 Monte Carlo simulations

Modern approaches to deriving proton-dose calculation algorithms try to use data from Monte Carlo (MC) simulations [25] [35] as these (MC methods) account for all physical processes, thereby providing the most accurate means of approximating proton energy-deposition in matter and the interaction of radiation with matter in general [1] [36]. Besides providing a practical alternative to measured beam profiles, MC methods are capable of simulating scenarios that may prove difficult or impossible to do experimentally [1]. These can also save beam time by reducing the need for experiments. Basically, MC simulations can be used for predicting dose distributions in the patient, studying the physics of proton beams, designing and testing the beam delivery system, for quality assurance purposes, and so on [1] [37].

In general, a MC method (or simulation) is a numerical method for approximating the probability of a certain outcome by using randomly sampled numbers from a probability density function. MC methods are mainly used to find numerical solu-

tions to problems that are too complicated to solve analytically. Random number generators used in modern day computers have very long periods, making them capable of simulating complex stochastic processes before the sampled number sequence eventually repeats itself. Conceptually, a MC algorithm takes as input the numbers sampled randomly from a probability distribution and performs a calculation. In radiotherapy, the probability distribution could represent possible ways a particle might interact in a given step consistent with the laws of physics. The calculation is performed repeatedly over a very large number (N) of samples, thus, allowing the simulation of all possible outcomes. The result is a probability distribution of a certain outcome, which converges as $N \to \infty$. The uncertainty in the result decreases with increasing number of samples taken, N (i.e., $\approx 1/\sqrt{N}$).

Charged particle transport in matter depends on the interaction probabilities (i.e., cross sections) per unit distance [36]. MC methods are widely used today in radiation therapy to simulate physics interactions on a step-by-step basis. At each step of the particle's passage through the medium, the probability of physics interactions and their outcomes is represented by probability density functions, making the simulation equivalent to solving the Boltzmann particle-transport equation for protons [1].

1.3.1 Geant4 Monte Carlo detector simulation toolkit

Geant4 (i.e., GEometry AND Tracking) is an open source Monte Carlo detector simulation toolkit for simulating passage of particles (radiation) through matter [38]. It is developed and maintained by an international collaboration of physicists and software engineers (Geant4 collaboration) from all around the world [39]. The Geant4 code is written in object-oriented C++ programming language and is widely used in high energy physics, space science, nuclear and accelerator physics as well as in medical sciences. Besides offering versatile ways of tracking particles in the medium with realistic magnetic or electric fields, the Geant4 detector simulating toolkit comprises a comprehensive collection of a large variety of particles, physics processes, models and cross-section libraries for particle transport in matter. Because of its complexity, the Geant4 code relies significantly on the optimized computing power of modern computers (e.g., multi-threading) and the extensible nature of object-oriented C++. Moreover, the Geant4 kernel (central unit) is designed to work in conjunction with non-Geant4 graphic systems and interfaces, such as OpenGL, Qt, DAWN, and ROOT, to aid visualization of the geometry and trajectories as well as for data analysis purposes [40] [39] [41]. The Geant4 toolkit therefore allows for development of a program capable of carrying out tasks from the initial problem definition all the way through to the generation of results, or even final plots for

publication [38].

1.4 Objectives and aims

The main aim of this work is to generate pencil beam kernels (i.e., 3D dose distributions in water) by simulating the traversal of proton pencil beams in the energy range of clinical interest (i.e., 50-250 MeV) through water using the Geant4 MC simulation toolkit, and to assess the contribution of primary protons, secondary protons, and heavy recoil ions and other secondary particles to the total absorbed dose. Such investigations will lay a foundation for future development of an in-house MC-based analytical model for pencil-beam kernels (and eventually a pencil-beam dose calculation algorithm) for the iThemba LABS proton therapy program. This work is motivated by the analytical proton beamlet model of Ulmer et al. [35], which is partially implemented in the commercial proton treatment planning system, Eclipse^{TM}, of Varian medical systems[1]. The beamlet model will therefore be used mostly as a reference point. Like in the beamlet model, the energy deposited in water will be sorted into the following categories: primary protons (pp), secondary protons (sp), and a third group comprising heavy recoil ions and other secondaries which will be denoted as (rc). Both the radial and depth-dependent components of the energy deposited by each particle category will be investigated at respective depths and for the longitudinal depth, respectively. To embark on this undertaking, it was necessary to first learn the formalism of the Geant4 detector simulation toolkit and establish an optimized list of the simulation control parameters and physics settings for a robust, fast and accurate MC (Geant4) simulations.

1.5 Thesis structure overview

Chapter 2 discusses the different ways in which proton beams interact with matter. It describes the basic physics of proton energy loss and the production of secondary particles. This chapter ends with a brief explanation of how these interaction processes are included in the Geant4 simulation toolkit.
Chapter 3 covers the mathematical definitions of simple proton beam configurations. It also introduces the mathematical description of dose deposited (the pencil beam kernel) at a given point in the medium by a very narrow proton beam (pencil beam). The rest of the chapter discusses ways different types of particles contribute to the 3D dose deposition by a pencil beam.

[1]Proton Algorithm Reference Guide-Eclipse^{TM}, April 2007.

In chapter 4 the derivation of the analytical proton beamlet model by Ulmer et al. is outlined.
Chapter 5 covers the simulation of the passage of proton pencil beams (of clinical energy range) through water using the Geant4 (MC) toolkit. An optimized simulation parameter list is suggested, the physics models are discussed, and the general setup and settings for the Geant4 simulations are outlined.
Chapter 6 discusses the results from the simulations. A comparison of dose distributions from the Geant4 simulations and the Ulmer beamlet model are also given here.
A conclusion is presented in chapter 7 together with an outline on possible future work.

Chapter 2

Proton interaction mechanisms

The interaction of protons with matter takes place via three distinct processes: they suffer energy loss by electromagnetic (EM) collisions with atomic electrons, multiple Coulomb deflections by atomic nuclei, and sometimes undergo nuclear collisions, in which incident protons inelastically scatter off the medium nucleus, leaving it in the excited state, or physically knock constituent protons, neutrons, or light nucleon clusters out of the nucleus [1]. In this chapter we review the physics of proton interactions with matter.

2.1 Energy loss processes

Protons traversing a given target medium (e.g., water) lose energy mainly through electromagnetic (EM) collisions with atomic electrons, causing them to eventually stop in the medium. Although important only at incident energies far less than the clinical range (below 20 keV [26]), protons also lose energy by elastic EM collisions with atomic nuclei, giving rise to the so-called *nuclear stopping power* S_{nuc} [42].
A proton (or a charged particle) penetrating the medium interacts with the atoms via the Coulomb force, leading to excitation of the atomic electrons or ionization of the atoms (see Table 2.1). This is the main process by which protons traversing matter lose their energy. Apart from that, incident protons can physically eject orbital electrons from the atom (see Table 2.1 and Fig. 2.1(a)). Ejected electrons are called δ-rays and have kinetic energy equivalent to that lost by projectile protons.

As protons slow down in the medium, the rate of energy loss increases, leading to a sharp increase in ionization of the medium atoms near the end of the range, thus leading to the Bragg peak. According to Gottschalk, the range R_0 of a quasi-monoenergetic proton beam is defined as the depth of material at which half the

protons that undergo only EM interactions have stopped [1] [42]. For water, this range can be approximated as

$$R_0 \approx d_{80}, \tag{2.1.1}$$

where d_{80} is the depth in water corresponding to the distal 80% point of the Bragg peak [42] [1]. An incident mono-energetic proton beam may be assumed to be undergoing continuous interactions (hence losing energy continuously) as it penetrates a homogeneous medium. Such an approximation allows for fluctuations in energy loss to be ignored, therefore, the so-called continuous-slowing-down-approximations (CSDA) [35] technique can be used to approximate the range R_{CSDA} of the proton beam in the medium. In the CSDA framework, protons in the incident mono-energetic beam would be assumed to eventually stop at the same depth in the medium. However, whether their initial energy is the same or varies, protons traversing matter have been observed to stop at different points (even if the medium is homogeneous), a phenomenon referred to as *energy* or *range straggling*[1] [26]. Janni [26] explored the theory of straggling and showed that range straggling in light (low Z) and heavy (high Z) materials differ only slightly, meaning that the shape of the Bragg peak almost remains the same when, say, water is replaced by plastic or lead (Pb). Changing the incident proton energy however changes both the peak-to-plateau ratio of the Bragg curve and its shape [25].

2.1.1 The stopping power

The amount of energy lost per unit distance travelled by a charged particle through the medium, also known as the *linear stopping power* $S \equiv -dE/dz$ (MeV/cm), is a function of the incident particle energy and the target material [1]. In proton therapy however, the *mass stopping power* $S/\rho \equiv -dE/\rho dz$ (MeV/(g/cm^2)), defined as the amount of energy lost per unit areal distance, is frequently used. The mass stopping power equation was derived around 1933 by Bethe and Bloch [26]. For an elemental target with atomic number Z and relative atomic mass A, traversed by a projectile of charge ze and velocity $v = \beta c$, S/ρ can be calculated by

$$-\frac{1}{\rho}\frac{dE}{dz} = \frac{4\pi r_e^2 m_e c^2}{\beta^2}\frac{1}{u}\frac{Z}{A}z^2 L(\beta). \tag{2.1.2}$$

The quantity $L(\beta)$ is called the *stopping number*. It accounts for the fine details of the energy loss process. The factor $4\pi r_e^2 m_e c^2/u$ is a material-independent constant

[1] Energy straggling as a result of fluctuations in energy loss, or range straggling to refer directly to the resulting variations in range.

Interaction type	Interaction target	Principal ejectiles	Influence on Projectile	Dosimetric manifestations
Inelastic Coulomb scattering	Atomic electrons	Primary proton, ionization electrons	Quasi-continuous, energy loss	Energy loss determines range in patient
Elastic Coulomb scattering	Atomic nucleus	Primary proton, recoil nucleus	Change in trajectory	Determines lateral penumbra sharpness
Non-elastic nuclear reactions	Atomic nucleus	Secondary protons and heavy ions, neutrons, and gamma rays	Removal of primary proton from beam	Primary fluence generation of stray neutrons, generation of prompt gammas for in `vivo` interrogation
Bremsstrahlung	Atomic nucleus	Primary proton, Bremsstrahlung photon	Energy loss, change in trajectory	Negligible

Table 2.1: *Summary of proton interaction types, targets, ejectiles, influence on projectiles, and selected dosimetric manifestations, Table by [43].*

approximately equal to 0.307075 MeV cm^2 g^{-1}. The constant r_e is the classical electron radius $= 2.817 \times 10^{-13}$ cm, u is the atomic mass unit, and $m_e c^2 \approx 0.511$ MeV is the electron rest energy. The quantity L can be written as

$$L(\beta) = L_0(\beta) + zL_1(\beta) + z^2 L_2(\beta), \tag{2.1.3}$$

where zL_1 is the Barkas correction, and z^2L_2, the Bloch correction. Bethe derived the stopping power theory on the basis of the first-order Born approximation. These corrections account for departures from this approximation, and are important only at low projectile velocities (i.e., lower than velocities of the atomic electrons) [44]. The term L_0 is given by

$$L_0(\beta) = \frac{1}{2}\ln\left(\frac{2m_e c^2 \beta^2 W_m}{(1-\beta^2)I^2}\right) - \beta^2 - \frac{C}{Z} - \frac{\delta}{2}, \tag{2.1.4}$$

where C/Z is the target shell correction, and $\delta/2$, the relativistic density-effect correction, I is the *mean excitation energy* of the target material (discussed in Sec. 2.1.1.1). The factor W_m is the maximum energy that can be transferred to an unbound electron at rest in a single proton-electron collision [1]. It is given by

$$W_m = \frac{2m_e c^2 \beta^2}{1-\beta^2} \times \left[1 + \frac{2m_e}{m_p(1-\beta^2)^{1/2}} + \frac{m_e}{m_p}\right]^{-1}. \tag{2.1.5}$$

The factor in the square brackets is nearly unity and contributes only at relativistic energies. For clinical incident energy range, Eq. (2.1.8) is a reasonably accurate

approximation for the full relativistic description.
The density-effect δ and the shell correction C are important only at high and low energies respectively [45]. The density-effect δ arises from the fact that a proton polarizes the atoms along its path, leading to the disturbance in the electron field which in turn reduces the influence of the outer lying electrons on the proton energy loss [26] [45]. The density-effect becomes more important at incident energies far beyond the clinical energy regime and for high medium densities. On the other hand, the shell correction accounts for effects arising when the incident particle velocity becomes less or equal to the orbital velocity of the bound electrons. At such energies, the assumption that the electron is at rest relative to the incident particle is no longer valid and the Bethe-Bloch formula without the shell correction term breaks down [45].

2.1.1.1 The mean excitation potential

The mean excitation energy (or ionization potential) I of the target material is a material dependent quantity and by far the main source of uncertainty in the clinical energy range [1]. In practice, it is very difficult to calculate I with sufficient accuracy. Therefore, it is usually obtained by fitting measured range-energy values (for materials where data exists) or interpolated with the guidance of the theory [42] (in cases where measurements are unavailable). For media of unknown ionization potential, Bragg's additivity rule:

$$\frac{S}{\rho} = \sum_i w_i \left(\frac{S}{\rho}\right)_i, \tag{2.1.6}$$

is used. Here, the term w_i is the fraction by weight of the i^{th} element. Bragg's additivity rule suggests that mass stopping power for mixtures or compounds can be estimated by the linear combination of the stopping powers of the constituent elements [46]. However, because of the significant influence the chemical bonding in compounds has on the mass stopping power Eq. (2.1.6) is largely an approximation. Range-energy tables can slightly differ depending on the author's choice for the I value. In Geant4, I values recommended by ICRU [44] are used [47].

Overall, the Bethe-Bloch formula is accurate enough for the radiotherapy energy regime and it is permissible to omit most of these corrections [1] in this energy range. Eq. (2.1.2) can therefore be used in its simplest or non-relativistic form:

$$\frac{S}{\rho} \equiv -\frac{1}{\rho}\frac{dE}{dz} = 0.307075\frac{Z}{A}\frac{1}{\beta^2}\left(\ln\frac{W_m}{I} - \beta^2\right)\frac{MeV}{g/cm^2}, \tag{2.1.7}$$

with

$$W_m = \frac{2m_e c^2\beta^2}{1-\beta^2}. \tag{2.1.8}$$

At very low energies (e.g., $\lessapprox$ 2 MeV), this formula is no longer accurate, therefore, the corrections must be implemented. Implementing these corrections can be quite involved mathematically, especially in the already complicated MC codes. Several authors [46] [26] [44] have calculated the mass stopping powers of various material for clinical incident proton energy range which are today tabulated into range-energy tables, e.g., of Janni [26], ICRU report 49 [27], etc. These look-up tables are used in most MC codes today, which would otherwise take very long to execute.

In the Geant4 toolkit, the Bethe-Bloch equation is used to calculate the hadron energy loss down to 2 MeV, below which a parameterization based on the ICRU report 49 [44] is implemented [48]. In Geant4, any interaction process calculates the continuous and discrete energy loss in the medium. Above a given energy threshold (range cut) the energy loss of the particle is simulated by the explicit production of secondary particles (gammas, electrons, positrons, protons, etc.) while below the threshold, the energy loss is treated as continuous [47]. Therefore, if a given particle suffers continuous energy loss via several processes, the total continuous part of the energy loss will be the sum. In order to speed up the simulations, the continuous energy loss (which occurs at very low energies depending on the user-defined cut-off value) is pre-calculated during the initialization phase of the Geant4 simulation and stored in the dE/dz table. The ranges of the particle in a given material are then calculated using this table and stored in the *Range* table, which eventually is inverted into the *InverseRange* table. At run time, values of the continuous energy loss and range are obtained using these tables. Discrete energy loss is not involved at this stage. In contrast to the continuous energy loss, the production of secondary particles above the production threshold is sampled explicitly by each energy loss process [47].

2.2 Multiple Coulomb scattering

Protons passing through matter may also get deflected by atomic nuclei, a process commonly referred to as *scattering*, more precisely, *multiple Coulomb scattering* since the observed angular dispersion is due to a cumulative effect of many random small single-scatterings. Both the proton and the nucleus have a positive charge, as such, their interactions are largely electrostatic in nature (as a result of the Coulomb force acting between them, see (b) in Figure 2.1). Such large numbers of small single-deflections are better treated statistically. The overall spatial distribution tends towards a Gaussian (Figs. 2.2a and 2.2b) provided the scattering events occur at small angles, a condition largely satisfied by protons traversing a low Z medium such

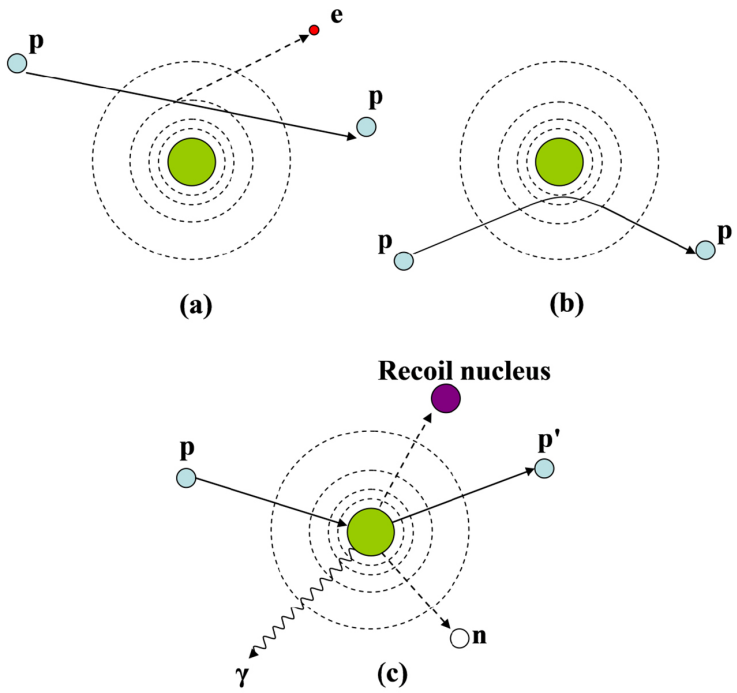

Figure 2.1: *Schematic illustration of proton interaction mechanisms: (a) energy loss via inelastic Coulomb interactions, (b) deflection of proton trajectory by repulsive Coulomb elastic scattering with nucleus, (c) removal of primary proton and creation of secondary particles via non-elastic nuclear interaction (p: proton,e: electron, n: neutron, γ: gamma rays). Image from Newhauser [43].*

as water or plastic [1].

Several theories of multiple scattering have been developed since the 1930s [28] [1]. In the Gaussian approximations the main focus is the dependence of the *mean scattering angle* θ_0 on proton energy and scattering material as well as its thickness. The so-called Molière's *characteristic multiple scattering angle* θ_M, given by

$$\theta_M = \frac{1}{\sqrt{2}}(\chi_c\sqrt{B}) \tag{2.2.1}$$

is analogous to θ_0 [1]. In Eq. 2.2.1, χ_c is the *characteristic single scattering angle*. For an incident proton (charge number z, momentum p, speed v) passing through a significantly thin target (t:thickness$\ll$proton range) consisting of a single element (atomic weight A, atomic number Z), χ_c can be written as

$$\chi_c^2 = c_3 t/(pv)^2, \tag{2.2.2}$$

where

$$c_3 \equiv 4\pi N_A \left(\frac{e^2}{\hbar c}\right)^2 (\hbar c)^2 \frac{z^2 Z^2}{A}, \tag{2.2.3}$$

and B is the reduced target thickness,

$$B - \ln B = b, \tag{2.2.4}$$

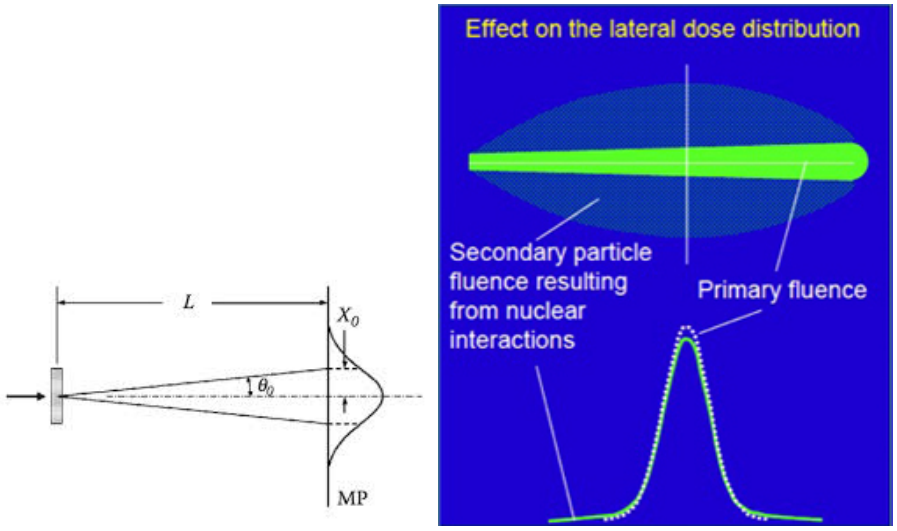

(a) *MCS in thin slab.MP-Measuring plate.* **(b)** *Lateral scattering due to MCS yields a Gaussian.*

Figure 2.2: *Multiple Coulomb scattering resulting from proton interactions with nuclei of medium atoms (images from [1] and [49] respectively).*

$N_A \approx 6.022 \times 10^{23}$ mol^{-1} is Avogadro's number, $e^2/\hbar c \approx 1/137$ is the fine structure constant, and $\hbar c \approx 197 \times 10^{-13}$ MeV cm is the conversion factor. The quantity b is the natural logarithm of the effective number of collisions in the target. The physical interpretation of χ_c is that, on average, a proton suffers exactly one single scatter greater than χ_c in its traversal of the target [1].

Defining a reduced angle,

$$\theta' \equiv \frac{\theta}{\chi_c \sqrt{B}} \tag{2.2.5}$$

Molière approximates the angular distribution function $f(\theta)$ of the proton space angle θ by a power series in 1/B:

$$f(\theta) = \frac{1}{2\pi\theta_M^2}\frac{1}{2}\left[f^{(0)}(\theta') + \frac{f^{(1)}(\theta')}{B} + \frac{f^{(2)}(\theta')}{B^2}\right] \tag{2.2.6}$$

where the $f^{(n)}$ are given by

$$f^{(n)}(\theta') = \frac{1}{n!}\int_0^\infty y dy J_0(\theta' y) e^{y^1/4}\left(\frac{y^2}{4}\ln\frac{y^2}{4}\right)^n. \tag{2.2.7}$$

and $f^{(0)}$ is a Gaussian:

$$f^{(0)}(\theta') = 2e^{-\theta'^2}. \tag{2.2.8}$$

A good summary of Molière's theory is given in [1], while the detailed theory is in the original papers [28]. Although given here in brief, it can be clearly seen that Molière's theory is mathematically complicated.

In subsequent years continuous improvements or re-evaluation of some of these scattering theories has been on the rise, with the view of arriving at accurate but easier to evaluate formulae for purposes of clinical dose calculation algorithms. Examples of such undertakings include Highland's formula [29], which he derived by parameterizing the full Molière/Bethe/Hanson theory, and Urbàn model [50], which is based on the Lewis theory of multiple Coulomb scattering [31].
Highland's formula calculates the *mean scattering angle* θ_0 as

$$\theta_0 = \frac{14.1\text{MeV}}{pv}\sqrt{\frac{L}{L_R}}\left[1+\frac{1}{9}\log_{10}\left(\frac{L}{L_R}\right)\right]rad, \tag{2.2.9}$$

where pv is the kinematic factor given by Eq. (A.0.6), L is the target thickness, and L_R is the radiation length of the target material [1]. The radiation length is the distance over which the incident particle's energy is reduced by a factor $e^{-1}(\approx 0.37)$ due to radiation losses alone [51]. This scattering angle is integrated along the beam axis (z-axis), and the lateral standard deviation at depth z (for beam axis coinciding with the z-axis) can be given by

$$\sigma^2_{x,\text{MCS}}(Z) = \left[1+\frac{1}{9}\log_{10}\left(\frac{z}{L_R}\right)\right]^2 \times \left[\int_0^z \left(\frac{14.1\text{MeV}}{pv}\times(z-z^{'})\right)^2 \frac{1}{L_R}dz^{'}\right]. \tag{2.2.10}$$

Another theory very appropriate for describing the spatial and angular distributions of protons traversing matter is the Fermi-Eyges theory [19]. The Fermi-Eyges theory is a relatively simple theory that describes the propagation of a particle beam through matter. It gives the solution to the Fermi equation which in turn derives from the more fundamental linear Boltzmann equation in two steps [52]: First, with the assumption that the scattering of interacting particles occur over small angles, the Boltzmann equation is approximated by the Fokker-Planck equation. Second, the Fokker-Planck equation is reduced to the Fermi equation by assuming continuous energy loss of the penetrating particle (CSDA), that is, the energy of incident particle is a well defined and continuous function of the penetration depth [52] [33]. Ideally, the angular distribution of protons in a given medium approximates a Gaussian for small angles (see Figs. 2.2a and 2.2b) followed by a scattering tail, which is effectively governed by the small-angle Rutherford scattering, with $d\sigma/d\Omega \approx 1/\theta^4$. The Fermi-Eyges theory was initially applied to pencil beam algorithms for electron beams by Hogstrom [16].
The Fermi-Eyges theory approximates the lateral spread of an initially parallel and infinitesimally narrow proton beam as a function of depth in water, z (in centimeters), to a Gaussian of width

$$\overline{x^2_{\text{MCS}}(z)} = \sigma^2_{x,\text{MCS}} = \int_0^z (z-z^{'})^2 T(z^{'})dz^{'}[\text{cm}^2], \tag{2.2.11}$$

where the lateral variance of the beam,

$$\overline{x^2_{\mathrm{MCS}}(z)} = \sum_{i=1}^{\mathrm{N}} x_i^2/\mathrm{N} \tag{2.2.12}$$

is equal to the square of the standard deviation of the Gaussian profile ($\sigma^2_{x,\mathrm{MCS}}(z)$), in the limit of many scattering events (N), and

$$T(z) \equiv \overline{d\theta^2}/dz \tag{2.2.13}$$

is the scattering power [1], simply defined as the rate of increase of the variance of the MCS angle [53]. However, the commonly used formula for the scattering power is the parameterization,

$$\begin{aligned} T(z) = T_{dm} \quad &= [0.524 + 0.1975\log_{10}(1-(pv/p_1v_1)^2) + 0.2320\log_{10}(pv/\mathrm{MeV}) \\ &\quad -0.0098\log_{10}(pv/\mathrm{MeV})\log_{10}(1-(pv/p_1v_1)^2)] \times \left(\tfrac{E_s}{pv}\right)^2 \tfrac{1}{L_R}, \end{aligned} \tag{2.2.14}$$

which is called the improved non-local formula, as given by Gottschalk [53]. Here, pv[MeV] is the product of the proton momentum and velocity and is a function of z; p_1v_1 is the initial product of momentum and velocity, $E_s = 15.0$ MeV, and L_R is the radiation length (36.1 cm for water) [1].

In the Gaussian approximation, each pencil beam evolves in water according to $\sigma_{x,\mathrm{MCS}}(z)$ such that at any depth z the total distribution can be explained in terms of the convolution of two Gaussian functions: the initial unperturbed Gaussian shape and the additional spreading due to MSC in the medium [1].

2.2.1 Multiple Coulomb scattering in Geant4

In order to optimize speed in MC simulations, condensed algorithms are used instead of the detailed algorithms. Detailed simulation algorithms account for every collision/interaction that a simulated particle experiences. A simulation by a detailed algorithm can be considered exact, i.e., it gives the same results as the solution of the transport equation [50]. Because the detailed algorithm simulates every interaction, it can only be used for simulations which involve a small number of collisions, such as the interaction of low energy projectiles with thin foils, or low density gas [50]. On the other hand, condensed simulation algorithms simulate global effects (such as the net energy loss, displacement and change of direction of the charged particle) of the collisions at the end of the step (or track segment). Condensed simulation algorithms are used to simulate high energy particle transport in solid or liquid media where the average number of collisions is very large such that the detailed

simulation becomes inefficient [50]. The displacement and the change of direction of the penetrating particle are calculated by MSC algorithms that are incorporated in the transport codes. The accuracy of these algorithms is limited by the accuracy of the approximations used in MSC models.

The MSC model used by default in the Geant4 toolkit (since version 10.0) is the `G4UrbanMscModel`, developed by L. Urbàn [50]. The Urbàn MSC model belongs to the class of condensed simulation algorithms and is applicable to all types of particles at any energy. It is based on the Lewis model of MSC [31], i.e., it uses model functions that have been chosen in such a way as to give the same moments of angular and spatial distributions after a step as the Lewis model [50]. Compared to the Lewis model, the MSC theories of Molière, Goudsmit-Saunderson [30], etc., only determine the angular distribution after a step, they do not compute the moments of the spatial distributions. The `G4UrbanMscModel` simulates the scattering of the charged particle after a given step, computes the path length correction and the lateral displacement of the particle penetrating the medium [50]. Below (Sec. 2.2.2) we briefly discuss the Lewis theory and give a short overview of the Urbàn model.

2.2.2 The Urbàn model of multiple Coulomb scattering

The Lewis theory describes a direct method of obtaining exact results from the diffusion equation of the multiple scattering of charged particles traversing an infinite and homogeneous medium, without the usual small-angle approximation. In the development of the theory, Lewis carried out an expansion of the cross-section for scattering in spherical harmonics, leading to a diffusion equation that rapidly converges in the case of large-angle scattering when integrated over all space, and whose coefficients can be exactly determined. The determination of the coefficients leads to expressions for various moments of spatial and angular distributions. Lewis also showed that his angular distribution result can be transitioned to cases in which only the small-angle scattering is important [31].

Based on the Lewis theory of multiple scattering, Urbàn developed a model for MSC to be used in the Geant4 toolkit. The model uses the *transport mean free paths*, λ_i, to determine properties of the MSC process. The i-th transport mean free path is given by

$$\frac{1}{\lambda_i} = 2\pi n_a \int_{-1}^{1} [1 - P_i(\cos\chi)] \frac{d\sigma(\chi)}{d\Omega} d(\cos\chi), \tag{2.2.15}$$

where $d\sigma(\chi)/d\Omega$ is the differential cross section for scattering, $P_i(\cos\chi)$ is the i-th Legendre polynomial, and n_a is the number of atoms per volume. Instead of using the cross section directly, the model uses the first and second transport mean free

paths (λ_1 and λ_2) to compute the different spatial and angular distributions. The straight distance between the endpoints of a step is called the *geometrical path length* ℓ, while the total length travelled by a particle is referred to as the *true path length* t. In order to accurately describe the transport of a particle in matter, the step limitation imposed by the physics processes and the geometry of the detector are compared and the minimum step length is selected as the actual step length. The role of the MSC algorithm in this capacity is to transform the minimum 'physics step length' into 'geometrical step length' (i.e., $t \rightarrow \ell$, also known as the inverse of the path length correction). Once the actual step length is determined and the particle position has changed, the MSC carries out the path length correction: the transformation $\ell \rightarrow t$, since the energy loss and scattering computation need the true step length t. For instance, at the end of this step length (t) the scattering angle θ of the particle is sampled according to the model function, and lateral displacement is calculated using the equation (for a particle with the initial direction parallel to the z-axis)

$$\langle x^2 + y^2 \rangle = \frac{4\lambda_1^2}{3}\left[\tau - \frac{\kappa+1}{\kappa} + \frac{\kappa}{\kappa-1}\mathrm{e}^{-\tau} - \frac{1}{\kappa(\kappa-1)}\mathrm{e}^{-\kappa\tau}\right], \tag{2.2.16}$$

where $\tau = t/\lambda_1$ and $\kappa = \lambda_1/\lambda_2$. The lateral correlation given by

$$\langle x\upsilon_x + y\upsilon_y \rangle = \frac{2\lambda_1}{3}\left[1 - \frac{\kappa}{\kappa-1}\mathrm{e}^{-\tau} + \frac{1}{\kappa-1}\mathrm{e}^{-\kappa\tau}\right] \tag{2.2.17}$$

determines the direction of the lateral displacement. In Eq. (2.2.17) υ_x and υ_y are the x and y components, respectively, of the direction unit vector [50].

Step limitation algorithms are also implemented in the transport process of this model to keep the particle from crossing the volume in one step or to restrict the step size of the particle entering a new volume for the sake of good simulation of backscattering. Similarly, boundary crossing is treated by a stepping algorithm which prevents the last step of the particle from being bigger than the mean free path of elastic scattering in the given volume. This restricts the particle to single scattering at or very close to the boundary [50].

The reliability of the Geant4 MC simulations under the implementation of the Urbàn MSC model has been tested against experimental and Geant3[2] simulation results, which implemented Molière's theory [54] [55]. Some benchmarking comparisons have been done for the scattering angle distribution, energy deposit distribution in detectors, transmission of charged particles, backscattering of charged particles, etc., in

[2] A predecessor of Geant4, it was written in FORTRAN.

different media. Overall, with the implementation of the Urbàn MSC model, Geant4 simulation results agree with experimental data within experimental uncertainties.

Molière's theory is well known for reproducing the Gaussian type of angular distribution at small angles and the Rutherford-like scattering at large angles. The Lewis theory equally gives a good description of the long single-scattering tail in addition to Gaussian distribution for small-angle scattering. There is yet to be an authoritative comparison of the two theories, as such we cannot categorically state which theory is more accurate. However, the outstanding difference is that one theory (Molière's) calculates only the angular distribution of a particle at the end of the step whereas the other (Lewis') computes the spatial distribution as well. It suffices to observe that compared to the Geant3 (which implemented Molière's theory) simulations, the Geant4 (using the Urbàn model) simulation results give better agreement with experimental data [54] [55].

2.3 Nuclear interactions

Incident protons can also undergo elastic or nonelastic collisions with the atomic nuclei of the medium. In elastic collisions the projectile proton physically scatters off the target nucleus while maintaining its total kinetic energy. Nonelastic collisions on the other hand can physically knock nucleons or light nucleon clusters out of the target nucleus, leaving the nucleus in the excited state. The excited nucleus subsequently decay by emitting nucleons or γ-rays, or by undergoing β^-/β^+ decays [45]. Possible products of nonelastic nuclear interactions comprise protons, neutrons, electrons, gammas, heavy fragments such as alphas, and recoiling residual nuclei (see Table 2.1 and Fig. 2.1 (c)), generally referred to as secondaries or secondary particles [42]. Since the medium considered here is water, nonelastic interactions in the energy range of clinical interest are predominantly with the oxygen nuclei:

$$\left.\begin{array}{lll}
\mathrm{p} + {}^{16}_{8}\mathrm{O} \rightarrow \mathrm{p} + \mathrm{n} + {}^{15}_{8}\mathrm{O} & \text{or} & {}^{16}_{8}\mathrm{O}(\mathrm{p},\mathrm{pn}){}^{15}_{8}\mathrm{O} \\
\mathrm{p} + {}^{16}_{8}\mathrm{O} \rightarrow \mathrm{n} + {}^{16}_{9}\mathrm{F} & \text{or} & {}^{16}_{8}\mathrm{O}(\mathrm{p},\mathrm{n}){}^{16}_{9}\mathrm{F} \\
\mathrm{p} + {}^{16}_{8}\mathrm{O} \rightarrow \mathrm{p} + \mathrm{p} + {}^{15}_{7}\mathrm{N} & \text{or} & {}^{16}_{8}\mathrm{O}(\mathrm{p},2\mathrm{p}){}^{15}_{7}\mathrm{N} \\
\mathrm{p} + {}^{16}_{8}\mathrm{O} \rightarrow \alpha + {}^{13}_{7}\mathrm{N} & \text{or} & {}^{16}_{8}\mathrm{O}(\mathrm{p},\alpha){}^{13}_{7}\mathrm{N} \\
\mathrm{p} + {}^{16}_{8}\mathrm{O} \rightarrow \mathrm{d} + {}^{15}_{8}\mathrm{O} & \text{or} & {}^{16}_{8}\mathrm{O}(\mathrm{p},\mathrm{d}){}^{15}_{8}\mathrm{O} \\
\mathrm{n} + {}^{16}_{8}\mathrm{O} \rightarrow \mathrm{p} + {}^{16}_{7}\mathrm{N} & \text{or} & {}^{16}_{8}\mathrm{O}(\mathrm{n},\mathrm{p}){}^{16}_{7}\mathrm{N} \\
\mathrm{n} + {}^{16}_{8}\mathrm{O} \rightarrow \mathrm{p} + \mathrm{n} + {}^{15}_{7}\mathrm{N} & \text{or} & {}^{16}_{8}\mathrm{O}(\mathrm{n},\mathrm{pn}){}^{15}_{7}\mathrm{N} \\
\mathrm{n} + \mathrm{p(H)} \rightarrow \mathrm{n} + \mathrm{p(recoil)} & \text{or} & {}^{1}_{1}\mathrm{H}(\mathrm{n},\mathrm{n}){}^{1}_{1}\mathrm{H}
\end{array}\right\} \quad (2.3.1)$$

The proton-oxygen cross-section for nonelastic nuclear reactions has a threshold energy of $E_{Th} = 7$ MeV, which is the energy required to overcome the repulsive Coulomb barrier [56] [57].

Explicit evaluation and theoretical modelling of nuclear interactions, as has been done for stopping and scattering processes, proves mathematically challenging. Their dose contribution is however significantly low compared to that of primary protons (see Fig. 2.3) [58] [59]. In some analytical pencil beam algorithms, the effects of nuclear interactions on the total dose distribution are assumed to be small and often accounted for by using measured depth-dose distributions. Studies previously

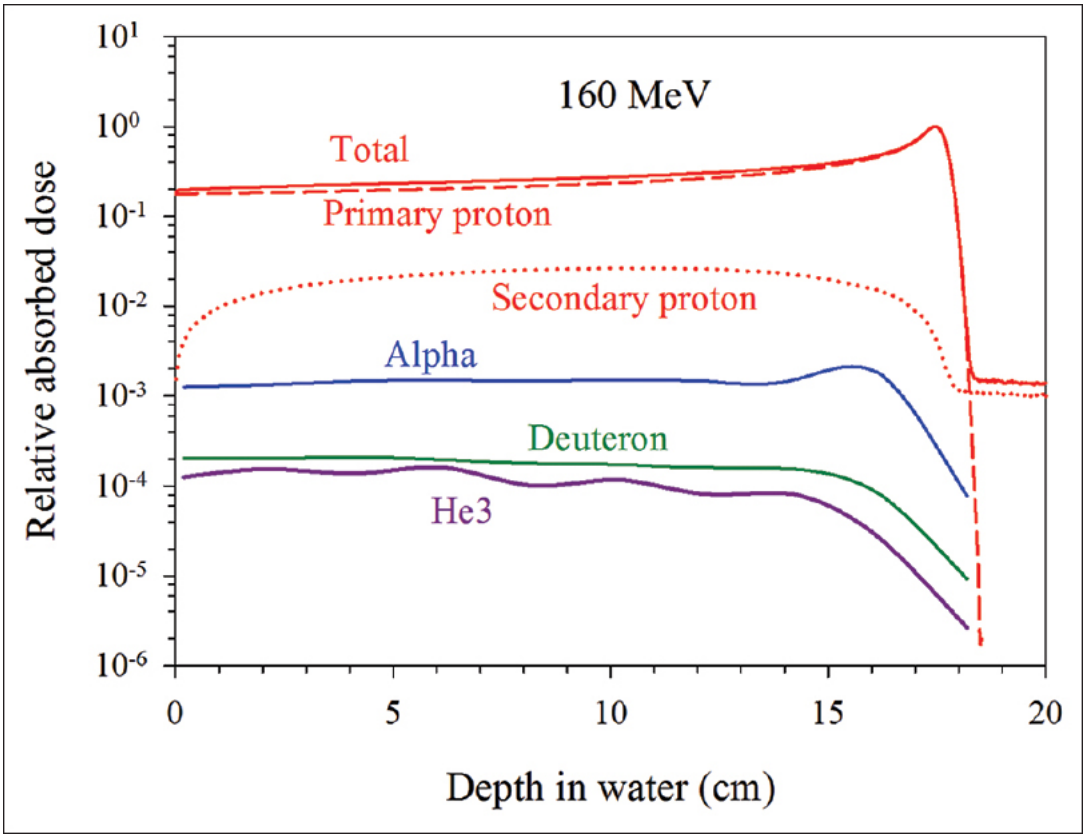

Figure 2.3: *Depth-dose distribution for 160 MeV proton beam incident on a water phantom. Also plotted are the individual dose contributions of the primary protons and the secondary particles (Image from [60]).*

conducted to investigate the influence of nonelastic nuclear interactions on dose distribution [58] [59] [60] show that nonelastic nuclear interactions remove primary protons from the incident beam, thereby decreasing the peak-to-plateau ratio of the total depth-dose distribution. Furthermore, generated secondary particles (except for neutrons) have short range and large scattering angles [1] [42]. Another influence nonelastic nuclear interactions have on the depth-dose distribution, especially

at high incident proton energies ($\gtrapprox$200 MeV), is a dose build-up effect observed in the entrance region of the Bragg curve [61]. The build-up effect is partly caused by the Landau tails in the proton-electron energy transfer [35] (see Sec. 4.2). All these factors have to be included in a dose calculation algorithm if a more accurate result is to be achieved.

2.3.1 Including nuclear interactions in Geant4 simulations

With its flexible framework for modular implementation of physics processes, the Geant4 toolkit is capable of putting together various kinds of hadronic interaction modules[3]. These modules describe the elastic scattering, inelastic scattering, nuclear interactions and the transport of secondary particles. In MC codes nuclear interactions are usually taken into account by using the total nonelastic nuclear interaction cross-section and branching ratios of different reaction channels liberating secondary particles [58]. In Geant4, hadronic interaction cross-sections are either tabulated, parameterized using analytical functions, or deduced from other cross-sections via general nuclear physics principles [58].

To model nonelastic nuclear interactions, one can assume an incident proton interacting with nucleons in the target nucleus, thereby liberating secondary nucleons and leaving the nucleus in an excited state (also known as the intra-nuclear cascade phase). Subsequently, the nucleus de-excites to equilibrium by emitting nucleons, and the residual nucleus can de-excite further (e.g., by evaporation) [48]. To simulate these processes, selected models are applied to different phases (e.g., intra-nuclear cascade, pre-equilibrium, and equilibrium) of the nuclear system as it evolves with time. Within the clinical energy range, the binary cascade and the Bertini cascade models for inelastic nuclear scattering of protons, neutrons, and heavier ions are known to give comprehensive description of the intra-nuclear cascade phase [48]. However, in the present work we follow the recommendations of Jarlskog et al. [48] and choose the binary cascade model over the Bertini cascade model for reasons that the latter gives a less accurate description of the target by considering it to have discontinuous nuclear density distributions and potentials, uses entirely classical calculation of scattering, is devoid of Coulomb barrier simulation, and disregards nuclear momenta in calculations of reaction cross-sections. The binary cascade model also automatically invokes the `G4PreCompoundModel` (used to simulate the de-excitation of the nucleus in the pre-equilibrium phase) when energy of particles in the intra-cascade phase reaches a lower limit, whereas the Bertini cascade model invokes its

[3]Note that term 'module' is used here to refer to a collection of models that work together to achieve a particular result.

own 'pre-equilibrium model', which is less accurate compared to the former [62] as shown by Quesada et al. [62]. At equilibrium, several de-excitation models are present (see Table 5.2) through the `G4ExcitationHandler` but for therapeutic proton interaction with water the evaporation model (`G4VEvaporation`) is sufficient [48]. Table 5.1 gives, among others, physics processes, models and data sets used in Geant4 to describe nuclear interactions.

Chapter 3

Simple proton beam configurations

In order to derive a satisfactory mathematical description of particle transport in matter, beam and geometric configurations must be explicitly defined. Simple beam configurations range from pencil beams (sometimes referred to as *point-monodirectional* beams or beamlets [32]) to broad beams. Pencil beam here means that spatial and angular dimensions of the proton beam are infinitesimally narrow at the point the beam impinges onto the medium. Similarly, in the plane-parallel beam configurations, individual proton pencil beams are assumed to be incident normally onto the plane surface of the medium. Simple beam configurations such as pencil beams are widely used in developing dose calculation algorithms for particle beams as they give a basis on which mathematical models for more realistic beam configurations can be derived [22].

3.1 Pencil beam kernels

The introductory part of the mathematical description of simple proton beam configurations is given in Appendix B.3. A pencil beam can be derived from the plane-parallel beam such as Eq. (B.3.3) by limiting the target surface area onto which the beam is incident. If we assume a narrow beam of monoenergetic particles incident on a small area $\delta A = \delta x \delta y$ on the $x-y$ plane at $z = 0$, the dose deposited by such a pencil beam at some point $\vec{r}$ in the medium can be written as

$$D_{pb}(\delta A; \vec{r}) = \Phi'_{pp} \int \int_{\delta A} \mathfrak{D}_{pb}\big(E; x - x', y - y', z\big) dx' dy'. \tag{3.1.1}$$

Here, it is assumed that the energy spectrum of the source protons is uniform throughout the small area δA, i.e.,

$$\Phi'_{pp}(x', y', E) = \Phi_{pp} \psi_{pp}(E) \quad \forall (x', y') \in \delta A, \tag{3.1.2}$$

where Φ_{pp} and $\psi_{pp}(E)$ are the fluence and the normalized energy distribution of the initial protons respectively. Eq. (3.1.1) follows from Eq. (B.3.3) and is only valid for a homogeneous semi-infinite medium, it is therefore a limiting case of a plane-parallel beam [63]. In Eq. (3.1.1), the pencil kernel $\mathfrak{D}_{pb}$ is given by

$$\mathfrak{D}_{pb}(\vec{r}) = \int_0^\infty \psi_{pp}(E)\mathfrak{D}_{pp}(E;\vec{r}). \tag{3.1.3}$$

The dose deposited in the homogeneous semi-infinite area $\Omega(z)$ (symmetric to the initial beam direction) by each pencil beam can be summed up to approximate the dose of an arbitrary broad beam:

$$D(x,y,z) = \int_0^{E_{max}} dE \int\int_{\Omega(z)} \Psi\big(E;x^{'},y^{'}\big)\mathfrak{D}_{pb}\big(E;x-x^{'},y-y^{'},z\big)dx^{'}dy^{'}. \tag{3.1.4}$$

The integration is over the limits of the area $\Omega(z)$, conformal to the target volume, onto which a collection of parallel PBs are incident normally [16]. The term Ψ is the relative strength or energy fluence of the PBs at $x^{'},y^{'}$. It depends on the incident proton energy, the material and the geometry of elements in the beamline. Therefore, algorithms used to calculate the energy fluence usually involve modelling of the geometry and material of the beamline configurations, a topic beyond the scope of the current work. Hong et al. [17] developed such an algorithm to account for effects of elements upstream of the patient, and of the air gap between them and the patient, on the absorbed dose. The quantity $\mathfrak{D}_{pb}$ denotes the dose distribution at the point $\vec{r}$ in the medium by the monoenergetic PB of energy E [16]. Throughout the rest of this work we will refer to $\mathfrak{D}_{pb}$ as the pencil beam kernel. The maximum penetration depth of the pencil beam kernel depends largely on the incident proton pencil beam energy and the density of the target [1]. It is however, independent of the effects of elements upstream of the target. The primary focus of this work is to model the three-dimensional proton pencil beam kernel $\mathfrak{D}_{pb}$.

At any arbitrary point $p(x,y,z) = p(r,\phi,z)$ in three-dimensional space, the PB kernel takes the form

$$\mathfrak{D}_{pb}(E;x,y,z) = \mathfrak{D}_{pb}(E;r,\phi,z) = \mathfrak{D}_{pb}(E;r,0,z) = \mathfrak{D}_{pb}(E;r,z) \tag{3.1.5}$$

$$\forall\, \phi \in \big(0,2\pi\big] \text{ and } \forall\, z \in \mathbb{R}.$$

Here, (r,ϕ,z) are the cylindrical coordinates, and $r = \sqrt{x^2+y^2}$. The PB kernel $\mathfrak{D}_{pb}(r,\phi,z)$ is radially symmetric about the z-axis or direction of propagation of the PB, therefore, does not depend on the azimuthal angle ϕ. Furthermore, $\mathfrak{D}_{pb}$ can be written as a product of the depth dependent term $g(z)$ and the off-axis term $f(E;x,y,z) = f(E;r,z)$ [16] [17] [32] [18] as

$$\mathfrak{D}_{pb}(E;r,z) = f(E;r,z)g(E;z). \tag{3.1.6}$$

The off-axis term $f(x, y, z)$ describes the lateral spread of the primary proton PB as a function of penetration depth, a phenomenon resulting from multiple Coulomb scattering (MSC) and range straggling [16] [1]. The depth-dependent term $g(z)$ corresponds to the central-axis of the broad beam measured in water. Therefore, it is usually obtained from measured depth dose distributions of broad beams in the water phantom [16] [17].

3.2 Pencil beam kernel decomposition

In this work we treat the total dose deposited in the medium as a sum of the contributions from three categories of particles: *primary protons* (pp), *secondary protons* (sp), and the rest of the particles and residual nuclei (e.g., deuterons, tritons, α-particles, ^{3}He) put together into a group we loosely call *recoil* (rc) *ions*. A similar approach was taken in the dose calculation algorithm developed by Ulmer et al. [32] (see Ch. 4). Let us denote these categories of particles as:

$1 = pp \rightarrow$ primary protons,

$2 = sp \rightarrow$ secondary protons,

$3 = rc \rightarrow$ recoil and other secondary charged particles heavier than protons (e.g., deuterons, tritons, α-particles, ^{3}He).

The absorbed dose can therefore be decomposed into components corresponding to dose from each category of the interacting particles as follows (we will assume $\mathfrak{D}_{pb}$ is implied (i.e., $\mathfrak{D} = \mathfrak{D}_{pb}$) as well as the dependence of $\mathfrak{D}_{pb}$ on E, r and z)

$$\mathfrak{D} = \mathfrak{D}_{pp} + \mathfrak{D}_{sp} + \mathfrak{D}_{rc} \tag{3.2.1}$$

$$= \sum_{i=1}^{3} \mathfrak{D}_i \tag{3.2.2}$$

$$= \sum_{i=1}^{3} f_i(E; r, z) g_i(E; z), \tag{3.2.3}$$

where $f_i(E; r, z)$ and $g_i(E; z)$ are the off-axis and the depth-dependent terms respectively, and the summation is over the three different category of particles ($i = 1, 2, 3$) that are contributing to the total dose absorbed in the medium. We briefly discuss here how each particle category contributes to the total absorbed dose:

3.2.1 Primary protons (pp)

These are protons originally incident on the medium and before they undergo nuclear interactions. Primary protons lose their energy only through Coulomb interactions,

in which a fraction of their energy is given to atomic electrons of the medium, leading to ionization (see Fig. 2.1) while part of it goes into atomic excitation and or dissociation [64] [21]. Due to the small electron to proton mass ratio, the energy transferred to each atomic electron at each interaction is generally quite small. Literature shows that the maximum energy transferred to knock-on electrons ($\delta-rays$) never exceed 500 eV for 200 MeV protons [44] [43]. Overall, all of the energy the proton loses in each electronic collision can be assumed to be deposited locally (at the site of interaction), hence contributing to the kernel component $\mathfrak{D}_{pp}$ [15]. The loss of primary protons due to inelastic nuclear interactions causes reduction in primary proton fluence, and is also taken into account by $\mathfrak{D}_{pp}$.

3.2.2 Secondary protons (sp)

Energy lost through inelastic nuclear interactions is transferred to uncharged particles (neutrons and photons), secondary protons, and charged particles heavier than protons, such as deuterons, tritons, ^{3}He, alpha particles and recoil nuclei [59] [56] [58] [65]. Secondary protons contribute $\approx 10\%$ of the total dose proximal to the Bragg peak of the unmodulated proton beam [58]. Occasionally, secondary particles undergo inelastic nuclear interactions, some of them yielding tertiary protons and several other tertiary particles. All protons produced in an inelastic nuclear interaction are referred to as 'secondary protons' (Sec. 2.3), hence contribute to the dose component $\mathfrak{D}_{sp}$ through the Coulomb interactions (as described above for primary protons). Secondary protons, p′, produced in elastic collisions such as $^{1}\mathrm{H}(\mathrm{p},\mathrm{p}')^{1}\mathrm{H}'$ contribute to $\mathfrak{D}_{sp}$ through Coulomb interactions, while the recoil proton $^{1}\mathrm{H}'$ (the recoil hydrogen nucleus) contribute to $\mathfrak{D}_{rc}$.

3.2.3 Secondary neutrons and photons

Except through the emission of secondary protons in (n, pn) reactions, secondary neutrons do not significantly contribute to the dose distribution as they interact further away from the point where they are emitted [59]. They are however, mainly responsible for the long tail beyond the distal edge of the Bragg peak [63]. This tail is insignificant relative to the Bragg peak. In the (n, pn) reactions, the dose that is deposited by p is assigned to $\mathfrak{D}_{sp}$, and that deposited by n to $\mathfrak{D}_{rc}$. On the other hand, emission of secondary photons from inelastic nuclear interactions are negligible [15] [58]. In the current work the energy deposited by these photons was allocated to $\mathfrak{D}_{rc}$.

3.2.4 Recoil and other secondary charged particles (rc)

The recoil and secondary charged particles heavier than protons (e.g., deuterons, tritons, α-particles, ^{3}He) are assumed to deposit most of their energy locally, hence their dose contribution to the total kernel $\mathfrak{D}$ is through $\mathfrak{D}_{rc}$ [59]. Paganetti [58] shows that the energy deposited by these particles contribute less than 0.1% to the total dose.

Let us now define $\rho g_i(z)dz$ as the average energy $\bar{E}_i$ deposited at depths between z and $z+dz$ by primary protons (pp, $i=1$), secondary protons (sp, $i=2$), and recoil ions and secondaries other than protons (rc, $i=3$), where ρ is the density of the medium. Also, let $2\pi f_i(r,z)rdr$ denote fractions of the energy $\rho g_i(z)dz$ imparted to the medium by each particle category at radial distances between r and $r+dr$ off the z-axis. The depth dependent components (also known as depth dose distributions) $g_i(z)$ are given in units of MeV cm^2/g (per source proton), while the off-axis components or radial dose distributions $f_i(r,z)$ are given in units of cm^{-2} [63]. We can also write

$$g(z) = \sum_{i=1}^{3} g_i(z) \tag{3.2.4}$$

as the total *energy-deposition distribution*, so that

$$\bar{E} = \rho g(z)dz = \sum_{i=1}^{3} \bar{E}_i \tag{3.2.5}$$

is the average energy, per source proton, deposited in the medium at depths between z and $z+dz$ by all the radiation particles in the field [63] [66]. The radial distribution $f_i(r,z)$ is defined by

$$f_i(r,z) = \mathfrak{D}_i(r,z)/g_i(z), \tag{3.2.6}$$

with

$$\rho \int_0^\infty g(z)dz = E_0, \tag{3.2.7}$$

$$\left.\begin{aligned} 2\pi \int_0^\infty f(r,z)rdr = 1 \quad \forall z > 0, \\ 2\pi \int_0^\infty f_i(r,z)rdr = 1 \quad \forall z > 0 \end{aligned}\right\}, \tag{3.2.8}$$

where E_0 is the initial energy of the monoenergetic primary protons and $i = 1, 2, 3$ (the particle categories). It must be noted that the scattering is radially symmetric about the z-axis (or the direction of the pencil beam). Inserting $\mathfrak{D}_{pb}(r,z)$ into Eq. (B.3.10), it can be shown, with the help of Eq. (3.2.7), that $g(z)$ is equivalent to

the central-axis depth dose distribution of the broad parallel beam:

$$g(z) = \lim_{R\to\infty} \mathfrak{D}_{pp}(R; z). \tag{3.2.9}$$

It follows immediately that

$$g_i(z) = \lim_{R\to\infty} \mathfrak{D}^i_{pp}(R; z) \quad \forall i = 1, 2, 3. \tag{3.2.10}$$

Chapter 4

The analytical proton beamlet model

The proton beamlet model is an analytical dose calculation algorithm for proton pencil beams (beamlets) developed by Ulmer et al. [67]. It is based on the complete integration of the Bethe-Bloch equation which also provides the determination of R_{CSDA}, E(z) and dE(z)/dz using only those parameters given by the Bethe-Bloch equation itself (i.e., without further empirical parameterization). The results obtained from this integration were compared with Geant4 MC simulations. The Geant4 toolkit was also used to analyse lateral distributions, nonelastic nuclear interactions, the build-up effect, and to obtain or adjust some numerical parameters [32] [35].

4.1 The integration of the Bethe-Bloch equation

In this section we discuss, without too much detail, the integration of the Bethe-Bloch equation and the derivation of the beamlet model as given by Ulmer et al. in [67] [68] [35] [32] [57]. The integration of the Bethe-Bloch equation according to [67] leads to a power expansion of R_{CSDA} in terms of E_0:

$$R_{\mathrm{CSDA}} = \frac{1}{\rho} \cdot \frac{A_{\mathrm{N}}}{Z} \sum_{i=1}^{\mathrm{N}} \alpha_i E_I^{p_i} E_0^i \quad (\lim \mathrm{N} \to \infty). \tag{4.1.1}$$

To arrive at Eq. (4.1.1), the boundary conditions

$$\begin{aligned} z = 0 &\Rightarrow E = E_0, \\ z = R_{\mathrm{CSDA}} &\Rightarrow E = 0 \end{aligned} \tag{4.1.2}$$

were applied. The term E_I refers to an average ionization energy, Z/A_{N} to the nuclear charge/mass number of the absorbing material, and ρ to it's density (g/cm^3). The coefficients α_i in Eq. (4.1.1) are determined by the complete integration of the

α_1	α_2	α_3	α_4	p_1	p_2	p_3	p_4
6.8469×10^{-4}	2.26769×10^{-4}	-2.4610×10^{-7}	1.4275×10^{-10}	0.4002	0.1594	0.2326	0.3264

Table 4.1: *Parameter values for Eq. (4.1.1) if E_0 is in MeV, E_I in eV and R_{CSDA} in cm [68]*

Bethe-Bloch equation and are given in Table 4.1. For water, $Z = 10$, $A_N = 18$, $\rho = 1.0$ g/cm^3, and $E_I = 75.1$ eV, Eq. (4.1.1) becomes:

$$R_{CSDA} = \sum_{i=1}^{\mathrm{N}} a_i E_0^i \quad (\lim \mathrm{N} \to \infty). \tag{4.1.3}$$

The case of N=4 yields very accurate results for energies below 300 MeV [35]. The coefficients a_i in Eq. (4.1.3) are given in Table 4.2.

a_1	a_2	a_3	a_4
6.94656×10^{-3}	8.13116×10^{-4}	-1.21068×10^{-6}	1.053×10^{-9}

Table 4.2: *Parameter values for Eq. (4.1.3) if E_0 is in MeV, E_I in eV and R_{CSDA} in cm [68]*

Transforming Eq. (4.1.3) into a sum of exponential functions results in an inverted form which can be used for the calculation of the initial (input) energy from the residual range: $E(z) = E(R_{\mathrm{CSDA}} - z)$. A restriction to N=5 leads to highly accurate results for energies below 300 MeV.

$$\left.\begin{aligned} E_0 &= R_{\mathrm{CSDA}} \sum_{k=1}^{5} A_k e^{-R_{\mathrm{CSDA}}/\beta_k}, \\ E(z) &= (R_{\mathrm{CSDA}} - z) \sum_{k=1}^{5} A_k e^{-(R_{\mathrm{CSDA}} - z)/\beta_k} \end{aligned}\right\} \tag{4.1.4}$$

with parameter values given in the Table 4.3.

A_1	A_2	A_3	A_4	A_5	β_1	β_2	β_3	β_4	β_5
99.639	25.055	8.8075	4.19001	9.1832	0.0975	1.24999	5.7001	10.6501	106.727

Table 4.3: *Parameter values for Eq. (4.1.4) with $N = 5$, E_0 is in MeV, E_I in eV and R_{CSDA} in cm, A_k in MeV/cm and β_k is in cm [68]*

At this stage, the stopping power S(z) can be derived from E(z):

$$\mathrm{S}(z) = -\frac{dE(z)}{dz} = \sum_{k=1}^{5} A_k \left[1 - \beta_k^{-1}(R_{\mathrm{CSDA}} - z)\right] e^{-(R_{\mathrm{CSDA}} - z)/\beta_k}, \tag{4.1.5}$$

which is a sum of 5 exponential functions. In order to speed up the dose calculations, the 5 exponential functions in Eq. (4.1.5) were replaced by simpler functions, leading to

$$\mathrm{S}_{\mathrm{approx}} = \sum_{k=1}^{5} \varphi_k(E_0, z), \tag{4.1.6}$$

with

$$\left.\begin{aligned}
\varphi_1 &= C_1(E_0)\exp(-(R_{\mathrm{CSDA}}-z)^2/\tau_0^2)\theta(R_{\mathrm{CSDA}}-z),\\
\varphi_2 &= 2C_2(E_0)\theta(R_{\mathrm{CSDA}}-z),\\
\varphi_3 &= 2C_3(E_0)\exp(-Q_p(E_0)(R_{\mathrm{CSDA}}-z))\theta(R_{\mathrm{CSDA}}-z),\\
\varphi_4 &= 2C_4(E_0)(z/R_{\mathrm{CSDA}})^2\theta(R_{\mathrm{CSDA}}-z),\\
\varphi_5 &= 2C_5(E_0)(1-z/R_{\mathrm{CSDA}})\theta(R_{\mathrm{CSDA}}-z)
\end{aligned}\right\}. \tag{4.1.7}$$

The term $\exp(-Q_p(R_{\mathrm{CSDA}}-z))$ (φ_3) provides the main contribution of the exponentially increasing part of the Bragg curves [35]. The Gaussian term (φ_1) containing a half-width $\tau_0 \approx 10^{-5}$ cm reflects the behaviour of the Bethe-Bloch equation in the environment of the CSDA-range, which would otherwise be singular. Thus, φ_1 is therefore used instead of the $\delta-$function (if $\lim \tau_0 \to 0$). However, in the presence of range straggling the problem of the singularity does not exist (as will be shown later). The functions φ_2, φ_4, and φ_5 result from the power expansion of Eq. (4.1.5) with respect to the initial plateau and slowly increasing $\mathrm{S}(z)$ up to the order of z^2/R_{CSDA}^2 [35]. A unit step function $\theta(R_{\mathrm{CSDA}}-z)$:

$$\theta(R_{\mathrm{CSDA}}-z) = \begin{cases} 1 & \text{if} \quad z \le R_{\mathrm{CSDA}},\\ 0 & \text{if} \quad \text{otherwise} \end{cases} \tag{4.1.8}$$

is used in order to express the condition that the energy E(z) is zero at $z > R_{\mathrm{CSDA}}$. The term Q_p is expressed as $Q_p = \pi P_E/z_{\max}$, where $z_{\max}$ is given below in Eq. (4.3). The parameter P_E and the coefficients C_i ($i = 1, ..., 5$) depend linearly on E_0 and are determined by the variation procedure:

$$\left.\begin{aligned}
\sum_{E_0=1}^{300}\int_0^{R_{\mathrm{CSDA}}} |\mathrm{S}(z)-\mathrm{S}_{\mathrm{approx}}(z)|^2 dz &= \text{Minimum},\\
\mathrm{S}(z) \approx \mathrm{S}_{\mathrm{approx}} &= \sum_{k=1}^{5}\varphi_k(z, E_0)
\end{aligned}\right\}. \tag{4.1.9}$$

The contribution of C_5 was found to be negligible and is omitted (i.e., $C_5 = 0$), the accelerated algorithm is therefore restricted to four coefficients C_i ($i = 1, ...4$) and a parameter P_E (related to φ_3) which are calculated by

$$\left.\begin{aligned}
C_i &= \alpha_{0,i} + \alpha_{1,i}E_0 \quad (i = 1, .., 4)\\
P_E &= \alpha_{0,5} + \alpha_{1,5}E_0
\end{aligned}\right\}. \tag{4.1.10}$$

According to Ulmer et al. reproducing the parameter values in Table 4.4 by carrying

C_i	C_1	C_2	C_3	C_4	P_E
$\alpha_{0,i}$	2.277463	0.2431	1.0295	0.4053	6.26751
$\alpha_{1,i}$	-0.0018473	0.0007	-0.00103	-0.0007	0.00103

Table 4.4: *Parameters used to calculate the energy dependence of C_i and P_E according to Eq. (4.1.10) [68]*

out a least-squares fit against Geant4 results for different initial energies (E_0) led to the mean standard deviations of the order $0.04\% - 0.06\%$ [32].

4.2 Fluence decrease of primary protons

By performing an integration of the total nuclear proton-oxygen cross-section Ulmer et al. [57] derived the equation for the fluence decrease of primary protons Φ_{pp} due to nuclear interactions of protons in water as

$$\left.\begin{aligned} \Phi_{pp}(z) &= \frac{1}{2}\left(1 - uq\frac{z}{R_{\mathrm{CSDA}}}\right)\left[1 + \mathrm{erf}\left(\frac{R_{\mathrm{CSDA}} - z}{\tau}\right)\right]\Phi_0, \\ uq &= [(E_0 - E_{Th})/M_p c^2]^{1.032} \end{aligned}\right\}, \tag{4.2.1}$$

where Φ_0 is the arbitrary initial fluence of a proton beamlet at the surface, E_0 is the initial proton energy, $E_{Th} = 7$ MeV is the threshold energy for inelastic nuclear interactions (i.e., necessary to overcome the Coulomb repulsion of the oxygen nucleus), $M_p c^2 = 938.276$ MeV is the proton rest energy, and erf is the error function. Good agreement of the fluence decrease was found with the data of Chadwick et al. [69]. To account for energy/range straggling, Ulmer et al. first assumed that the energy/range straggling can be described by a Gaussian type of fluctuation. Therefore, the widths of the corresponding distributions can be added quadratically:

$$\tau = \sqrt{\tau_{\mathrm{strg}}^2 + \tau_{\mathrm{in}}^2}, \tag{4.2.2}$$

where τ_{in} represents the distribution of the incident beam and τ_{strg} the variation of the range due to straggling along the beam path [35]. The term τ_{strg} reaches its maximum at R_{CSDA}:

$$\tau_{\mathrm{strg}}(R_{\mathrm{CSDA}}) = \sqrt{2} \times 0.012703276 \times \begin{cases} R_{\mathrm{CSDA}}^{0.9352}, & \text{if} \quad R_{\mathrm{CSDA}} \geq 1\mathrm{cm} \\ R_{\mathrm{CSDA}}^{1.763}, & \text{if} \quad R_{\mathrm{CSDA}} \leq 1\mathrm{cm} \end{cases}. \tag{4.2.3}$$

For incident proton energies lower than 100 MeV, the energy-transfer distribution can be accurately defined by the symmetrical Gaussian, hence for a monoenergetic

proton beam (i.e., $\tau_{\text{in}} = 0$), a constant value of τ_{strg} can be used along the whole path of the beam. However, for incident energies greater than 100 MeV, Landau tails: asymmetrical fluctuations in the energy transfer, become more important, hence the depth dependence of τ_{strg} must be used. High energy protons undergo fewer hits, but deliver high energy to environmental electrons per hit, leading to asymmetrical energy transfer in the plateau region [35]. The consequence of this is the build-up effect which is observed in the plateau region for high energy ($\gtrsim$200 MeV) incident proton beams. As the kinetic energy of the incident particle decreases with increasing depth in the medium, the build-up effect also decreases. This is observed because the fluctuations in energy transfer tend to become symmetrical as the residual energy continue to decrease towards 100 MeV. Ulmer et al. suggests using the modified Gaussian convolutions, i.e., the Gaussian convolution kernel with additional relativistic correction terms expressed by the first and second (for $E_0 \lesssim$300 MeV) order terms in a series expansion of Hermite polynomials [35].

4.3 The dose distributions of primary protons

In the April 2007 Proton Algorithm Reference Guide [70] however, the inclusion of energy/range straggling, for quasi-monoenergetic narrow proton beams (beamlets) in the clinical energy range (0-250 MeV), was done by using a Gaussian[1] convolution kernel of the form

$$\left.\begin{aligned} I(z) &= \int I_{\text{mono}}(u) \times G_{\text{strg}}(u-z)du, \\ G_{\text{strg}}(u-z) &= \frac{1}{\sqrt{\pi}\tau} \exp\left(-\frac{(u-z)^2}{\tau_{\text{strg}}^2} \right) \end{aligned}\right\}. \tag{4.3.1}$$

The term τ is as given by Eq. (4.2.2), except the restriction, $\tau_{\text{in}} = 0$, to monoenergetic beamlets has been applied here. The overall depth dose distribution for primary protons, including the effect of energy/range straggling, is a combination of the fluence decrease of primary protons and the integration of the Bethe-Bloch equation:

$$\begin{aligned} \text{S}_{pp}(E_0, \tau_{\text{strg}}, z) = \Phi_0 \left[1 - uq\left(\frac{z}{R_{\text{CSDA}}} \right) \right] [I_1(E_0, \tau_{\text{strg}}, z) + I_2(E_0, \tau_{\text{strg}}, z) + I_3(E_0, \tau_{\text{strg}}, z) \\ + I_4(E_0, \tau_{\text{strg}}, z) + I_5(E_0, \tau_{\text{strg}}, z)] \end{aligned}, \tag{4.3.2}$$

where Φ_0 (dimensionless) can be put equal to 1, the factor $(1 - uq \times z/R_{\text{CSDA}})$ represents the number of remaining protons at a given depth, and the I_i-terms

[1] The Gaussian usually has the exponential of the form $-r^2/(2\sigma^2)$, but for computational reasons, $\sqrt{2}\sigma$ is substituted for τ in Eq. (4.3.1) [70]

$(i = 1, .., 5)$ result from functions of Eq. (4.1.7) subject to a Gaussian convolution with τ according to Eq. (4.3.1) to account for energy/range straggling. They are given as

$$\left.\begin{aligned}
I_1 &= \left(C_1 - \frac{C_{\text{lin}} \times \tau_{\text{strg}}}{\sqrt{\pi} R_{\text{CSDA}}} - \frac{C_4 \times \tau_{\text{strg}} \times (R_{\text{CSDA}} + z)}{\sqrt{\pi} R_{\text{CSDA}}^2}\right) \times \exp\left(-\frac{(R_{\text{CSDA}} - z)^2}{\tau_{\text{strg}}^2}\right), \\
I_2 &= \left(C_2 + \frac{C_4 \times \tau_{\text{strg}}^2}{2 \times \sqrt{\pi} R_{\text{CSDA}}^2}\right) \times \left[1 + \text{erf}\left(\frac{R_{\text{CSDA}} - z}{\tau_{\text{strg}}}\right)\right], \\
I_3 &= C_3 \exp\left(-P_E \times \pi \times \frac{R_{\text{CSDA}} - z}{z_{\text{max}}}\right) \times \left[\text{erf}\left(\frac{R_{\text{CSDA}} - z}{\tau_{\text{strg}}} - \frac{1}{2} \times P_E \times \pi \times \frac{\tau_{\text{strg}}}{z_{\text{max}}}\right) + 1\right], \\
I_4 &= C_4 \times \frac{z^2}{R_{\text{CSDA}}^2} \times \left[1 + \text{erf}\left(\frac{R_{\text{CSDA}} - z}{\tau_{\text{strg}}}\right)\right], \\
I_5 &= \left[-C_{\text{lin}} \times \left(1 - \frac{z}{R_{\text{CSDA}}}\right)\right] \times \left[1 + \text{erf}\left(\frac{R_{\text{CSDA}} - z}{\tau_{\text{strg}}}\right)\right]
\end{aligned}\right\}. \tag{4.3.3}$$

The parameters C_i $(i = 1, .., 4)$, P_E (calculated using Eq. (4.1.10) and Table 4.4), $C_{\text{lin}} \approx 0.02$, which describes the Landau tail and was (when deriving these functions) fixed to fit an energy of about 150 MeV, z_{max}, and τ_{strg} were determined theoretically, checked by MC (Geant4) simulations (i.e., yield deviations of 2-4%) and then adjusted to agree with MC results [70].

It must be mentioned here that these dose distribution formulae are taken from the April 2007 "Proton Algorithm Reference Guide-Eclipse$^{\text{TM}}$" edition of the Varian medical systems. The more recent version may have implemented the improvements that Ulmer et al. has made to this model in the papers, e.g., improved treatment of the Landau tails, the inclusion of nonelastic nuclear interactions [57], etc. Unfortunately we did not have a more recent copy of the manual at the time of this work. The term z_{max} in Eq. (4.3.3) is given by

$$z_{\text{max}} = R_{\text{CSDA}} + \tau_{\text{Range}}, \tag{4.3.4}$$

where

$$\tau_{\text{Range}} = R_{\text{CSDA}}\left(2.1179 \times 10^{-5} E_0 + 0.919 \times 10^{-7} E_0^2\right). \tag{4.3.5}$$

The lateral scattering is modelled by the sum of two Gaussian: (1) the Gaussian approximation for the small-angle MSC, and (2) a wide tail to account for the large-angle scattering events. The scatter kernel is given by

$$k_{l,p}(r, z) = C_0\left(\frac{1}{\pi \tau_0^2}\right) \times \exp\left(-\frac{r^2}{\tau_0^2}\right) + (1 - C_0) \times \frac{1}{\pi \tau_1^2} \times \exp\left(-\frac{r^2}{\tau_1^2}\right), \tag{4.3.6}$$

where $C_0 = 0.96$. The scatter kernel $k_{l,p}(r, z)$ describes the scattered intensity at a radius r from the central axis of the beamlet, at a depth z [70]. The scatter

parameters τ_0 and τ_1 of the scatter kernel $k_{l,p}$ are functions of depth z, they represent the root mean square (RMS) or the half-width of the beamlet. They are given by

$$\tau_0 = \begin{cases} \tau_{\max} \times (0.205s + 0.795s^2) & \text{for} \quad z < R_{\text{CSDA}}, \\ \tau_{\max} & \text{for} \quad z \geq R_{\text{CSDA}} \end{cases}, \tag{4.3.7}$$

and

$$\tau_1 = 0.90563\left(\frac{1}{176.58}\right)^p \exp\left(-\frac{(s-1)^2}{0.252}\right), \tag{4.3.8}$$

where

$$p = \begin{cases} 1.5 + 0.0015 \times (176.576 - E_0) & \text{if} \quad E_0 \leq 176.5876, \\ 1.5 + 0.03104 \times \sqrt{E_0 - 176.576} & \text{if} \quad E_0 > 176.576 \end{cases}, \tag{4.3.9}$$

$$\tau_{\max} = 0.626 \times \left(\frac{E_0}{176.576}\right)^p, \tag{4.3.10}$$

$$\tau_0 = \begin{cases} f \times \tau_{\max} \times \frac{(e^{-Q(1-s)} - e^{-Q})}{(1-e^{-Q})} & \text{if} \quad s \leq 1, \\ f \times \tau_{\max} & \text{if} \quad s > 1 \end{cases}, \tag{4.3.11}$$

$s = z/R_{\text{CSDA}}$, $Q = 2.887$, and $f = 0.9236$. All the constants were determined by fitting the above formulas to MC simulation results [70].

4.4 The dose distributions of secondary protons

The generation and transport of secondary protons and recoil particles is another topic that was thoroughly investigated leading to the development of the beamlet analytical model. In [35], [32], and [57], Ulmer et al. defines secondary protons as those protons that undergo nuclear interactions with the nucleus (see Eq. 2.3.1). They further separate them (secondary protons) into nonreaction protons (sp_n) and reaction protons (sp_r). Nonreaction secondary protons result from elastic scattering due to strong interaction potential in the environment of the nucleus and the resonant inelastic scattering due the proton/nucleus interaction, thereby inducing transitions between different states of the nucleus. On the other hand reaction secondary protons emanate from inelastic nuclear scattering due to high energy incident protons, yielding heavy recoil fragments and recoil protons. The dose distribution of the nonreaction secondary protons is modelled in a similar manner as the primary protons. The contribution of the reaction protons is largely based on MC simulations because of its dependency on the fluence reduction of primary protons and the generation of heavy recoils [35]. Fig. 4.1 shows the depth dose curve of secondary reaction protons (sp_r) for given therapeutic proton energies in water.

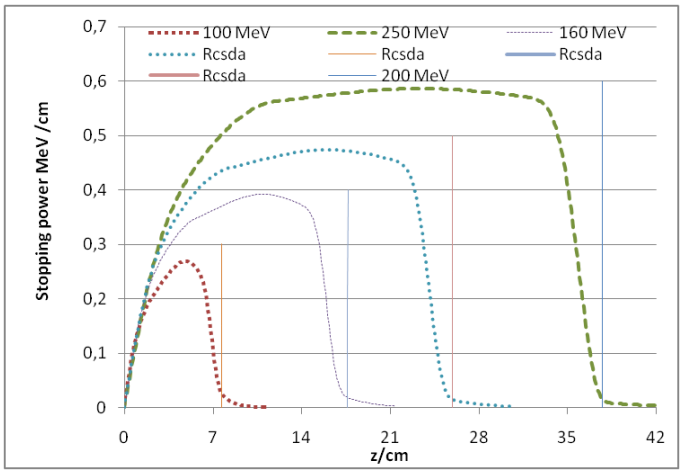

Figure 4.1: *The dose distribution (generalized stopping power that incorporates the particle fluence) of the secondary/tertiary reaction protons for the initial proton energies 100 MeV, 160 MeV, 200 MeV, and 250 MeV in water. The R_{CSDA} ranges are indicated by the perpendicular straight lines [35].*

The fluence of secondary protons Φ_{sp} ($\Phi_{\mathrm{sp,n}}$ and $\Phi_{\mathrm{sp,r}}$) and recoil protons (Φ_{rp}) put together is approximately equal to the fluence decrease of primary protons due to nuclear interactions [35]. Ulmer et al. gave the fluence of secondary nonreaction (sp,n) and recoil protons as

$$\left.\begin{aligned}\Phi_{\mathrm{sp,n}} &= \upsilon(1-2C_{\mathrm{heavy}})\left(\Phi_0\frac{uq\cdot z}{R_{\mathrm{CSDA}}}\right)\\ \Phi_{\mathrm{rp}} &= 0.042\left(\Phi_0\frac{uq\cdot z}{R_{\mathrm{CSDA}}}\right)\end{aligned}\right\}, \tag{4.4.1}$$

where

$$C_{\mathrm{heavy}} = \begin{cases} 3.46\times10^{-3}+7.81\times10^{-5}E_0 & \text{if} \quad E_0 \geq 7 \quad \text{MeV},\\ 0 & \text{else}\end{cases}. \tag{4.4.2}$$

The parameter υ represents the fraction of secondary protons reaching the water phantom. It can therefore vary depending on the beam line characteristics. Generally, the assumption is made that some percentage of secondary protons are lost along the beam line as they scatter broader than the primary protons, in which case υ can be set to 1 for scanning beam lines. Alternatively, Ulmer et al. suggests using a specific Monte Carlo code to simulate the beam line characteristics and to determine the associated phase space [35]. However, in the current work, the value 0.958 given in the April 2007 Proton Algorithm Reference Guide was used.

Overall, modelling the dose contribution of secondary non-reaction protons and recoil protons was largely guided by MC simulations. It was realized that they basically show the same physical behaviour as the primary protons Eq. (4.3.3) [35], except

their Bragg peak is much broader and shifted to a lower z-value. The depth dose distribution for secondary protons is given by

$$\begin{aligned} \mathrm{S}_{sp}(E_0, \tau_{\mathrm{strg,sp}}, z_s) = \beta \times uq \times \left(\frac{z}{R_{CSDA}}\right) \Big[& I_1(E_0, \tau_{\mathrm{strg,sp}}, z_s) + I_2(E_0, \tau_{\mathrm{strg,sp}}, z_s) \\ & + I_3(E_0, \tau_{\mathrm{strg,sp}}, z_s) + I_4(E_0, \tau_{\mathrm{strg,sp}}, z_s) + I_5(E_0, \tau_{\mathrm{strg,sp}}, z_s) \Big] \end{aligned}, \tag{4.4.3}$$

where

$$z_s = z + z_{\mathrm{shift}}\,, \tag{4.4.4}$$

$$\left.\begin{aligned} \tau_{\mathrm{strg,sp}} &= \sqrt{\tau_{\mathrm{strg}}^2 + \tau_{\mathrm{heavy}}^2}, \\ \tau_{\mathrm{heavy}} &= 0.5541 - 5.85 \times 10^{-4} \times (E_0 - E_{\mathrm{pmax}}) \end{aligned}\right\}, \tag{4.4.5}$$

$$z_{\mathrm{shift}} = 0.255 \begin{cases} \exp\left(-2\pi^2 \frac{(E_{\mathrm{pmax}} - E_0)^2}{E_{\mathrm{pmax}}} \right) & (\text{if} \quad E_0 \le E_{\mathrm{pmax}}), \\ \exp\left(\frac{-(E_{\mathrm{pmax}} - E_0)^2}{E_{\mathrm{sig}}} \right) & (\text{if} \quad E_0 > E_{\mathrm{pmax}}) \end{cases}, \tag{4.4.6}$$

$\beta = \upsilon(1 - 2C_{\mathrm{heavy}}) \approx 0.958$, $E_{\mathrm{Th}} = 7.0$ (MeV), $E_{\mathrm{pmax}} = 20.12$ (MeV), and $E_{\mathrm{sig}} = 106.875$ (MeV) [70]. Note that the I-terms of Eq. (4.3.3) are used here too only with z and τ_{strg} replaced by z_s and $\tau_{\mathrm{strg,sp}}$ respectively.

The lateral scattering for the secondary protons is described by a single Gaussian, which is less accurate but acceptable since their dose contribution does not exceed 20% (for $E_0 = 250$ MeV). However, the depth dependent scatter parameter τ_2 is different from that of primary protons because secondary protons already have an initial angular spread (due to nuclear interactions) as they begin to be transported in the medium [70]. The lateral scatter kernel for secondary protons is therefore given by

$$k_{l,sp}(r, z) = \frac{1}{\pi \tau_2^2} \exp\left(-\frac{r^2}{\tau_2^2} \right), \tag{4.4.7}$$

where

$$\tau_2 = \sqrt{\tau_{2.0}^2 + \tau_{\mathrm{heavy}}^2}, \tag{4.4.8}$$

and

$$\tau_{2.0} = \begin{cases} \tau_{\mathrm{max}} \left(\frac{e^{-Q(1-s)} - e^{-Q}}{(1 - e^{-Q})/0.626} \right) & (\text{if} \quad s \le 1), \\ \frac{\tau_{\mathrm{max}}}{0.626} & (\text{if} \quad s > 1) \end{cases}. \tag{4.4.9}$$

The quantities Q, s, τ_{heavy}, and τ_{max} are as given earlier.

4.5 The dose distributions of heavy recoil particles

According to [70] [35] [67], nuclear fragments resulting from inelastic scattering of the primary and secondary protons as well as protons that lose most of their energy in nuclear collisions such that they subsequently emerge as slow protons are regarded as recoil particles (heavy recoils and recoil protons) which deposit their energy locally (i.e., at the point where they suffer interactions) [70]. In the Proton Algorithm Reference Guide-Eclipse of the Varian medical systems, recoil energy loss is modelled using similar equations (Eq. 4.3.3) as the primary protons except z is replaced by z_s.

$$\mathrm{S}_{rc}(E_0, \tau_{\mathrm{strg}}, z_s) = 0.042 \times uq \times \left(\frac{z}{R_{\mathrm{CSDA}}}\right)\Big[I_1(E_0, \tau_{\mathrm{strg}}, z_s) + I_2(E_0, \tau_{\mathrm{strg}}, z_s) + I_3(E_0, \tau_{\mathrm{strg}}, z_s) + I_4(E_0, \tau_{\mathrm{strg}}, z_s) + I_5(E_0, \tau_{\mathrm{strg}}, z_s)\Big] \quad (4.5.1)$$

The lateral dose distribution for recoil particles is taken to be identical to that of primary protons. This assumption was made based on the fact that recoil particles are mainly produced by the primary protons and mainly deposit their energy locally [70].

4.6 The total dose distribution

The total 3D dose distribution of the beamlet at any point in the homogeneous medium is the sum of energy loss by primary protons, secondary protons and recoil particles (heavy recoils and recoil protons):

$$D_{total}(r, z) = (\mathrm{S}_{pp}(z) + \mathrm{S}_{rc}(z)) \times k_{l,p}(r, z) + \mathrm{S}_{sp}(z) \times k_{l,sp}(r, z). \quad (4.6.1)$$

4.7 Implementation of the beamlet model

Comparisons of the dose profiles of the two methods were done using Mathematica (version 10.2) [71]. The analytical beamlet functions were coded in Mathematica and integrated as described in Appendix D. The results were further analysed, the normalization factors and other parameters calculated (e.g., FWHM, R_{80} shift, entrance-to-peak dose ratio), and ultimately the dose distribution curves (in Sec. 6.2) were generated.

Chapter 5

Geant4 simulations

This chapter gives detailed description of the simulation of the transport of protons in the clinical energy range through a homogeneous phantom of water, undertaken using the Geant4 (version 10.1) MC toolkit. The geometry, medium material, choice of physics models and processes, and control parameters (step size, range cuts, etc.), particle tracking and tallying of dose deposited as a result of the interaction of particles with the target medium (water) will be discussed here.

5.1 Detector geometry and material

The simulation geometry comprises of a $50 \times 50 \times 50$ cm^3 cube[1] built using a concrete class `G4DetectorConstruction` of Geant4's `G4VuserDetectorConstruction` base class. The cube is filled uniformly with the medium material which in our case is liquid water, defined using the internal Geant4 material database through the `G4Material` class. By deriving a concrete detector class from the abstract base class `G4VSensitiveDetector`, and assigning it to the logical volume (`G4LogicalVolume` objects) of the cube geometry in the `G4VUserDetectorConstruction::Construct-SDandField()` method, the whole cube is made sensitive (i.e. 'readout' detector). The `ProcessHits()` method constructs hits (snapshots of the physical interaction of tracks in the sensitive region of a detector) using information from steps along the particle track (`G4Step` objects) as input, or in the case of 'readout' geometry, objects of the `G4TouchableHistory` class are used as optional input [39].

A concrete class derived from `G4VuserPrimaryGeneratorAction` is used to place the source of primary protons on the inner wall of the the phantom at $(0, 0, 0)$, with the proton beam directed into the phantom of water, z$>$ 0, along the z-axis

[1] A plane geometry was opted for over a voxelized one due to slower simulation speed with the latter. Besides, dose tallying was done outside of the Geant4 program.

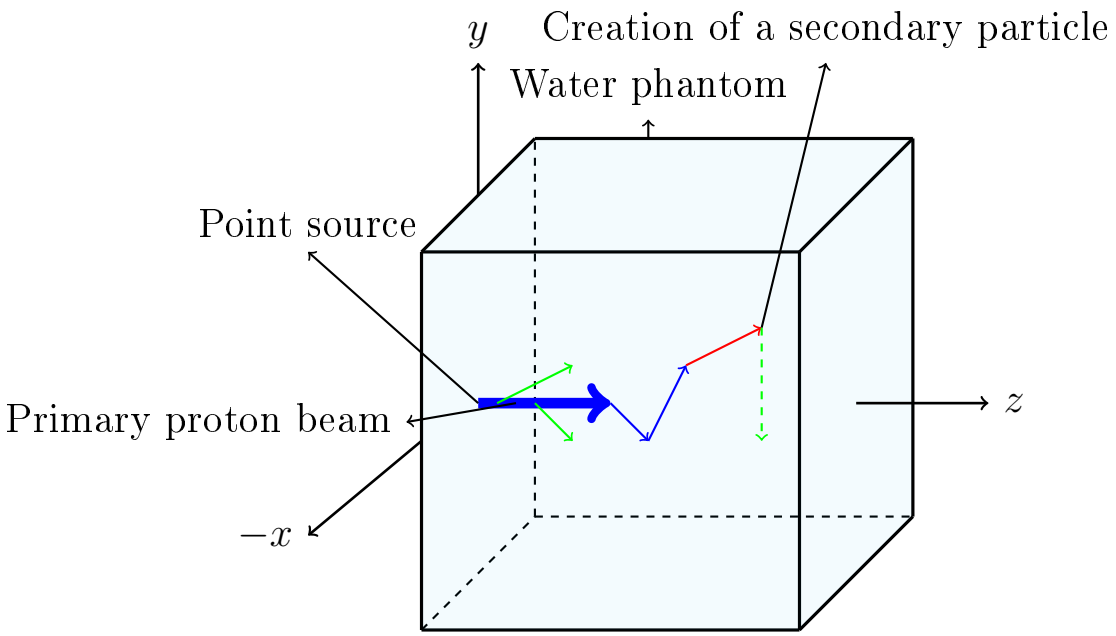

Figure 5.1: *A beam of source protons (blue) is directed into the phantom of water. Arrows (associated with their length) represent steps of particle tracks. The colour (Geant4 simulations) codes: blue is used for proton tracks (or +1 charged particles), green for gammas (or neutral particles), and red electrons (or -1 charged particles).*

(Fig. 5.1), while the actual generation of primary protons is done by the concrete class `G4ParticleGun` (one of the three concrete classes of `G4VPrimaryGenerator` base class). The particle generator, `G4ParticleGun`, is used in its simplest form: no randomizing of any sort, generates particles with the same kinematics, hence the source beam is assumed to be mono-energetic and mono-directional, apart from being a point source.

At the core of the Geant4 kernel (central unit) is the `G4RunManager` (or `G4MTRunManager` if the simulation code is multi-threaded) class responsible for controlling the flow of the program and managing event loops within a run. It also manages initialization procedures, including methods in the initialization classes. As such, the user must, through the initialization classes, provide the run manager with all the information necessary to build and run the simulation, for example, how the detector should be constructed, all the particles and physics processes to be simulated, how the primary particles in an event should be generated, etc. [39]. Because it plays such a central role, the run manager is the only manager class that must be explicitly constructed within the central part of the program that links all classes and subprograms, commonly referred to as the `main()` program. Other manager classes are created and destroyed when the run manager class is created and destroyed, respectively.

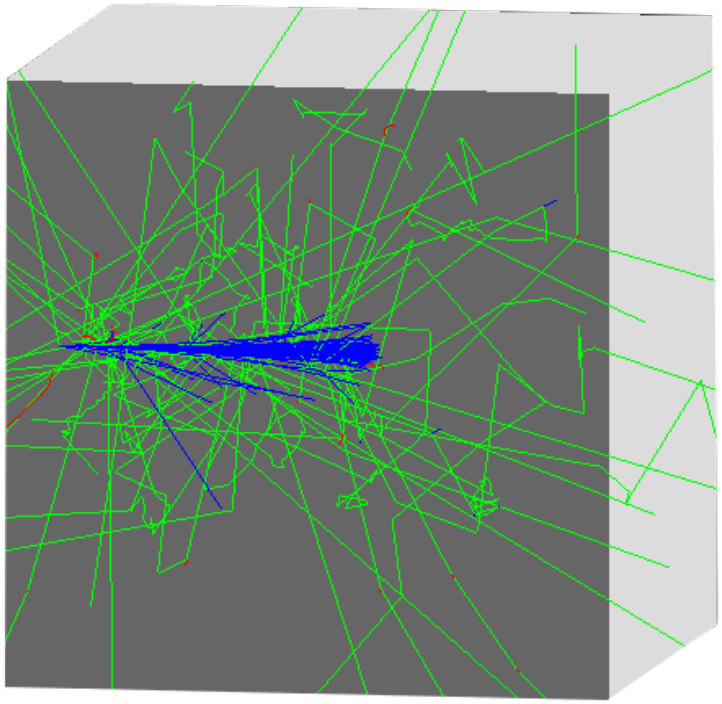

Figure 5.2: *Incident protons (blue) from a point source located at the origin and initially along the positive z-axis scatter laterally and generate secondary particles (e.g., electrons (red), gammas or neutrons (green), etc.) as they interact with water.*

5.2 Physics lists

Given the complexity of Geant4, a single modelling algorithm cannot accurately describe all possible interaction processes for the entire energy domain and for all particles. For instance, some models are valid only over finite energy ranges, and there may be competing models in a given energy range. Besides, some models may perform better with a specific group of particles, while others may do better with other species. The need to use a combination of physics processes (models and cross sections) is therefore inevitable if a comprehensive simulation is to be achieved. Geant4 provides a wide variety of physics components for simulating particle interaction with matter. These are coded as processes (a process is a class that describes how a particle interacts with a given medium), and are classified into electromagnetic, hadronic, decay, parameterized, or transport [72] [41]. To put the programs describing these processes together in a way that they can be invoked flexibly at given stages of the simulation, Geant4 uses the concept of *physics lists*. A physics list is a collection of physics processes (cross sections and models), particles, secondary particle production thresholds and step sizes required to, successfully and accurately, carry out a particular set of simulations [73]. It is therefore the responsibility of the user to define all the particles and processes they would like to simulate.

This is done through the mandatory user class `G4VUserPhysicsList`. The user derives a concrete class and invokes the `ConstructParticle()`, `ConstructProcess()`, and `SetCuts()` methods of this class (`G4VUserPhysicsList`).

5.2.1 Physics models in Geant4

Generally, a physics list for proton interaction with matter (e.g., water) would consist of at least three modules (sets of physics models and processes) that account for the following types of interactions: (a) electromagnetic, (b) elastic scattering, and (c) inelastic scattering of protons, neutrons, and heavier ions. Physics models are usually a mixture of theory-driven, parameterized, and, for cases where sufficient experimental data are available (e.g., inelastic nuclear interaction cross section), data-driven formulae [37]. Detailed discussions of various models for proton therapy simulations, their build structure, and their successes or limitations are given in [48] [62] [47] [40], and many other Geant4 hadron therapy related studies [74] [72] [58]. Variations do arise in the choice of models and control parameters (e.g., step size, range cuts) depending on the use-case or results the user is trying to achieve. The level of fine-tuning, hence the accuracy of the generated results may also differ among such studies as it depends mainly on available computational power [75].

In order to optimize our Geant4 simulations, that is, to obtain as accurate dose distributions as possible while allowing the simulations to be relatively fast, given the limited computational power at our disposal (i.e., Intel^{R} Core^{TM} i7-4710HQ CPU (8) @ 2.50GHz, DDR3L 1600 MHz SDRAM, 16 GB), a thorough review of previous studies on the choice of models and control parameter values used in Geant4 proton therapy simulations was done. The influence of a few physics models on the dose distributions were compared (Fig. 6.1) and used to come up with optimized physics models and a parameter list (see Table 5.3). Specifically, the standard electromagnetic model, `EmStandard_Opt3`, which is highly recommended for medical proton therapy simulations by [76] and others, was adopted. The simulation of the nonelastic nuclear interactions is done using the binary cascade model, together with its back-end pre-equilibrium (`G4PreCompoundModel`) and equilibrium models (see Sec. 2.3.1), while for MSC Geant4 uses the Urbàn MSC model [50]: (`G4UrbanMscModel`), which is not only computationally competitive but also relatively accurate. The Urbàn model is based on the Lewis model of MSC [31] (see Sec. 2.2.1).

It turns out that some 'reference physics lists' (released within Geant4 toolkit) implement combinations of physics components or models appropriate for the simulation of clinical energy range (e.g., 50-250 MeV) protons in water, while others may require

only minor modifications to meet specific user requirements. One such example is the `QGSP_BIC_EMY` physics list [47]. In fact, the `QGSP_BIC_EMY` reference physics list is highly recommended for clinical proton therapy simulations, not only because it is built specially for this purpose by a group of individuals specializing on this component of Geant4 [74], but because it is also tested and validated regularly (improved in every new Geant4 release) [74] [47] [40] [41]. A summary of its building blocks is given in Table 5.1, while a breakdown of models activated for distinct phases are tabulated in Table 5.2. This physics list was therefore used in our simulations, following comparisons with models implemented in alternative reference physics lists (e.g., QGSP_BERT, QGSP_FTFP_BERT, FTFP_BERT (see Sec. 6.1)).

Hadron Process	Particle	Geant4 Process	Geant4 Models	Geant4 data sets	Energy range
Elastic scattering	Generic Ion	G4HadronElastic Process	G4LElastic	G4HadronElastic DataSet	- -
	All Other particles	G4UHandronElastic Process	G4HadronElastic	G4HadronElastic DataSet	- -
Inelastic Process for protons	Protons	G4ProtonInelastic Process	G4BinaryCascade	G4ProtonInelastic CrossSection	0-20 GeV
Inelastic process for Ions	Generic Ion	G4IonInelastic Process	G4BinaryLightIon Reaction	G4IonsShen CrossSection	0-20 GeV
	Deuteron, Triton, Alpha	G4IonInelastic Process	G4LEInelastic G4BinaryLightIon Reaction	G4TripathiLight CrossSection	0-80 MeV 80 MeV-20 GeV
Radiative capture	Neutron	G4HadronCapture Process	G4LCapture	G4HadronCapture DataSet	14 MeV-20 GeV
Inelastic Scattering for neutrons	Neutron	G4NeutronInelastic Process	G4BinaryCascade	G4NeutronInelastic CrossSection	14 MeV-20 MeV

Table 5.1: *Hadron physics models and processes implemented in the QGSP_BIC_EMY reference physics list (original table by [77]).*

5.3 Step size and range cut value

Another set of important input information that significantly affects dose distributions has to do with the so-called simulation control parameters (or simulation transport parameters), that is the *maximum step size*, defined as the distance to the next interaction, and the *range cut* value, defined as the production threshold

EM Physics	
	EmStandard_Opt3: Analytical model⇒treats photons & all charged particles down to 1 keV. Bethe-Bloch⇒Hadron energy loss $\geq$ 2 MeV. ICRU parameterized stopping power $<$ 2 MeV.
Multiple Scattering	
	G4UrbanMScModel: ⇒Calculates spatial & angular distribution of scattered particles.
Nuclear Interactions	
	G4BinaryCascadeModel⇒Intranuclear cascade models (phase). G4PreCompoundModel⇒Pre-equilibrium models (phase). G4VEvaporation, G4VFission, G4VFermiBreakUp, G4VMultiFragmentation, G4VPhotonEvaporation⇒Equilibrium models (phase).
Elastic Interactions	
	G4LElasticModel, G4HadronElasticModel, Cross-section modules: UHElastic + G4HadronElastic = G4UHadronElasticProcess.

Table 5.2: *Models implemented in the QGSP_BIC_EMY reference physics list.*

for secondary particles such as the electrons, positrons, gammas, and protons [47] [40]. These are crucial in MC simulations as they do not only influence the speed of the simulation but the accuracy of the results as well. Generally in Geant4, each process has intrinsic limits to produce secondary particles, all particles produced are tracked down to zero energy, and each particle has a suggested cut in range which is internally converted to energy for all material [39]. One therefore needs to find a balance between simulating all the physics processes they are interested in (i.e., at what energy to stop tracking a particle) and the CPU time, as some processes can lead to exponential increase in the simulation time at low energies. This requires setting a cut-off in energy, so that particles stop being tracked when they reach a specific threshold in energy, and the remaining energy can be assumed to be deposited locally. In Geant4, the production threshold for secondary particles (range cut value) is given via the `SetCUts()` method of the `G4UserPhysicsList` in the form of distance, which is internally converted to threshold energies for each particle in a given medium material [39] [47].

In trying to gain full control of secondary particle production, hence secondary particle energy loss in the medium (water), we had to implement 'special cuts' (using the `/run/SetCutForAGivenParticle` UI commands), that is allocate a unique range cut value of 1.0 mm ($\approx$ 350 keV) to electrons, positrons, and gammas, while protons were allocated a range cut of 0.001 mm ($\approx$ 0.080 MeV). In principle, this undertaking was meant to address two issues: (1) the unphysical case in which heavy recoils (rc group) produced higher dose profiles than secondary protons (sp group) when a single small (say, 0.001 mm) cut-off value was used for all particles, and (2) the

lack of convergence in the dose profiles. Ideally, convergence in the dose profiles is expected at lower cut-off values (i.e., < 1.0 mm). Appendix E briefly discusses how convergence was attained.

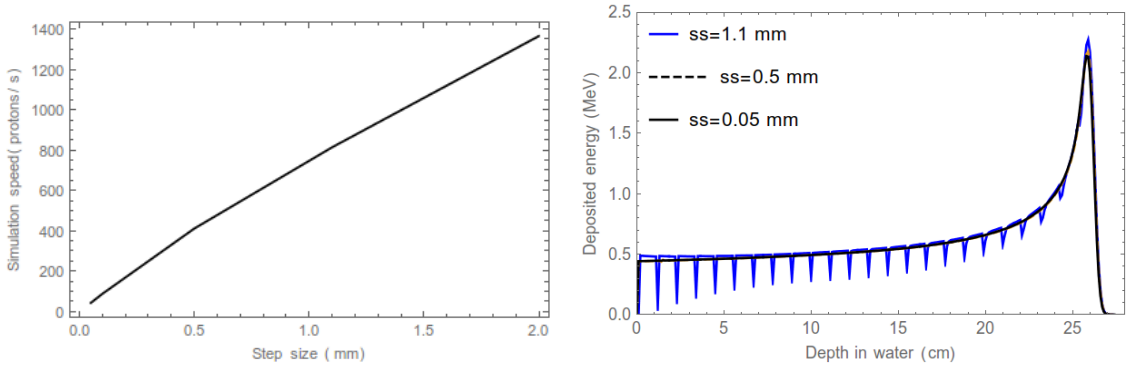

(a) *Simulation speed.* **(b)** *Effects of step size on dose distribution.*

Figure 5.3: *Simulation speed versus step size (a), and effects of step size on the dose distributions (b): at smaller step sizes, Bragg curves converge. Above 1.0 mm, artefacts manifest.*

Besides the other (discrete) processes, the continuous energy loss imposes a limit on the step size too, because of the dependence of the cross section of different processes on the energy of the particle. It is generally assumed in some MC programs (e.g., EGS, Geant3) that the cross sections are approximately constant along a step, i.e., the step size is so small that the change in energy, and hence in cross section, along the step is also small [47]. In principle, very small steps should be used to ensure accurate simulations, however the CPU time increases with decreasing step size (Fig. 5.3a). Alternatively, step limiting can be controlled by the *StepFunction* (Eq. (5.3.1)) or a user defined *maximum allowed step*. The *maximum allowed step* limits the step length according to the user-given value in competition with intrinsic limits of the process. The *StepFunction* is a dynamic step limiting function which decreases the particle step limit (ΔS_{lim}) in parallel with the particle's decreasing range.

$$\Delta S_{lim} = \alpha_R \cdot R + \rho_R(1 - \alpha_R)(2 - \frac{\rho_R}{R}), \tag{5.3.1}$$

where $\alpha_R \sim Step/Range$ (referred to as the 'dRoverRange') defines the maximum step size allowed (default $\alpha_R = 0.2$). As the particle travels the maximum step size decreases gradually until the range becomes lower than ρ_R (referred to as the 'finalRange', default $\rho_R = 1.0$ mm) [47]. The parameters of the *StepFunction* can be overwritten using the UI command: `/process/eLoss/StepFunction` 0.2 1.0 mm.

Physics List	Step size (mm)	$e^-/e^+/\gamma$ range cut (mm)	p range cut (mm)
QGSP_BIC_EMY	0.1	1.0	0.001

Table 5.3: *The table lists the simulation control parameters: step size and range cuts used in the Geant4 simulations.*

	e^-/e^+	Proton	Generic Ion
StepFunction-finalRange	0.1 mm	0.05 mm	0.02 mm

I (mean ionization potential of water)	Bins/decade
75.0 eV	20

Table 5.4: *The table lists the values for the stepping function final range, the I-value and the number of bins used in option 3 of the EmStandard physics component.*

The maximum allowed step size is related to the range cut and is primarily intended for limiting the step of the particle being tracked. In Geant4, step limiting is done artificially by assigning `G4UserLimits` to the intended volume[2] (see Fig. 5.3a) in addition to attaching the process `G4StepLimiter` to the intended particle's process manager. Limiting the step of a particle during tracking increases the frequency of dose deposition along the track, thereby limiting propagation of inaccurate data sampling to the maximum allowed step size [40]. As shown in Fig. 5.3b, larger step sizes cause discontinuities in the dose distribution. On the other hand, dose distributions converge at smaller step sizes.

5.3.1 Ionization potential and number of bins

It has been shown by Grevillot et al. [40] [42] that the proton range also depends on the mean ionization potential (I) of the medium (I was briefly discussed in Sec. 2.1). The I values of water and human tissue are of significant concern in proton therapy simulations as they are highly susceptible to error. For example, Grevillot et al. [40] found that the I values: 70.9 eV, 75.0 eV, and 80.0 eV moved the proton range to 324.9 mm, 329.2 mm, and 330.8 mm respectively, while the R_{CSDA} given by NIST is 329.4 mm. The I value recommended by ICRU reports 37 and 49 [44], 75.0 eV, was used in the present work.

[2] A step size less than or equal to half the smallest voxel is recommended.

As stated in Sec. 2.1.1, in order to speed up the simulation, Geant4 pre-calculates quantities related to the EM processes, i.e., the range and the inverse of the range, the mean free path (simply cross sections), and the stopping power dE/dz tables, according to the user-defined simulation parameters. The number of bins/decade in these pre-calculated EM tables need to be sufficiently high (>15 bins/decade) in order to accurately describe EM interactions [40]. For the present work, this issue was taken care of by the `Standard EM_Opt3` in which 20 bins/decade are implemented [47].

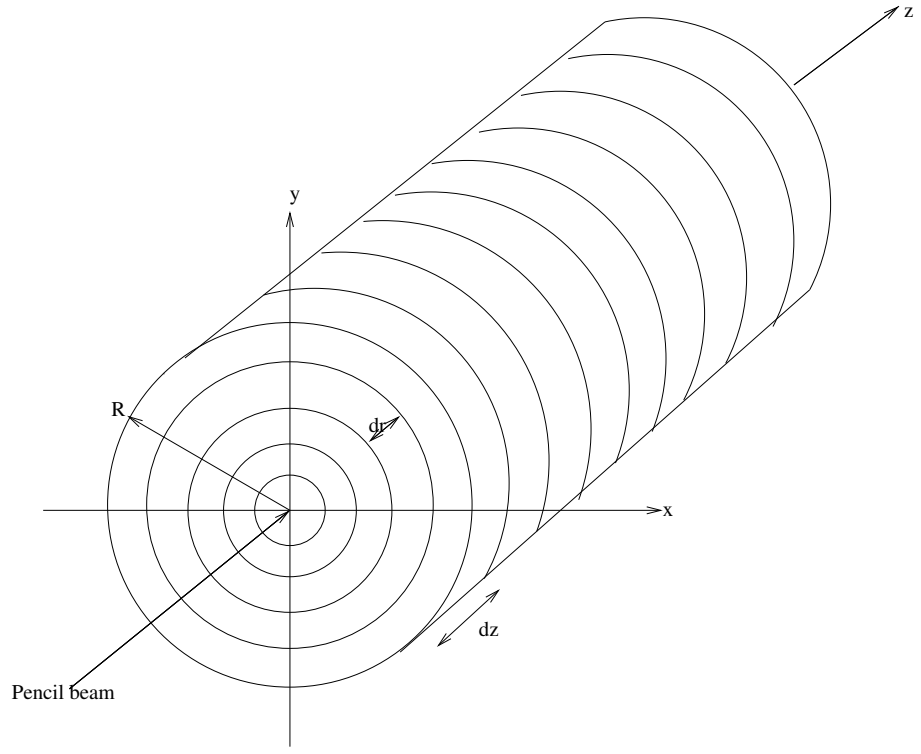

Figure 5.4: *Dose deposition geometry.*

5.4 Dose deposition geometry

The energy deposited in the water phantom was tallied into voxels in a cylindrical geometry (Fig. 5.4). The dose deposition cylinder is divided into M smaller slices ($i = 1, ..., M$) of thickness $\triangle z = 1.0$ mm, with each slice divided further into N concentric rings ($j = 1, ..., N$) of radial thickness $\triangle r = 0.5$ mm. For $E_0 = 50$ MeV results, the same geometry with slice and radial thickness of $\triangle z = 0.1$ mm and $\triangle r = 0.05$ mm respectively, was used. In this setup, the source of primary protons is taken to be placed at (0,0,0) and coincident with the z-axis (z> 0), $r = \sqrt{x^2 + y^2}$ is the radius. The energy lost by each particle traversing the medium is therefore

deposited at any point (r_i,z_j) within the 3D space. Clearly, beam scattering is radially symmetric to the beam direction (+z-axis). This geometry gives a good description of both lateral and longitudinal dose distributions in the medium, and at any given depth (z_1,z_2, ..., z_M) the integral dose in a given slice can be calculated by simply summing up dose deposited in individual rings.

Chapter 6

Results and discussion

This chapter summarizes important Geant4 simulation results and compares the dose distribution profiles with those of the analytical Ulmer beamlet model discussed in Chapter 4.

6.1 Choosing physics models

The preliminary task was to come up with the best combination of physics models and settings for a feasible and accurate simulation. To help check the sensitivity of dose distribution to different models, four reference physics lists (i.e., QGSP_BIC_EMY, QGSP_BERT, QGSP_FTFP_BERT, and FTFP_BERT (See the naming convention in Tables C.1 and C.2)) were compared. Notice that the outstanding differences in these physics lists are as given by the acronyms. Using the step size and range cut value of 1 mm for each one of these physics lists, 10^6 histories were simulated for incident proton beams of 200 MeV. As shown in Fig. 6.1, three reference physics lists: QGSP_BERT, QGSP_FTFP_BERT, and FTFP_BERT give similar dose profiles (both longitudinally and radially), implying that the physics models implemented in these physics lists differ only slightly and/or in ways that least influence the energy loss processes of the particles at this energy (i.e., $E_0 = 200$ MeV). On the other hand QGSP_BIC_EMY reference physics list produce dose profiles that are significantly different from the rest. For instance, the QGSP_BIC_EMY physics lists exhibit a Bragg peak for the (rc) group, whereas the rest do not (see Fig. 6.1e). As seen in Fig. 6.1, different physics models used in physics lists affects the dose profiles differently. One must therefore ensure the right combination of physics models and processes is established in order to achieve the intended result.

Note that the QGSP_BIC_EMY reference physics list is recommended [47] [74]

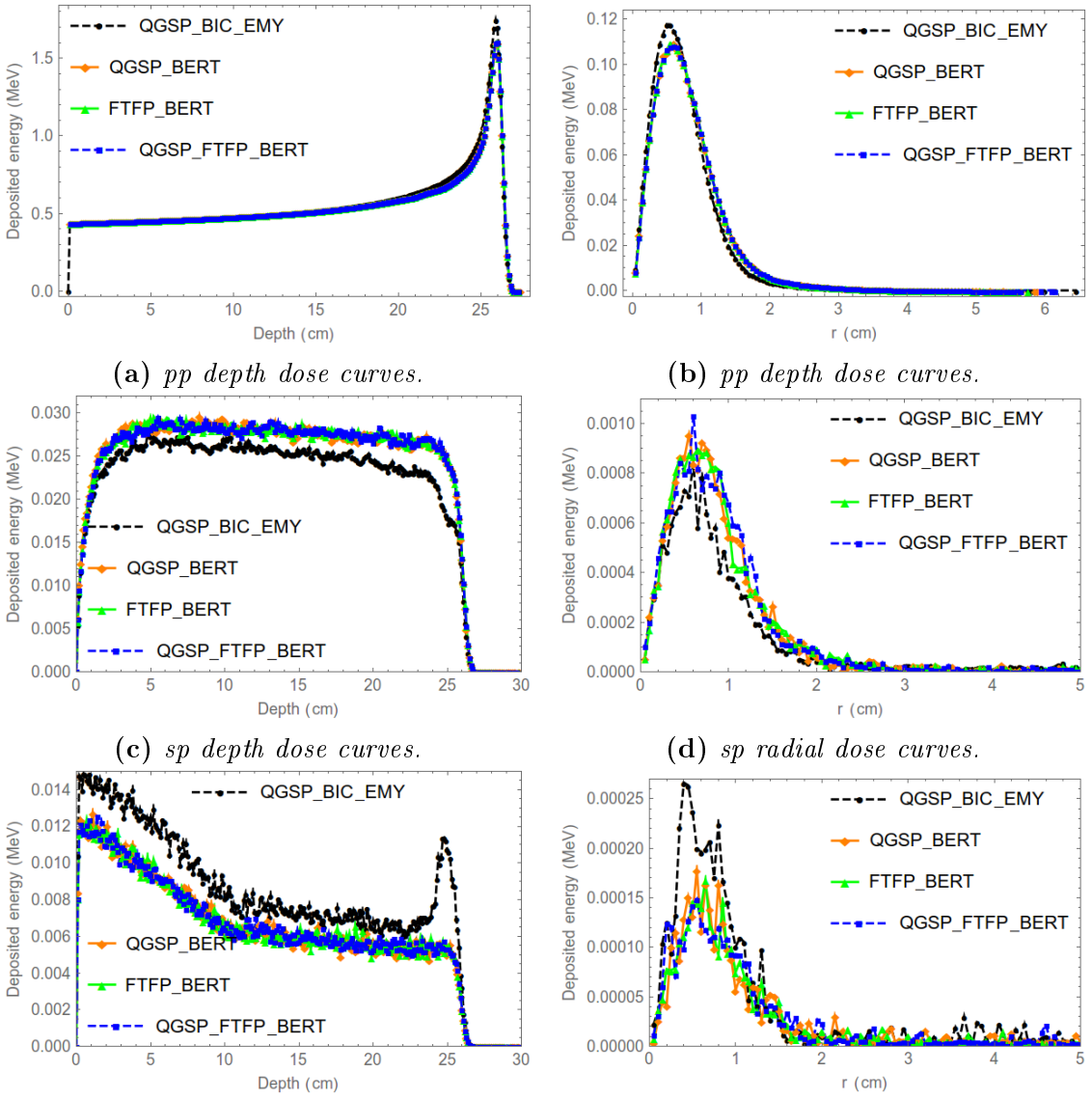

(a) *pp depth dose curves.* (b) *pp depth dose curves.*

(c) *sp depth dose curves.* (d) *sp radial dose curves.*

(e) *rc depth dose curves.* (f) *rc radial dose curves.*

Figure 6.1: *Sensitivity of dose distributions (energy deposited in water) to different physics models. Dose profiles due to the indicated reference physics lists are compared. The number of source particles is* 10^6*, incident energy,* $E_0 = 200$ *MeV, and step size and range cut values of 1.0 mm. Primary proton dose is shown in 6.1a and 6.1b, secondary protons in 6.1c and 6.1d, and recoils dose in 6.1e and 6.1f. Radial dose distributions are taken at depth,* $z = 26.0$ *cm.*

for the simulation of proton beams in the energy range of clinical interest, and was used in the current work. The other three reference physics lists are not quite ideal since they are recommended for high energy physics (HEP). They were used here to merely check the sensitivity of the dose distribution to different physics models.

As already mentioned in Sec. 5.2.1, the choice of physics lists in the current work is based on previous studies on this topic. For instance Jarlskog et al. investigated the influence of various Geant4 (version 8.1) models used to simulate electromagnetic

and nonelastic nuclear interactions, and validated them against measurements in water and with a multi-layer Faraday cup (MLFC). The MLFC is a device used to measure charge distribution of primary and secondary particles along the path of the beam. As the beam penetrates the detector, charge distribution on the plateau is mainly due to nonelastic nuclear interactions, whereas the Bragg peak near the end of the range is a result of primary protons that have only suffered EM interactions. Comparing Geant4 simulation results with longitudinal charge distributions measured using the MLFC is therefore a reliable way of validating EM and nonelastic models used in the simulation. In their study, Jarlskog et al. found that the standard EM model, the binary cascade model, and the unified hadron elastic scattering module `UHElastic` give results that agree closely with the measured data [48]. Several other authors e.g., Quesada et al. [62], Cirrone et al. [74], Ivanchenko et al. [78], have conducted similar studies and make similar recommendations.

6.2 Comparison of the Geant4 results with that of beamlet model

The Geant4 results were compared with that of the Ulmer beamlet model (see Ch. 4) for corresponding particle categories and respective primary proton energies (see Figs. 6.2-6.7) using Mathematica (version 10.2) [71]. Unless stated otherwise, the Geant4 simulations were based on the optimized parameter list and physics settings in Table 5.3. The comparisons were done for three incident proton energies: 50 MeV, 160 MeV and 230 MeV, which involved the simulation of 10^6 source protons. The results given here have been adjusted according to the procedure described in Appendix D.

The total dose distributions by the two methods compare relatively well as can be seen in Figs. 6.2a, 6.2b, 6.4a, 6.4b, 6.6a, and 6.6b, as well as Table 6.1. The influence of the build-up effect is observed to push the plateau region of the total depth dose distributions obtained by the simulations slightly above that associated with the analytical formula, Fig. 6.2a. This is caused by the (sp) and (rc) particle groups (see Figs. 6.3a and 6.3c), which are products of nuclear collisions. Moreover, the peak-diminishing effect of nuclear reactions is apparent in the Geant4 total depth dose profile (Fig. 6.2a). It must immediately be pointed out that the formulation[1] of the analytical beamlet model used here does not include the dose contribution from the reaction secondary protons (sp_r), which could explain the lack of the build-up

[1]The April 2007 Proton Algorithm Reference Guide-Eclipse^{TM}.

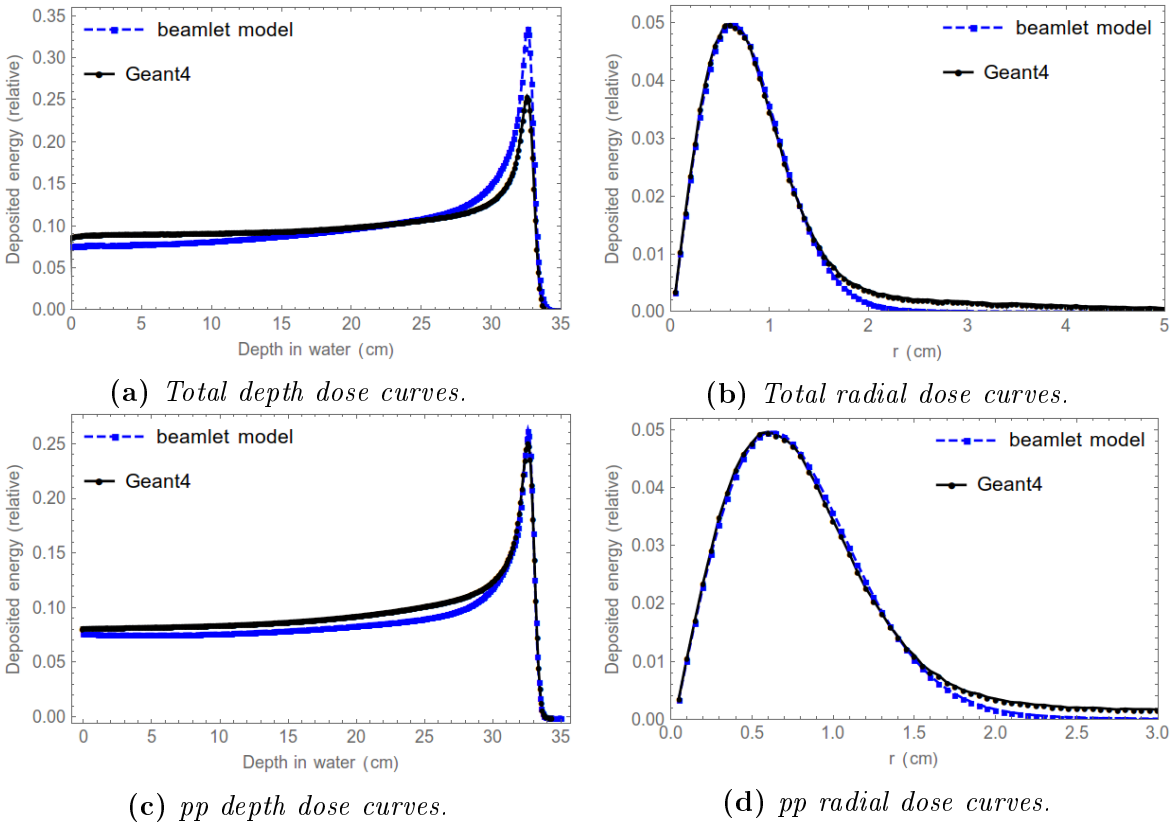

(a) *Total depth dose curves.*

(b) *Total radial dose curves.*

(c) *pp depth dose curves.*

(d) *pp radial dose curves.*

Figure 6.2: *Comparison of Geant4 simulation dose profiles against that of the beamlet model for incident proton pencil beam of $E_0 = 230$ MeV. Total dose distribution (longitudinal and lateral) is shown in 6.2a and 6.2b, while the primary proton dose distribution is shown in panes 6.2c and 6.2d. The radial dose distributions were taken at depth $z = 32.0$ cm.*

effect in their total depth dose distribution. Looking at Figs. 6.2a, 6.4a, and 6.6a, one can immediately see the dependence of the build-up effect on the incident proton energy. Basically, as protons impinge on water secondaries begin to be created. They rapidly increase to what is known as the *longitudinal equilibrium* within about two centimeters (approximately the characteristic range of secondary protons) for secondary protons and a few millimeters ($\ll$1.0 mm) for electrons [1]. This phenomenon also explains the almost non-zero entrance dose observed for the (rc) and (sp) particle categories in the simulations results (see Figs. 6.3a, 6.3c, 6.5c, etc.).

By definition, the range cut controls the generation and tracking of secondary particles. The smaller the cut-off value, the more secondaries are tracked. The effect of the range cut on the dose distribution also depends on the incident proton beam energy. In relation to the build-up effect, the effect of a smaller range cut value begins to be more apparent at incident energies of about 200 MeV and above. As can be seen in Figs. 6.3c, 6.5c and 6.7c, the range cut value of 1.0 mm (for e^-, e^+ and γ) yields different (rc) dose profiles at 230 MeV, 160 MeV and 50 MeV, respectively.

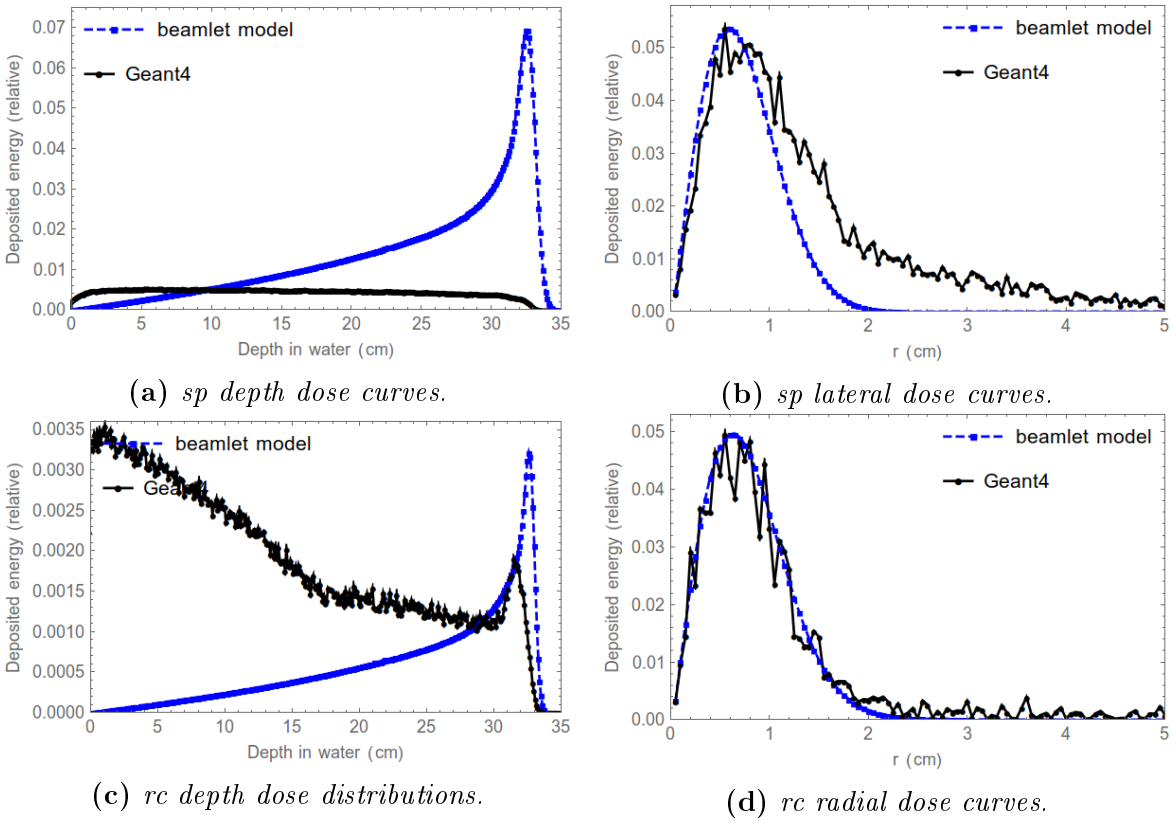

(a) *sp depth dose curves.*

(b) *sp lateral dose curves.*

(c) *rc depth dose distributions.*

(d) *rc radial dose curves.*

Figure 6.3: *Comparisons of Geant4 simulation dose profiles against that of the Ulmer beamlet model for incident proton energy of 230 MeV. Radial dose distributions taken at depth $z = 32.0$ cm. Secondary proton dose profiles are shown in 6.3a and 6.3b, while the the heavy recoil ions and secondaries other than protons are shown in 6.3c and 6.3d.*

Another physical manifestation worth discussing is the lack of a Bragg peak in the (sp) depth dose distribution (Figs. 6.3a, 6.5a, and 6.7a) of the simulations. It has been shown by some authors, e.g., Tung et al. [60] (see Fig. 2.3), Paganetti et al. [58], Fippel et al. [79], Medin et al. [59], etc., using different Monte Carlo packages that dose profiles of secondary protons do not exhibit a Bragg peak. However, the authors of the beamlet model categorized secondary protons into reaction (sp_r) and nonreaction (sp_n) as discussed in Sec. 4.4, and showed that the dose distribution for reaction secondary protons (sp_r) from their Geant4 simulation is without a Bragg peak (see Fig. 4.1), whereas nonreaction secondary protons (sp_n) exhibit a Bragg peak, albeit broader and shifted to a lower depth [35].

The lack of a Bragg peak can partly be attributed to the booking or tallying of energy deposited by individual particles. In our simulations, particle tracking and categorization was done using the particle name tags in conjunction with the particle ID. This means that only the energy deposited by primary protons and secondary

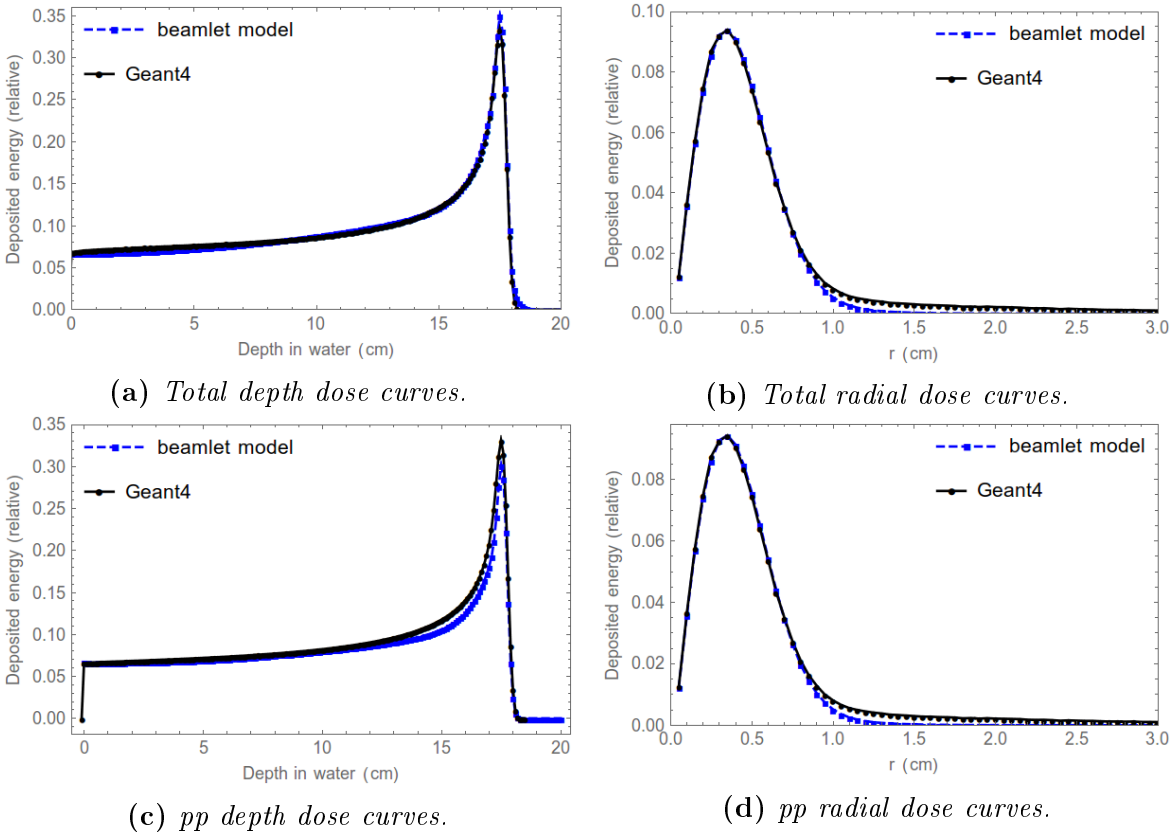

(a) *Total depth dose curves.*

(b) *Total radial dose curves.*

(c) *pp depth dose curves.*

(d) *pp radial dose curves.*

Figure 6.4: *Comparisons of Geant4 simulation dose profiles against that of the Ulmer beamlet model for incident proton energy of 160 MeV. The radial dose profiles are taken at depth $z = 17.0$ cm. Total dose profiles are shown in 6.4a and 6.4b, while the primary proton dose profiles are shown in panes 6.4c and 6.4d.*

protons is allocated to (pp) and (sp) groups, respectively, the energy deposited by the rest of the particles is booked into the (rc) group. Thus, other processes that ideally should be contributing to the protons groups, e.g., electrons produced by secondary protons, have their resulting dose assigned to the (rc) group. Moreover, in Geant4 simulation secondary protons are purely a result of nonelastic nuclear collisions, whereas in the beamlet model primary protons that suffer elastic nuclear scattering are booked as nonreaction secondary protons ($\mathrm{sp_n}$) [35].

Under the conditions set in Appendix D, major discrepancies between the simulation results and the Ulmer beamlet-dose functions are observed, especially for individual particle categories (pp, sp, and rc), Figs. 6.2c, 6.3a, 6.3b, 6.3c, 6.5b, 6.7a, 6.7b, 6.7c, 6.7d, etc. These discrepancies can partly be attributed to the dose tallying procedure explained above. The differences in the hadronic physics (or the nonelastic interaction cross-section data) and multiple scattering models used in the two versions of Geant4 (i.e., version 7.1 in the beamlet model and version 10.1 in the current work) could also explain the discrepancies in these plots. For instance, authors of the

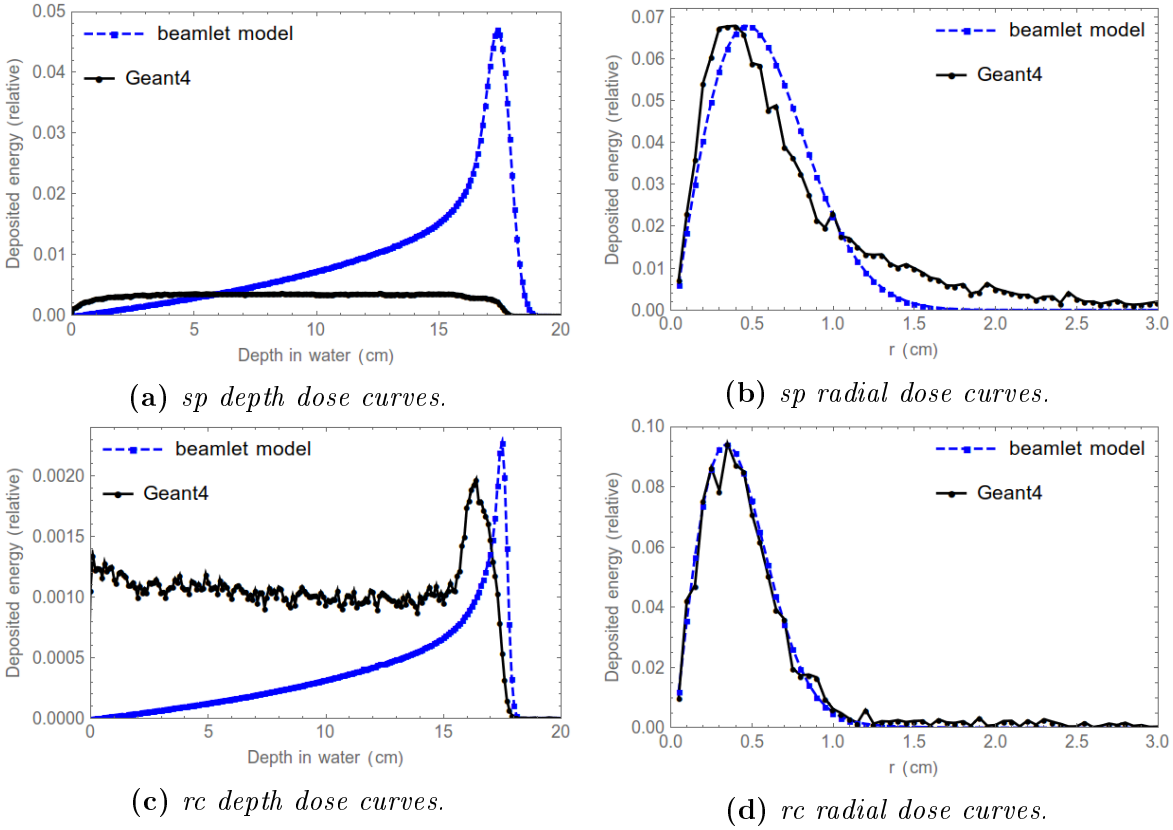

(a) *sp depth dose curves.*

(b) *sp radial dose curves.*

(c) *rc depth dose curves.*

(d) *rc radial dose curves.*

Figure 6.5: *Comparisons of Geant4 simulation dose distributions with that of the Ulmer beamlet model for $E_0 = 160$ MeV. The radial dose profiles are taken at depth $z = 17.0$ cm. The secondary proton dose is shown in panes 6.5a and 6.5b, while heavy recoils dose is shown in panes 6.5c and 6.5d.*

beamlet model replaced the default nonelastic nuclear cross-section data of Berger [80], that was implemented in Geant4 version 7.1, by the ^{16}O nuclear cross-section data of Chadwick and Young [69]. For the same purpose, version 10.1 of Geant4 uses the data driven `G4ProtonInelastic CrossSection` (see Table 5.1). Similarly, the authors of the beamlet model used Molière's theory to model MSC, whereas in the current version of Geant4 the Urbàn model is implemented (see Sec. 2.2.2). Furthermore, the differences in the secondary proton (sp) radial dose distributions (see Figs. 6.3b and 6.5b) can be attributed to the fact that a single Gaussian (Eq. 4.4.7) is used to approximate the radial dose distribution of secondary protons (sp) in the beamlet model. However, the radial dose distributions of primary protons (pp) is approximated by the sum of two Gaussians (Eq. 4.3.6): one to account for the central part and the other for the large angle single scattering. This explains why the beamlet model (pp) radial dose profiles compares closely with that of the simulations (Figs. 6.2d, 6.4d, etc.).

Finally, the analytical dose distribution functions of the Ulmer beamlet model that

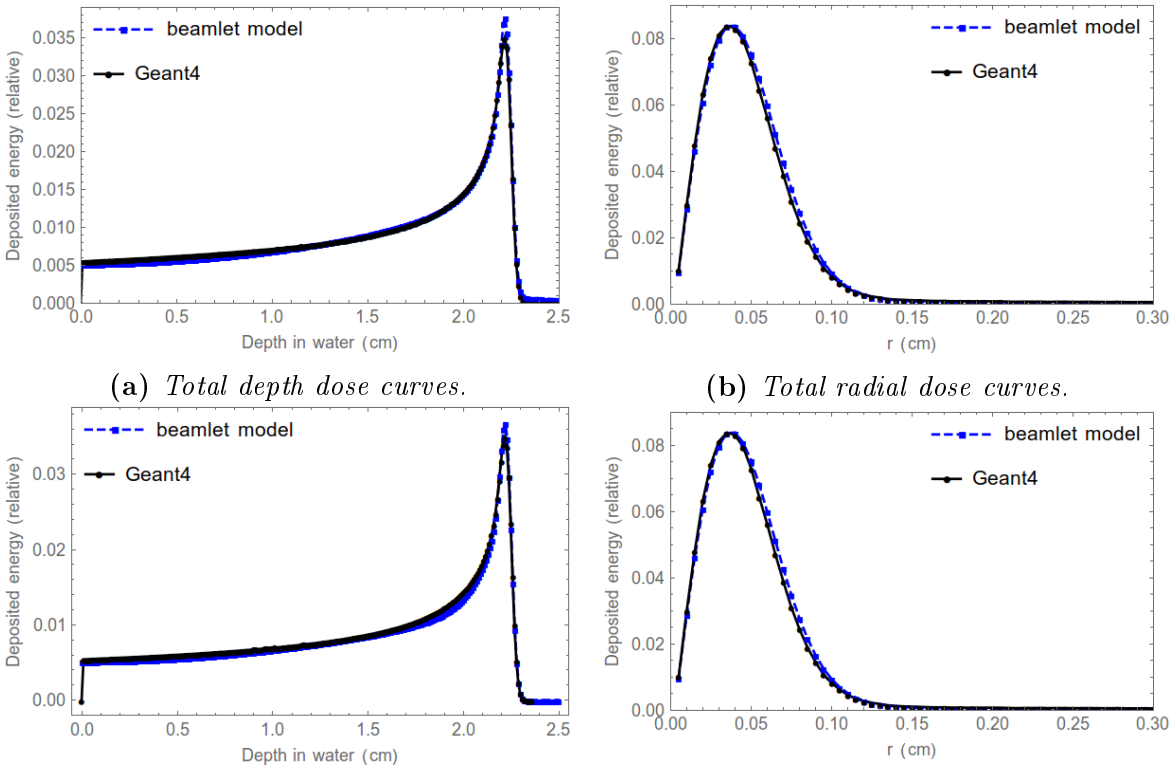

(a) *Total depth dose curves.* (b) *Total radial dose curves.*

(c) *pp depth dose curves.* (d) *pp radial dose curves.*

Figure 6.6: *Comparisons of Geant4 simulation dose distributions with that of the Ulmer beamlet model for $E_0 = 50$ MeV. The radial dose profile is taken at depth $z = 2.0$ cm. The total dose profiles are shown in panes 6.6a and 6.6b, and the dose profiles for the primary protons is shown in panes 6.6c and 6.6d.*

are implemented in the April 2007 Varian medical systems manual[2] for proton treatment planning have been compared with Geant4 MC simulations. A good correspondence was found between the total depth dose distributions of the two methods. It has been observed that the analytical functions do not exhibit the build-up effect which is expected at higher energies (see 6.2a). This could be because the improve-

	E_0 (MeV)	R_{100} (cm)	R_{80} (cm)	R_{50} (cm)	FWHM (cm)	Entrance dose to BP ratio	ICRU (49) R_{CSDA} (cm)
Geant4	230	32.82	33.14	33.35	3.35	0.35	32.95
	160	17.61	17.79	17.90	1.31	0.21	17.65
	50	2.22	2.24	2.26	0.17	0.16	2.227
Beamlet model	230	32.61	32.90	33.11	2.38	0.24	32.95
	160	17.51	17.68	17.79	1.25	0.19	17.65
	50	2.22	2.24	2.26	0.15	0.13	2.227

Table 6.1: *Values for the total dose distributions obtained from the Geant4 simulations and the beamlet model. The range values stated here were obtained before the shift (discussed in Appendix D) was applied.*

ments Ulmer et al. made to the model in the publications [35] [32] [57] may have

[2]Proton Algorithm Reference Guide-Eclipse^{TM}, April 2007

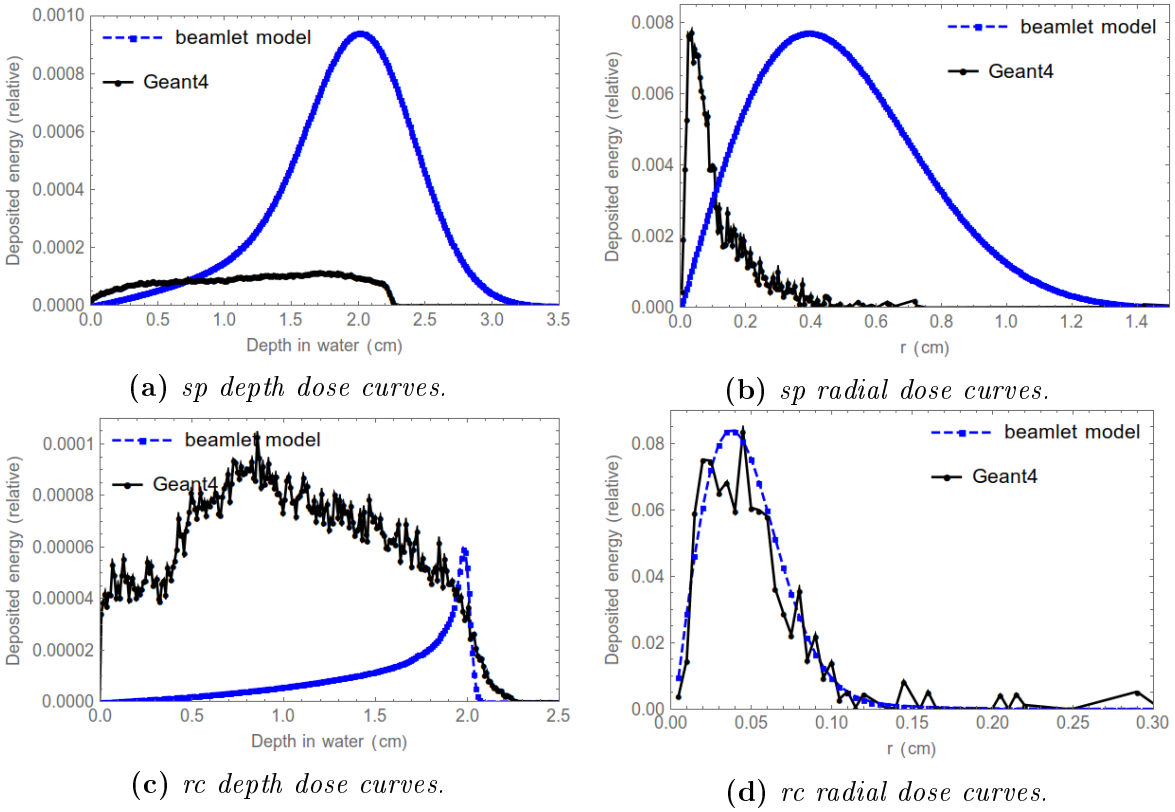

(a) *sp depth dose curves.*

(b) *sp radial dose curves.*

(c) *rc depth dose curves.*

(d) *rc radial dose curves.*

Figure 6.7: *Comparisons of Geant4 simulation dose distributions with that of the Ulmer beamlet model for E_0 = 50 MeV. The radial dose distribution is taken at depth z=2.0 cm. The secondary dose profiles are shown in 6.7a and 6.7b, while the recoil ion dose profiles are shown in 6.7c and 6.7d.*

only been implemented in the latter versions of the Eclipse proton treatment planning system (TPS). The Ulmer et al. papers also cater for the reaction secondary protons (sp_r), which is not treated in the Eclipse implementation used here. The

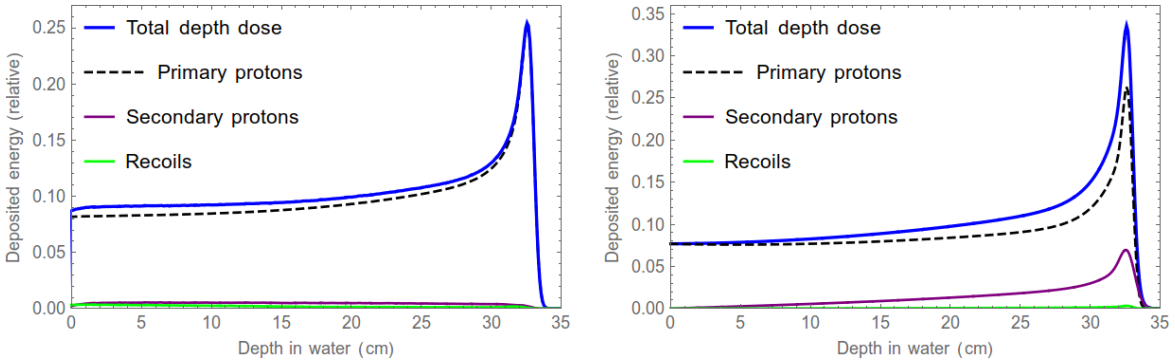

(a) *pp, sp, rc depth dose contributions-simulations.*

(b) *pp, sp, rc depth dose contributions-beamlet model.*

Figure 6.8: *Dose contributions of the pp, sp, and rc at E_0 = 230 MeV for (a) Geant4 simulations and (b) Ulmer beamlet model.*

full-width at half maximum (FWHM) and the entrance-to-peak ratio of the total depth dose distributions for the two cases were also compared and the values are given in Table 6.1. The percentage differences in the entrance-to-peak ratio between simulations and the formulae are 11%, 2%, and 3% for the 230 MeV, 160 MeV, and 50 MeV respectively. Differences of up to about 1 cm are seen in the FWHM of the two cases (for $E_0 = 230$ MeV). Except for 230 MeV simulation result, both the simulated and the analytical model R_{80} ranges compare favourably with the R_{CSDA} values as given by the ICRU report 49 [44].

Fig. 6.8 gives a summary of the different ways the particle groups (pp), (sp), and (rc) contribute to the total depth dose distribution (at $E_0 = 230$ MeV) in the simulations and the Ulmer beamlet model. Clearly, the entrance dose for these three particle groups differ significantly between the two cases, which as already mentioned, can partially be explained by the slightly different approaches taken in tallying their dose in the two methods.

Chapter 7

Conclusion

7.1 Summary

The Geant4 Monte Carlo simulation toolkit is a complete open source code for simulating passage of particles or radiation through matter. It offers the user a wide range of options for building the detector geometry, material, physics processes and models, particles, and data analysis tools, in addition to allowing the user to take full control of the simulation. In this work, Geant4 (version 10.1) has been used to assess the contribution of primary protons, secondary protons, heavy recoils and other secondaries to the total energy deposited in water when a proton pencil beam in the clinical energy range passes through it (water). A list of parameters (step sizes, range cuts, etc.) and physics settings that enabled a balance between the accuracy and the feasibility of the simulation (given the computational constraints) was proposed. Because it is validated and is highly recommended for simulation of protons traversing water in the clinical energy range, the QGSP_BIC_EMY reference physics list was adopted after comparisons with alternative physics lists. Besides, this physics list mostly makes use of the physics components that are known to yield best results (e.g., the binary cascade model of nucleon and heavy ion interactions, the Urbàn MSC model, standard EM option 3, etc.). In order to control the accumulation of dose for secondary particles and to achieve convergence in the dose profiles, it was necessary to introduce individual range cuts for protons and electrons.

Overall, the total dose distributions (both depth dependent and lateral) of the simulations and the analytical model show some good correspondence, except for some deviations which are likely related to the build-up effect by secondary particles in the plateau region. We may not have seen the build-up effect in the analytical model because the functions used here ignores the dose contribution of the reaction protons.

However, major discrepancies are manifest in the dose profiles of individual particle categories, especially at 50 MeV. These discrepancies could be as a result of the differences in the energy tallying procedure, hadronic physics models (or nonelastic nuclear cross-section data), and multiple Coulomb scattering models between the two methods.
Finally, the dose contribution of primary protons, secondary protons, and generally, heavy recoil ions to the total dose has been successfully investigated and compared to the analytical Ulmer beamlet model.

7.2 Possible further work

Future work should focus on the dose deposited by electrons and how to assign it correctly to the (pp), (sp), (rc) particle groups. It would also be interesting to distinguish the (sp) particle group into "reaction" and "non-reaction" secondary protons, like Ulmer et al. did, and investigate their dose contributions separately. Furthermore, it would be sensible to validate the Geant4 simulation results with measured data from machines that produce nearly monoenergetic pencil beams. The formulae for the analytical beamlet model used here are from the April 2007 Varian Eclipse Proton Algorithm Reference Guide. It would be necessary in future to compare the Geant4 results with the more recent version of the manual, in which the improvements done on the beamlet model by Ulmer et al. in the latter publications [35] [32] [57] [68] are implemented.

Appendix A

Proton kinematics

In the stopping and scattering theories of proton energy loss, it sometimes becomes useful to calculate the proton's speed v or momentum p, given its kinetic energy. The following equations can be used:

$$\beta \equiv \frac{v}{c} = \frac{pc}{E + mc^2}, \tag{A.0.1}$$

$$(E + mc^2)^2 = (pc)^2 + (mc^2)^2. \tag{A.0.2}$$

If we define a *reduced kinetic energy*,

$$\tau \equiv \frac{E}{mc^2} \tag{A.0.3}$$

the following derivations whose relativistic ($\tau \gg 1$) and non-relativistic ($\tau \ll 1$) limits are obvious can be made:

$$\beta^2 = \frac{\tau + 2}{(\tau + 1)^2}\tau, \tag{A.0.4}$$

$$(pc)^2 = (\tau + 2)mc^2E, \tag{A.0.5}$$

and

$$pv = \frac{\tau + 2}{\tau + 1}E, \tag{A.0.6}$$

pv appears frequently in MCS theory.

Appendix B

Basic beam configurations

This appendix gives a brief introduction to the mathematical definitions and concepts of simple beam configurations.

B.1 Beam coordinate system

Let $\mathcal{B}$ be a three-dimensional, right-handed Cartesian beam coordinate system. A point $\vec{r}$ in space has Cartesian coordinates (x, y, z) relative to $\mathcal{B}$. This beam coordinate system will be used to give a geometrical description of all quantities of interest. The Euclidean norm of $\vec{r}$ will be given by $|\,\vec{r}\,|$. In cylindrical coordinates $\vec{r} = (r, \phi, z)$, with

$$x = r\cos\phi, \quad y = r\sin\phi, \quad r \;= \sqrt{x^2 + y^2}, \quad \phi = \arctan2\,(x, y) \tag{B.1.1}$$

The arctangent function arctan2 gives a principal value of the argument of the non-zero complex number (x, y).

B.2 Mathematical notation

Let $f(\vec{r}) = f(x, y, z) = f(x, \phi, z)$ be a function representing the spatial dependency of some arbitrary quantity f. Here (r, ϕ, z) represents the cylindrical coordinates of the point $\vec{r} = (x, y, z)$ as given in (B.1.1).

A function $f(\vec{r})$ is said to be radially symmetric about the z-axis of the coordinate system $\mathcal{B}$ if

$$f(r, \phi, z) = f(r, 0, z) \quad \forall\phi \in \quad (0, 2\pi] \quad \text{and} \quad \forall z \in \mathbb{R}. \tag{B.2.1}$$

Since f does not depend on radial direction ϕ, the notation $f(\vec{r}) = f(r, z)$ will be used henceforth.

The radial integral of a function $f(\vec{r})$ over an arbitrary area $A(z)$ of a planar surface that intersects the z-axis at $(0, 0, z)$, and which is orthogonal to the z-axis is given by

$$F[A](z) = \int \int_{A(z)} f(x, y, z)dxdy. \tag{B.2.2}$$

If the z-axis passes through the interior of $A(z)$ for all z, then eq. B.2.2 can be written as

$$F[A](z) = \int_0^{2\pi} d\phi \int_0^{R(\phi,z)} f(r, \phi, z)rdr, \tag{B.2.3}$$

with $R(\phi, z)$ being the distance to the perimeter of the area $A(z)$ as a function of radial distance ϕ.
If $A(z)$ is circular and centred around the z-axis, and if radius R of $A(z)$ is constant for all z, then equation B.2.3 can be written as

$$F[A](z) = F(R; z), \tag{B.2.4}$$

with

$$F(R; z) = \int_0^{2\pi} d\phi \int_0^{R} f(r, \phi, z)rdr \tag{B.2.5}$$

and, if f is radially symmetric, B.2.5 reduces to

$$F(R; z) = 2\pi \int_0^{R} f(r, \phi, z)rdr. \tag{B.2.6}$$

We define radial convolution of two functions g and f, $g \otimes f$ as the two-dimensional integral

$$(g \otimes f)(z; \vec{r}) = \int_{-\infty}^{\infty} \int_{-\infty}^{\infty} g(x', y', z)f(x - x', y - y', z)dx'dy'. \tag{B.2.7}$$

In equation B.2.7, the function f is referred to as the "kernel" of the convolution. Since the dependency of g, and $g \otimes f$ on the z will most of the time be implicit, we can write $g(x, y, z_0) = g(x, y)$, and $(g \otimes f)(z, \vec{r}) = (g \otimes f)(\vec{r})$.

The conditions under which the convolution exists is beyond the scope of this work. For our case, it is sufficient to note that $(g \otimes f)$ exists if $g(x, y)$ is bounded in $\mathbb{R}^2$ (or $g(x, y)$ has a compact support in $\mathbb{R}^2$), and $f(r, \phi, z)$ decays rapidly to zero as $r \to \infty$ for all $\phi \in [0, 2\pi]$. If f is radially symmetric, then

$$\begin{aligned}(g \otimes f)(\vec{r}) &= \int_{-\infty}^{\infty} \int_{-\infty}^{\infty} g(x', y')f(\varrho, z)dx'dy' \\ &= \int_0^{2\pi} d\phi' \int_0^{\infty} g(r', \phi')f(\varrho, z)r'dr',\end{aligned} \tag{B.2.8}$$

where

$$\left.\begin{aligned} x &= r\cos\phi, & x' &= r'\cos\phi', \\ y &= r\sin\phi, & y' &= r'\sin\phi', \\ \varrho &= \sqrt{(x-x')^2+(y-y')^2} & & \\ &= \sqrt{r^2+r'^2-2rr'\cos(\phi-\phi')} & & \end{aligned}\right\}. \tag{B.2.9}$$

B.3 Simple beam configurations

If we define a semi-infinite medium as a medium made of some material of density ρ (g/cm^3) occupying the region $\mathbb{R}\times\mathbb{R}\times[0,\infty)\subset\mathbb{R}^3$. The dose deposited at an arbitrary point $\vec{r}=(x,y,z)$ in the semi-infinite medium by a monoenergetic pencil beam assumed to be incident at the point $\vec{r}_s=(0,0,0)$ (in this work, the incident point is the same as the source point of primary protons) with an initial direction of $\vec{k}=(0,0,z)$ can be expressed as

$$D(E_0;\vec{r}) = \mathrm{N}_{sp}\mathfrak{D}_{pb}(E_0;\vec{r}), \tag{B.3.1}$$

where $\mathfrak{D}_{pb}(E_0;\vec{r})$ is the absorbed dose, per source proton, at $\vec{r}$ in the medium, and N_{sp} is the number of source protons. $\mathfrak{D}_{pb}$ is radially symmetric in the $x-y$ plane, hence can be expressed as

$$\mathfrak{D}_{pb}(E_0;\vec{r}) = \mathfrak{D}_{pb}(E_0;r,z), \tag{B.3.2}$$

where $r=\sqrt{x^2+y^2}$. For a given medium material (e.g., water), $\mathfrak{D}_{pb}(E_0;r,z)$ is referred to as the *pencil kernel*, given in units of MeV/g [63]. It is a three-dimensional distribution of the dose due to a pencil beam.

If we now consider a number protons emerging parallel from a source plane $\mathcal{P}_s\subset\mathbb{R}^3$, on the $x-y$ plane at $z=0$ and directed into (parallel to the z-axis) the homogeneous semi-infinite medium, the dose deposited at a given point $\vec{r}$ in the medium is a convolution of energy deposited by each of these narrow proton beams:

$$\begin{aligned} D_{pp}(\vec{r}) &= \int_0^\infty (\Phi'_{pp}(E)\otimes\mathfrak{D}_{pb}(E))(\vec{r})dE \\ &= \int_0^\infty dE\int_{-\infty}^{\infty}\int_{-\infty}^{\infty}\Phi'_{pp}(x',y',E)\mathfrak{D}_{pb}(E;x-x',y-y',z)dx'dy', \end{aligned} \tag{B.3.3}$$

where $\Phi'_{pp}(E;x',y')$ denotes the initial energy spectrum of the protons at $\vec{r}=(x,y,0)$, and $\mathfrak{D}_{pb}(E;\vec{r})$ the dose deposited at the point $\vec{r}$, per source proton, by a pencil beam of energy E. Using results of Eqs. (B.2.7-B.2.8), Eq. (B.3.3) can be expressed as

$$D_{pp}(\vec{r}) = \int_0^\infty dE\int_0^{2\pi}d\phi\int_0^\infty \Phi'_{pp}(E;r',\phi')\mathfrak{D}_{pb}(E;\varrho,z)r'dr', \tag{B.3.4}$$

where $r^{'}$, $\phi^{'}$, and ϱ are given by Eq. (B.2.9).
For a circular plane-parallel proton beam of radius R with uniform energy spectrum inside the field centred around the z-axis, then

$$\Phi^{'}_{pp}(E; r^{'}, \phi^{'}) = \begin{cases} \Phi^{'}_{pp}(E) & \text{if} \quad r^{'} \leq R \\ 0 & \text{if} \quad r^{'} > R \end{cases} . \tag{B.3.5}$$

Eq. (B.3.4) can therefore be re-defined to express the dose on the central axis of the beam as

$$D_{pp}(R; z) = 2\pi\Phi_{pp} \int_0^R \mathfrak{D}_{pb}(r, z) r dr, \tag{B.3.6}$$

where

$$\mathfrak{D}_{pb}(\vec{r}) = \int_0^\infty \psi_{pp}(E)\mathfrak{D}_{pb}(E; \vec{r}) dE, \tag{B.3.7}$$

and

$$\psi_{pp}(E) = \Phi^{'}_{pp}(E)/\Phi_{pp}. \tag{B.3.8}$$

Here, Φ_{pp} is the uniform fluence inside the field, while $\psi_{pp}(E)$ is the energy distribution of the plane-parallel beam, normalized to 1:

$$\int_0^\infty \psi_{pp}(E) dE = 1. \tag{B.3.9}$$

The quantity $\mathfrak{D}_{pb}(\vec{r})$ is the dose deposited, per source proton, at the point $\vec{r}$ by the polyenergetic pencil beam with energy distribution $\psi_{pp}(E)$.
Eq. (B.3.6) can be re-written as

$$\mathfrak{D}_{pp}(R; z) = 2\pi \int_0^R \mathfrak{D}_{pb}(r, z) r dr, \tag{B.3.10}$$

where $\mathfrak{D}_{pp} = D_{pp}/\Phi_{pp}$ is the dose deposited, per source proton, by the plane-parallel beam (or broad beam). Eq. (B.3.10) gives a simple but very important mathematical relation between pencil beams and broad beams, known as the reciprocity principle [59] [63]. The reciprocity relationship has been used to obtain the properties of broad electron beams from experiments or calculations based on pencil beams [81].

Appendix C

Reference physics list naming convention

Acronym	Description
QGS:	Quark Gluon String model (>∼20 GeV)
FTF:	Fritiof string model (>∼5 GeV)
BIC:	Binary Intra-nuclear Cascade (<∼10 GeV)
BERT:	Bertini-style Intra-nuclear Cascade (<∼10 GeV)
HP:	High Precision neutron transport models (<20 MeV)
P:	G4Precompound model used for nuclear de-excitation

Table C.1: *Acronyms used to refer to various hadronic options.*

No Suffix:	Standard EM physics
_EMV:	(Option 1) older but faster EM processes
_EMY or _EMZ:	(Option 3 or Option 4) suitable for low energy EM
LIV:	Uses Livermore data bases
PEN:	Penelope-bases EM models

Table C.2: *Suffixes used to refer to EM options.*

C.1 A brief description of the reference physics lists

In this appendix we briefly discuss the reference physics lists that were used to check the sensitivity of dose profiles on different physics models. A detailed description of reference physics lists can be found in [82].

C.1.1 QGSP_BIC_EMY

- Applies the quark gluon string model to describe high energy interactions of protons and neutrons with nuclei.
- High energy interactions create an excited nucleus, which is passed to the Precompound model which is responsible for the nuclear de-excitation.
- It uses the Geant4 binary cascade model to describe the production of secondary particles during the interaction of protons and neutrons with nuclei.
- It also uses the binary light-ion cascade to model inelastic interaction of ions (see Tables 5.1 and 5.2).

C.1.2 QGSP_BERT

- Like the QGSP but uses the Geant4 Bertini cascade model for inelastic interaction of protons and neutrons with the nuclei.
- The Bertini uses its own Pre-equilibrium and equilibrium models to describe de-excitation of the residual nuclei (see Sec. 2.3.1).

C.1.3 FTFP_BERT

- Uses the Fritiof string model to describe the excitation and fragmentation of the nucleus.
- Also uses the Bertini cascade model for inelastic nuclear interactions of protons and neutrons with nuclei.

C.1.4 QGSP_FTFP_BERT

- Uses both the quark gluon and Fritiof string models to describe the excitation of the nucleus during the interaction of high energy protons and neutrons with the nuclei.
- Also uses the Bertini cascade model to describe the de-excitation of the nucleus.

Appendix D

Normalization of the dose distributions

Since the dose distribution obtained from Geant4 simulations are integrals of the dose deposited in each slice or ring (see Sec. 5.4 and Fig. 5.4), the dose functions of the analytical beamlet model had to be integrated using the same slice/ring thicknesses (z_i and r_j) as the ones used in the Geant4 simulation. That is, the dose functions of the analytical beamlet model were integrated from z_i to z_{i+1} and r_j to r_{j+1} for the depth dose and the radial dose distributions respectively. It is also worth noting that the radial dose distribution curves of the Geant4 simulations are obtained using the function of the form $2\pi \int_{r_j}^{r_{j+1}} f(r,z)rdr$ whereas the underlying radial dose distribution function in the beamlet model is simply $f(r,z)$, hence the difference observed in Fig. D.1a. In order to properly compare the radial dose curves by these two methods, it was necessary to integrate the analytical radial dose formulae as stipulated here (see Fig. D.1b).

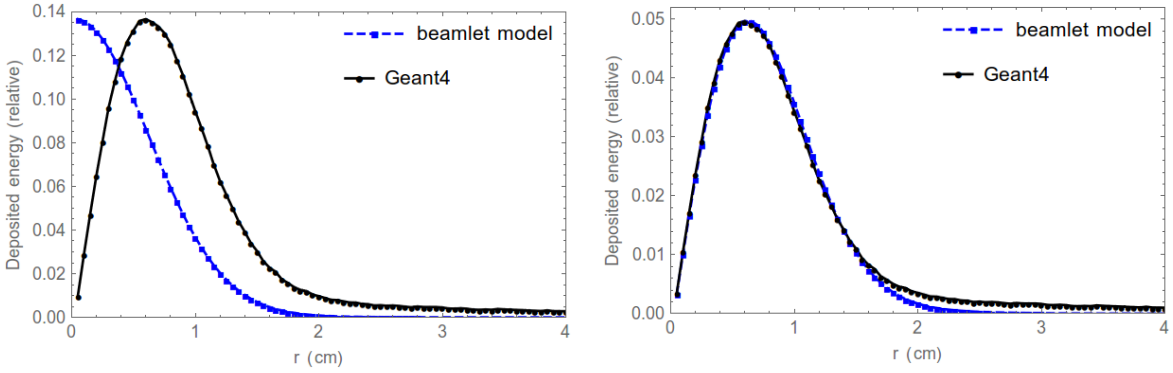

(a) *Un-normalized.* **(b)** *Normalized.*

Figure D.1: *In D.1a the radial dose curve for the beamlet model is given by $f(r,z)$, whereas in D.1b it is given by $2\pi f(r,z)r$, which is the same function used in the simulations.*

Owing to the fact that even slight differences in the energy-range tables used to obtain the dose curves (formulae vs simulations) can readily cause differences in the range, there was need to take corrective measures. In this case, comparing the R_{80} ranges (i.e., the depth at 80% of the maximum dose in the distal fall-off region of the Bragg peak) of the total depth dose distributions from the two methods was good enough. Whenever there was a difference the total dose curve of the simulations was shifted accordingly so that it matches the R_{80} range as given by the beamlet model. The same shift was also applied to the dose distributions of the particle categories (pp, sp, and rc). The R_{80} closely matches the CSDA range R_{CSDA} for monoenergetic protons.

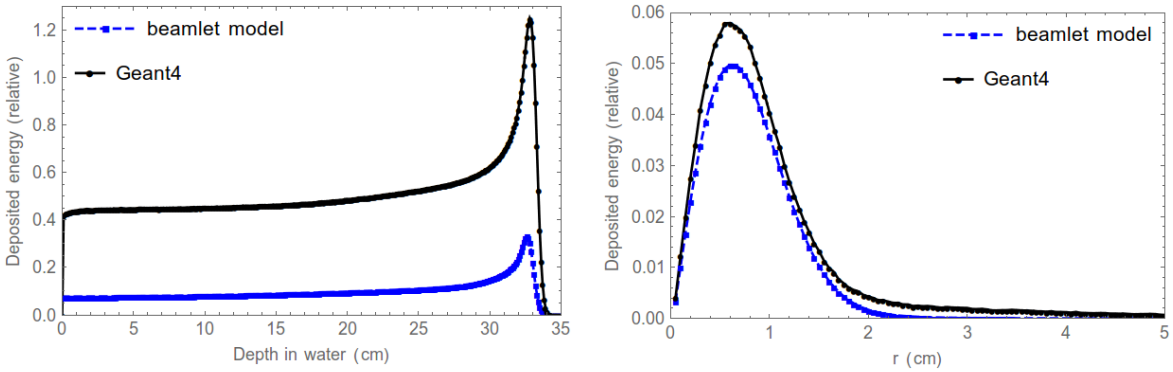

(a) *Depth dose curves.* **(b)** *Radial dose curves.*

Figure D.2: *Un-normalized dose distributions.*

In some cases, the dose distribution by one method were found to be much lower than that of the other when put on the same scale (see Fig. D.2). In our attempt to make proper comparisons, it became necessary to normalize the dose curves for the two methods. Particularly for the depth dose distributions, a normalization factor was computed using the requirement that the total dose, as obtained by integrating the total depth-dose distributions over all depths, are the same for the two cases (i.e., simulation and the beamlet model). The same factor was also applied to depth dose distributions of particle categories: (pp), (sp), and (rc). This undertaking is justifiable as it is in line with the requirement that the total energy must be conserved, i.e., Eq. (3.2.7). To normalize the radial dose distributions we initially applied the sum rule Eq. (3.2.8), that is divide the dose in each ring by the sum of the dose in all the rings (entire slice) at that depth z_i. However, this undertaking could not get the radial dose peaks of the two methods to properly match as the simulation radial profiles have longer tails. As such, the respective radial dose distributions of the two methods were simply normalized by forcing their peak values to be equal.

Appendix E

Convergence of dose curves due to the range cut

In trying to find the range cut that meets our requirements, several values were tested. Convergence in the dose distributions could not be achieved when all the particles were assigned the same range cut value (Fig. E.1). It was however achieved when electrons and protons were assigned individual cut-off values. Fig. E.2 shows the dose distributions when the range cuts for protons are compared (0.01 mm, 0.1 mm, and 1.0 mm) while that of the electrons is fixed at 1.0 mm. As can be seen, the dose distributions converge almost immediately. The lack of convergence when only one cut value is applied to all particles should be expected since the purpose of the cut-off value is to control the tracking of generated secondary particles (e.g., electrons, gammas, positrons, and protons). As can be seen in Fig. E.1a, the smaller the range cut value the lower the plateau region for primary protons. This is expected as a smaller range cut value leads to creation of more secondaries even at lower energies (see Figs. E.1e and E.1f).

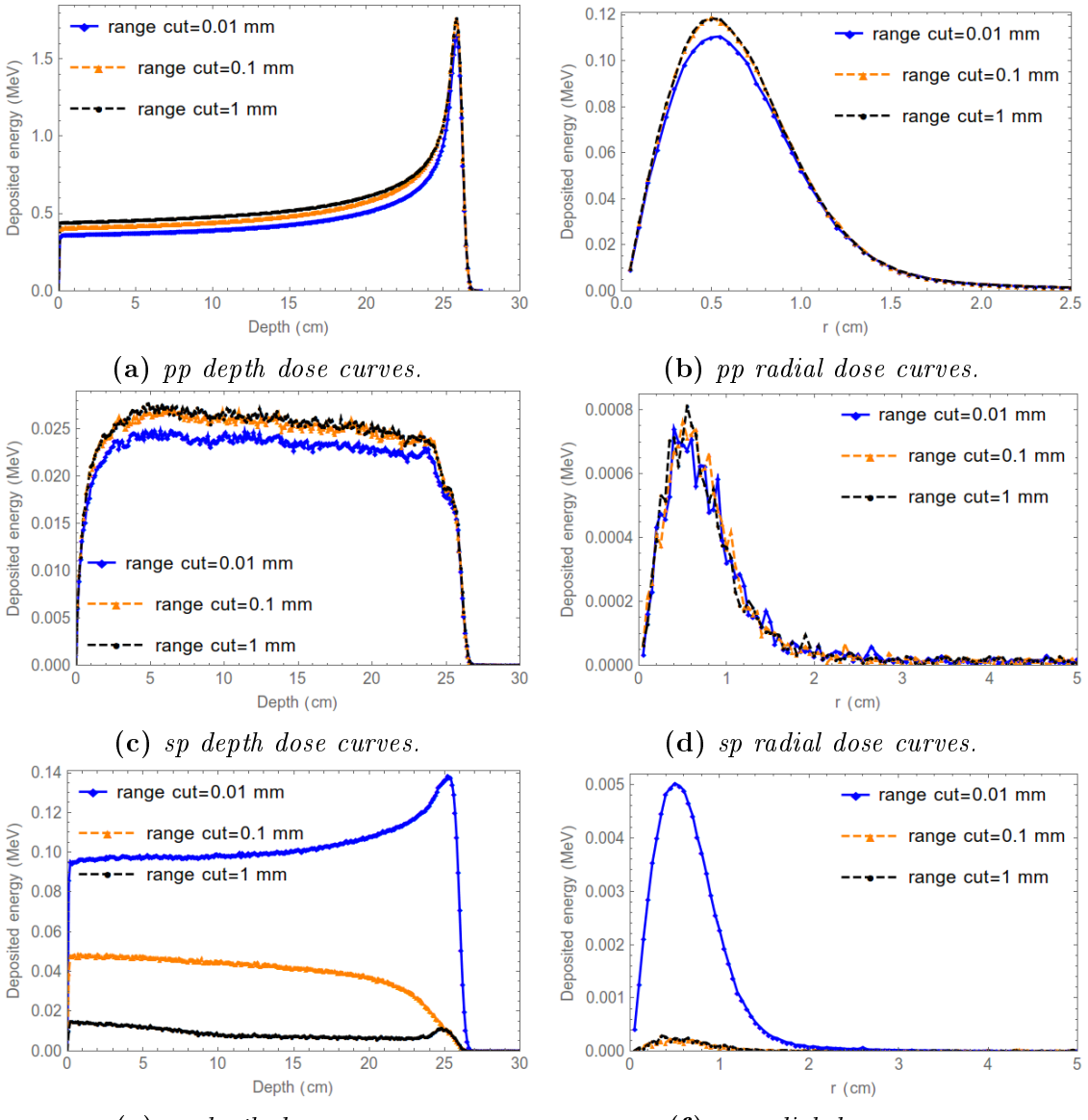

(a) *pp depth dose curves.*

(b) *pp radial dose curves.*

(c) *sp depth dose curves.*

(d) *sp radial dose curves.*

(e) *rc depth dose curves.*

(f) *rc radial dose curves.*

Figure E.1: *Plots illustrating lack of convergence in the dose profiles when a single cut-off value is used for all particles. Simulation settings: QGSP_BIC_EMY reference physics list, $E_0 = 200$ MeV, 10^6 source protons. The primary proton dose is shown in panes E.1a and E.1b, secondary protons in panes E.1c and E.1d, and recoils in panes E.1e and E.1f. Radial dose profiles taken at depth $z = 26.0$ cm.*

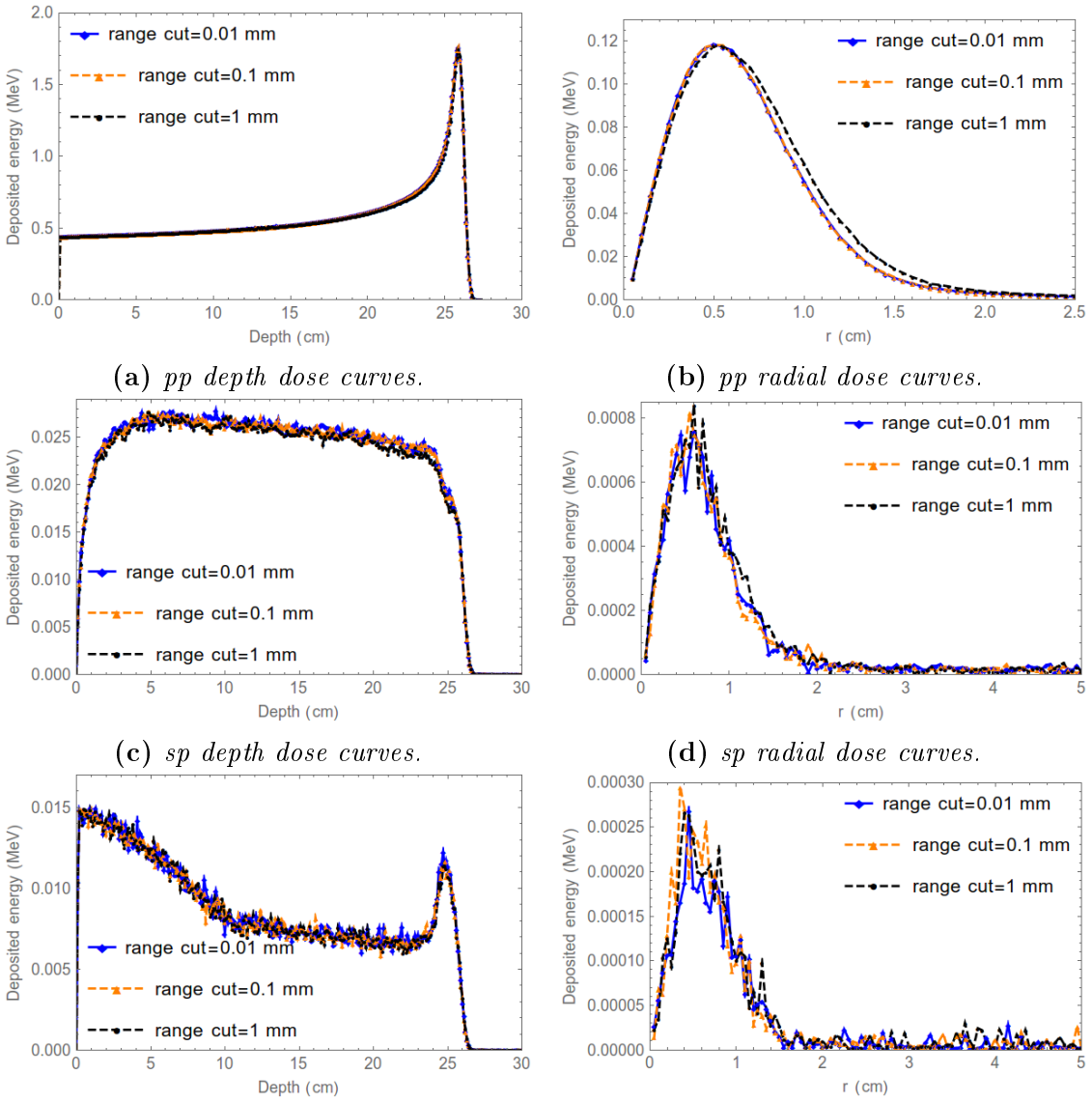

(a) *pp depth dose curves.*

(b) *pp radial dose curves.*

(c) *sp depth dose curves.*

(d) *sp radial dose curves.*

(e) *rc depth dose curves.*

(f) *rc radial dose curves.*

Figure E.2: *Convergence in the dose distribution is achieved when a special range cut is assigned to electrons (1.0 mm), protons are given range cuts of 0.01 mm, 0.1 mm, and 1.0 mm. Simulation settings: QGSP_BIC_EMY reference physics list, $E_0 = 200$ MeV, 10^6 source protons. The primary proton dose is shown in panes E.2a and E.2b, secondary protons in panes E.2c and E.2d, and recoils in panes E.2e and E.2f. Radial dose profiles taken at depth $z = 26.0$ cm.*

Bibliography

[1] Paganetti, H.: *Proton Therapy Physics.* CRC Press, 2011.

[2] De Laney, T.F. and Kooy, H.M.: *Proton and Charged Particle Radiotherapy.* Lippincott Williams & Wilkins, 2008.

[3] Röntgen, W.K.: On a new kind of rays. *CA: a cancer journal for clinicians*, vol. 22, no. 3, pp. 153–157, 1972.

[4] Wilson, R.R. *et al.*: Radiological use of fast protons. *Radiology*, vol. 47, no. 5, 1946.

[5] Bragg, W.H. and Kleeman, R.: LXXIV on the ionization curves of radium. *The London, Edinburgh, and Dublin Philosophical Magazine and Journal of Science*, vol. 8, no. 48, pp. 726–738, 1904.

[6] ICRU: Journal of the ICRU. [Online]. http://jicru.oxfordjournals.org/content/7/2/11/F4.large.jpg, [Accessed: 27 September 2015].

[7] Tobias, C.A., Anger, H. and Lawrence, J.H.: Radiological use of high energy deuterons and alpha particles. *The American journal of Roentgenology, Radium Therapy, and Nuclear Medicine*, vol. 67, no. 1, p. 1, 1952.

[8] Falkmer, S., Larsson, B. and Stenson, S.: Effects of single dose proton irradiation of normal skin and Vx2 carcinoma in rabbit ears. *Acta Radiologica [Old Series]*, vol. 52, no. 3, pp. 217–234, 1959.

[9] Larsson, B., Leksell, L., Rexed, B. and Sourander, P.: Effect of high energy protons on the spinal cord. *Acta Radiologica [Old Series]*, vol. 51, no. 1, pp. 52–64, 1959.

[10] Dalrymple, G.V., Lindsay, I.R., Hall, J.D., Mitchell, J.C., Ghidoni, J.J., Kundel, H.L. and Morgan, I.L.: The relative biological effectiveness of 138-MeV protons as compared to cobalt-60 gamma radiation. *Radiation Research*, vol. 28, no. 2, pp. 489–506, 1966.

[11] Dalrymple, G.V., Lindsay, I.R., Ghidoni, J.J., Hall, J.D., Mitchell, J.C., Kundel, H.L. and Morgan, I.L.: Some effects of 138-MeV protons on primates. *Radiation Research*, vol. 28, no. 2, pp. 471–488, 1966.

[12] Bonnett, D.: Current developments in proton therapy: a review. *Physics in Medicine and Biology*, vol. 38, 1993.

[13] iThemba LABS: iThemba LABS proton therapy center. http://tlabs.ac.za/?page_id=215, October 2015.

[14] PTCOG: Particle Therapy Co-operative Group. [Online]. http://www.ptcog.ch/index.php/facilities-in-operation, [Accessed: 27 January 2016].

[15] Berger, M.J.: *Penetration of Proton Beams Through Water: Depth-dose Distribution, Spectra and LET Distributions*. National Institute of Standards and Technology, 1993.

[16] Hogstrom, K.R., Mills, M.D. and Almond, P.R.: Electron beam dose calculation. *The Institute of Physics*, vol. 26, 1981.

[17] Hong, L., Goitein, M., Bucciolini, M., Comiskey, R., Gottschalk, B., Rosenthal, S., Serago, C. and Urie, M.: A pencil beam algorithm for proton dose calculations. *Physics in Medicine and Biology*, vol. 41, 1996.

[18] Hollmark, M., Uhrdin, J., Belkić, D., Gudowska, I. and Brahme, A.: Influence of multiple scattering and energy loss straggling on the absorbed dose distributions of therapeutic light ion beams: I. analytical pencil beam model. *Physics in Medicine and Biology*, vol. 49, 2004.

[19] Eyges, L.: Multiple scattering with energy loss. *Physical Review*, vol. 74, 1948.

[20] Brahme, A., Lax, I. and Andreo, P.: Electron beam dose planning using discrete gaussian beams: mathematical background. *Acta Oncologica*, vol. 20, 1981.

[21] Lillicrap, S., Wilson, P. and Boag, J.: Dose distributions in high energy electron beams: Production of broad beam distributions from narrow beam data. *Physics in Medicine and Biology*, vol. 20, 1975.

[22] Bortfeld, T.: An analytical approximation of the bragg curve for therapeutic proton beams. *Med. Phys.*, vol. 24, 1997.

[23] Bortfeld, T. and Schlegel, W.: An analytical approximation of depth-dose distributions for therapeutic proton beams. *Phys. Med. Biol.*, vol. 41, 1996.

[24] Bichsel, H. and Hiraoka, T.: Energy spectra and depth-dose curves for 70 MeV protons. *International Journal of Quantum Chemistry*, vol. 36, no. S23, pp. 565–574, 1989.

[25] Newhauser, W., Fontenot, J., Zheng, Y., Polf, J., Titt, U., Koch, N., Zhang, X. and Mohan, R.: Monte Carlo simulations for configuring and testing an analytical proton dose-calculation algorithm. *Physics in Medicine and Biology*, vol. 52, no. 15, p. 4569, 2007.

[26] Janni, J.F.: Proton range-energy tables, 1 keV-10 GeV, energy loss, range, path length, time-of-flight, straggling, multiple scattering, and nuclear interaction probability. part i. for 63 compounds. *Atomic data and nuclear data tables*, vol. 27, p. 147, 1982.

[27] Berger, M., Inokuti, M., Andersen, H. and Bichsel, H.: Stopping powers and ranges for protons and alpha particles. *ICRU Report*, vol. 49, 1993.

[28] Bethe, H.: Moliére's theory of multiple scattering. *Physical Review*, vol. 89, no. 6, p. 1256, 1953.

[29] Highland, V.L.: Some practical remarks on multiple scattering. *Nuclear Instruments and Methods*, vol. 129, no. 2, pp. 497–499, 1975.

[30] Goudsmit, S. and Saunderson, J.: Multiple scattering of electrons. *Physical Review*, vol. 57, 1940.

[31] Lewis, H.: Multiple scattering in an infinite medium. *Physical Review*, vol. 78, no. 5, p. 526, 1950.

[32] Ulmer, W. and Matsinos, E.: Theoretical methods for the calculation of bragg curves and 3D distributions of proton beams. *The European Physical Journal Special Topics*, vol. 190, 2010.

[33] Börgers, C. and Larsen, E.W.: The Fermi pencil beam approximation. In: *Proc. ANS Topical Meeting, Int. Conf. on Mathematics and Computations, Reactor Physics, and Environmental Analyses*, vol. 1. 1995.

[34] Jette, D.: Electron dose calculation using multiple-scattering theory. a. Gaussian multiple-scattering theory. *Medical Physics*, vol. 15, 1988.

[35] Ulmer, W. and Schaffner, B.: Foundation of an analytical proton beamlet model for inclusion in a general proton dose calculation system. *Radiation Physics and Chemistry*, vol. 80, 2011.

[36] Turner, J.E., Downing, D.J. and Bogard, J.S.: *Statistical Methods in Radiation Physics*. Wiley, 2012.

[37] Xu, X.G. and Eckerman, K.F.: *Handbook of Anatomical Models for Radiation Dosimetry*. CRC Press, 2009.

[38] Agostinelli, S., Allison, J., Amako, K.a., Apostolakis, J., Araujo, H., Arce, P., Asai, M., Axen, D., Banerjee, S., Barrand, G. *et al.*: GEANT4–a simulation toolkit. *Nuclear Instruments and Methods in Physics Research Section A: Accelerators, Spectrometers, Detectors and Associated Equipment.*
Available at: https://geant4.web.cern.ch/geant4/

[39] Geant4 Collaboration: Geant4 User's Guide for Application Developers. *Accessible from the GEANT4 web page*, vol. 9, 2014.
Available at: http://geant4.web.cern.ch/geant4/support/userdocuments.shtml

[40] Grevillot, L., Frisson, T., Zahra, N., Bertrand, D., Stichelbaut, F., Freud, N. and Sarrut, D.: Optimization of GEANT4 settings for proton pencil beam scanning simulations using gate. *Nuclear Instruments and Methods in Physics Research Section B: Beam Interactions with Materials and Atoms*, vol. 268, no. 20, pp. 3295–3305, 2010.

[41] Wright, D.H., Koi, T., Folger, G., Ivantchenko, V., Kossov, M., Starkov, N., Heikkinen, A. and Wellisch, H.-P.: Recent developments and validations in GEANT4 hadronic physics. *Calorimetry in High Energy Physics*, vol. 867, 2006.

[42] Gottschalk, B.: Passive beam spreading in proton radiation therapy. *unpublished book*, 2004.

[43] Newhauser, W.D. and Zhang, R.: The physics of proton therapy. *Physics in Medicine and Biology*, vol. 60, no. 8, p. R155, 2015.

[44] ICRU, Stopping Powers: Ranges for protons and alpha particles. *International Commission on Radiation Units and Measurements. Report*, vol. 49, 1993.

[45] Leo, W.R.: *Techniques for Nuclear and Particle Physics Experiments: a how-to approach*. Springer Science & Business Media, 2012.

[46] Ziegler, J.F.: SRIM-2003. *Nuclear Instruments and Methods in Physics Research Section B: Beam Interactions with Materials and Atoms*, vol. 219, pp. 1027–1036, 2004.

[47] Geant4 Collaboration *et al.*: Physics Reference Manual. *Version geant4*, vol. 16, 2014.
Available at: http://geant4.web.cern.ch/geant4/UserDocumentation/UsersGuides/PhysicsReferenceManual/fo/PhysicsReferenceManual.pdf

[48] Jarlskog, C.Z. and Paganetti, H.: Physics settings for using the Geant4 toolkit in proton therapy. *Nuclear Science, IEEE Transactions on*, vol. 55, no. 3, pp. 1018–1025, 2008.

[49] Shinohara Eric-OncoLink: The Physics of Proton Therapy-module 2. [Online]. https://www.oncolink.org/includes/print_article.cfm?Page=2&id=413&section=treatment_options, [Accessed: 4 Novemeber 2016].

[50] Urbán, L.: A model for multiple scattering in Geant4. Tech. Rep., 2006.

[51] Ahmed, S.N.: *Physics and Engineering of Radiation Detection*. Academic Press, 2007.

[52] Börgers, C. and Larsen, E.W.: On the accuracy of the Fokker–Planck and Fermi pencil beam equations for charged particle transport. *Medical Physics*, vol. 23, 1996.

[53] Gottschalk, B., Koehler, A., Schneider, R., Sisterson, J. and Wagner, M.: Multiple Coulomb scattering of 160 MeV protons. *Nuclear Instruments and Methods in Physics Research Section B: Beam Interactions with Materials and Atoms*, vol. 74, no. 4, pp. 467–490, 1993.

[54] Arce, P. Maire, M.U.L. and M., W.: Multiple Scattering in Geant4. a Comparison with Moliére theory and L3 detector data. [Online]. https://inis.iaea.org/search/search.aspx?orig_q=RN:33013562, [Accessed: 8 February 2016].

[55] Arce, P., Maire, M., Urban, L. and Wadhwa, M.: Multiple scattering in GEANT4: A comparison with Moliere theory and L3 detector data. In: *Advanced Monte Carlo for radiation physics, particle transport simulation and applications. Proceedings, Conference, MC2000, Lisbon, Portugal, October 23-26, 2000*, pp. 503–510. 2000.

[56] Chadwick, M., Hughes, H., Little, R., Pitcher, E. and Young, P.: Nuclear data for accelerator-driven systems. *Progress in Nuclear Energy*, vol. 38, no. 1, pp. 179–219, 2001.

[57] Ulmer, W. and Matsinos, E.: A calculation method of nuclear cross-sections of proton beams by the collective model and the extended nuclear-shell theory with applications to radiotherapy and technical problems. *Journal of Nuclear and Particle Physics*, vol. 2, no. 3, pp. 42–56, 2012.

[58] Paganetti, H.: Nuclear interactions in proton therapy: dose and relative biological effect distributions originating from primary and secondary particles. *Physics in Medicine and Biology*, vol. 47, no. 5, 2002.

[59] Medin, J. and Andreo, P.: Monte Carlo calculated stopping-power ratios, water/air, for clinical proton dosimetry (50-250 MeV). *Physics in Medicine and Biology*, vol. 42, no. 1, pp. 89–105, 1997.

[60] Tung, C.-J. *et al.*: Microdosimetric relative biological effectiveness of therapeutic proton beams. *Biomedical Journal*, vol. 38, no. 5, p. 399, 2015.

[61] Carlsson, C. and Carlsson, G.A.: Proton dosimetry with 185 MeV protons. 1977.

[62] Quesada, J.M., Ivanchenko, V., Ivanchenko, A., Cortés-Giraldo, M.A., Folger, G., Howard, A. and Wright, D.: Recent Developments in Pre-Equilibrium and De-Excitation Models in Geant4. *Progress in Nuclear Science and Technology*, vol. 2, pp. 936–941, 2011.

[63] de Kock, E.: Proton pencil beam kernels derived from monte carlo simulations. iThemba LABS. *Unpublished work*, 2009.

[64] Hendee, W.R.: Medical Radiation Physics. 1970.

[65] Stankovskiy, A., Kerhoas-Cavata, S., Ferrand, R. and Nauraye, C.: Monte Carlo simulation of a CPO beam line: modelling the nuclear interactions. In: *International Conference on Nuclear Data for Science and Technology*. EDP Sciences, 2007.

[66] Carlsson, Å.K., Andreo, P. and Brahme, A.: Monte Carlo and analytical calculation of proton pencil beams for computerized treatment plan optimization. *Physics in Medicine and Biology*, vol. 42, no. 6, 1997.

[67] Ulmer, W.: Theoretical aspects of energy–range relations, stopping power and energy straggling of protons. *Radiation Physics and Chemistry*, vol. 76, no. 7, pp. 1089–1107, 2007.

[68] Ulmer, W. and Schaffner, B.: Laboratory Report (LR) to the paper Foundation of an analytical proton beamlet model for inclusion in a general proton dose calculation system [arxiv: 1009.0832]. *arXiv preprint arXiv:1009.2187*, 2010.

[69] Chadwick, M. and Young, P.: Proton nuclear interactions with 12C, 14N, 16O, 31P and 40Ca for radiotherapy applications: Evaluated data libraries to 250 MeV. Tech. Rep., Los Alamos National Laboratory Report, 1996.

[70] Varian medical systems: Proton Algorithm Reference Guide-Eclipse. vol. P/N B500299R01C, April 2007.

[71] Wolfram Research, Inc.: Mathematica. https://www.wolfram.com, 2015.

[72] Asai, M., Dotti, A., Verderi, M., Wright, D.H., Geant4 Collaboration and others: Recent developments in Geant4. *Annals of Nuclear Energy*, 2014.

[73] Malathi, R. and Krishnan, J.: *Recent Advancements in System Modelling Applications: Proceedings of National Systems Conference 2012*, vol. 188. Springer Science & Business Media, 2013.

[74] Cirrone, G.P., Cuttone, G., Mazzaglia, S.E., Romano, F., Sardina, D., Agodi, C., Attili, A., Blancato, A.A., De Napoli, M., Di Rosa, F. *et al.*: Hadrontherapy: a Geant4-based tool for proton/ion-therapy studies. *Prog. Nucl. Sci. Technol*, vol. 2, pp. 207–212, 2011.

[75] Aso, T., Kimura, A., Tanaka, S., Yoshida, H., Kanematsu, N., Sasaki, T. and Akagi, T.: Verification of the dose distributions with GEANT4 simulation for proton therapy. *Nuclear Science, IEEE Transactions on*, vol. 52, no. 4, 2005.

[76] Electromagnetic Standard Physics Working Group: [Online]. http://geant4.web.cern.ch/geant4/collaboration/working_groups/electromagnetic/, [Accessed: 27 January 2016].

[77] Seravalli, E., Robert, C., Bauer, J., Stichelbaut, F., Kurz, C., Smeets, J., Ty, C.V.N., Schaart, D., Buvat, I., Parodi, K. *et al.*: Monte Carlo calculations of positron emitter yields in proton radiotherapy. *Physics in Medicine and Biology*, vol. 57, no. 6, p. 1659, 2012.

[78] Ivanchenko, V., Kadri, O., Maire, M. and Urban, L.: Geant4 models for simulation of multiple scattering. In: *Journal of Physics: Conference Series*, vol. 219. IOP Publishing, 2010.

[79] Fippel, M. and Soukup, M.: A Monte Carlo dose calculation algorithm for proton therapy. *Medical Physics*, vol. 31, no. 8, pp. 2263–2273, 2004.

[80] Berger, M.J.: Proton monte carlo transport program PTRAN. *Unknown*, vol. 1, 1993.

[81] ICRU, Radiation Dosimetry: Electron beams with energies between 1 and 50 MeV. *ICRU Report*, vol. 35, 1984.

[82] Geant4 Reference Physics List Group: Geant4 Reference Physics List. [Online]. http://geant4.cern.ch/support/proc_mod_catalog/physics_lists/referencePL.shtml, [Accessed: 22 February 2015].